LASER STUDIES IN FLAMES

A Thesis

submitted in partial fulfilment

of the requirements for the Degree

of

Doctor of Philosophy in Chemistry

in the

University of Canterbury

by

Terence John Brady

University of Canterbury

1980

ACKNOWLEDGEMENTS

I would like to express my sincere thanks to my supervisor Professor L.F. Phillips for his willing help and constant enthusiasm throughout this work, without which it may never have been completed.

I am also indebted to many members of the technical staff of the Chemistry Department for their advice and the construction of some of the apparatus. I would also like to thank Mr R.S. Temple for his help with reproducing some of the hydrogen data, and his assistance with some of the computing.

I am grateful to the New Zealand University Grants Committee for the award of a Teaching Fellowship, and to the Petroleum Research Committee of the American Chemical Society for the assistance provided by Grant 8052-AC5.

Finally my thanks to Mrs Christine Haughey who deciphered and typed the text, and to Ms Mary Noonan for also helping with the typing. Special thanks to Mary and Inata for much encouragement and understanding.

Terence John Brady

ABSTRACT

Laser excited fluorescence was used to investigate minority species in premixed H_2:N_2:O_2 flames with temperatures ranging from about 1500 K to 2400 K. The species CH and NH were produced in a series of flames but detection by laser fluorescence failed. Fluorescence studies of metal atoms enabled the rate of spin-orbit relaxation

$$Pb(7s^3P_1^o) \rightarrow Pb(7s^3P_0^o)$$

in collisions with atomic hydrogen and flame bulk-constituents to be measured. For hydrogen as the collision partner , the rate constant showed a negative temperature coefficient, varying as $T^{-1.7}$, whereas for other flame bulk constituents the rate constant showed a positive coefficient, varying as $T^{1.8}$. The process is described in terms of the Landau-Zener theory of non-adiabatic transitions between potential curves corresponding to excited states of the transient molecules formed during collisions. The magnitude of the rate constants and the signs of the temperature coefficients are predicted correctly by the application of the Landau-Zener theory.

LIST OF CONTENTS

LIST OF CONTENTS (Cont'd)

LIST OF ILLUSTRATIONS

LIST OF ILLUSTRATIONS (Cont'd)

LIST OF TABLES

CHAPTER I

INTRODUCTION

The work described in this thesis relates to the application of laser fluorescence techniques to the study of the kinetics of minority species in flames. In particular, the reactions of lead atoms in collisions with atomic hydrogen and other flame constituents have been studied.

A flame is essentially a high temperature, flowing, gas phase reaction system, in which the time scale can be converted to a scale of distance along the 'tail' of the flame. The high linear gas velocities, (typically about 10 $m.s^{-1}$) in the burnt gas stream, enable reasonably fast reactions to be studied, and by altering the composition of unburnt gas, (fuel, oxidant and diluent) a whole range of temperatures and reaction conditions can be obtained. The structure of flames and the methods used in their study are well described in books by Gaydon and Wolfhard[1], and Mavrodineanu[2] and will not be dealt with in detail here.

Methods of studying flames can be divided into two main categories, namely perturbing, and nonperturbing. Perturbing methods, as their name suggests, have the principal disadvantage of introducing some unwanted change in the characteristics of the flame. These include solid probe sampling, for example mass spectrometric techniques, conductivity measurements, and thermocouple temperature determination. However the extent to which the introduction

of solid probes changes the characteristics of the flame is generally small, and these methods have provided much valuable information on flame processes.

Within the framework of nonperturbing techniques, a wide variety of methods has been explored to measure processes and state properties of the combustion systems. The most notable of these are absorption and emission studies, but these can sometimes suffer from limitations in spatial resolution and from spectral interferences from other flame constituents. One of the newest techniques which does not suffer from these limitations is that of laser fluorescence, which has been made practical by the development of the tunable dye laser, and has the advantages of high sensitivity, good spatial resolution, and the facility to cover the entire visible spectrum, with suitable choice of dye, and with frequency doubling, this can be extended into the ultra-violet. One disadvantage of laser fluorescence applied to combustion systems at present, is that while schemes can be devised to monitor specific states of interest of a species, specific fluorescence quenching cross-sections may not be available. Also, care must be taken that the high intensity available with pulsed lasers (especially long duration pulses) does not cause significant changes from equilibrium in the species under study, such as absorption saturation. The use of a very short laser pulse can also lead to problems, where the pulse may be too short to enable a steady state to be set up between two excited states, for example, when exciting into a closely spaced

doublet. However, laser fluorescence has been applied successfully to measurements in flames, such as temperature determination[3], Raman scattering[4], and as an analytical tool[5]. It has been used to study reactions in flames[6], but has not yet found wide application. This work provides an example of the technique applied to the study of kinetics in combustion systems.

SUMMARY OF THESIS

Chapter two deals with a description of the experimental apparatus and the electronic and optical set up used to obtain fluorescence, emission and temperature measurements.

Chapter three is a brief summary of the work on various species in flames in attempts to characterise them, or obtain kinetic data of their reactions with other flame components. This includes the initial findings on lead introduced to the flame.

Chapter four describes the measurement of radical concentrations and establishes the dependence of spin-orbit relaxation of excited $^3P_1^o/^3P_0^o$ lead on hydrogen atom concentration.

Chapter five is concerned with the calculation of the rate constants for this process, and the importance of laser pulse width, and intensity is also assessed. Results are presented for hydrogen atoms, and flame bulk constituents as the colliding partners.

Chapter six gives a brief description of the Landau-Zener theory of collisions and its modifications and

applicability. The theory is applied to non-adiabatic transitions of molecules corresponding to bound states of PbH. Suitable potential curves are found which predict the observed rates of inter-level transitions in lead.

CHAPTER II

EXPERIMENTAL

I. THE BURNER

The burner used in this work was similar to that used by Phillips[7], McEwan[8] and Mulvihill[9]. Figure 1 shows the construction of the burner, the core of which consisted of five hundred 20 gauge hypodermic tubes bonded together with epoxy resin. The central one hundred tubes A, were supplied with gas plus additives for the experimental study flame, while the two hundred tubes forming the annulus B, were supplied with gas of identical composition excluding additives, in an amount calculated to give identical vertical gas velocity. The remaining two hundred tubes C, were generally supplied with a small amount of nitrogen to prevent the entrainment of air in cool flames, and to prevent charring of the burner-face sealant by the diffusion flame in hot flames. Nitrogen flow in this outer sheath was not metered, but adjusted until the outer diffusion flame disappeared, as suggested by Kaskan[10]. The burner face was machined flat, and each hypodermic tube counter sunk, so that the reaction zone would be as flat as possible, and laser scattering by irregularities on the burner face would be minimised.

Cooling water was supplied to chamber D. The compartments E, D, F, were sealed with neoprene "O" rings G and the central flame inlet was held in place by R.T.V. silicone rubber sealant, to eliminate strain. The top face

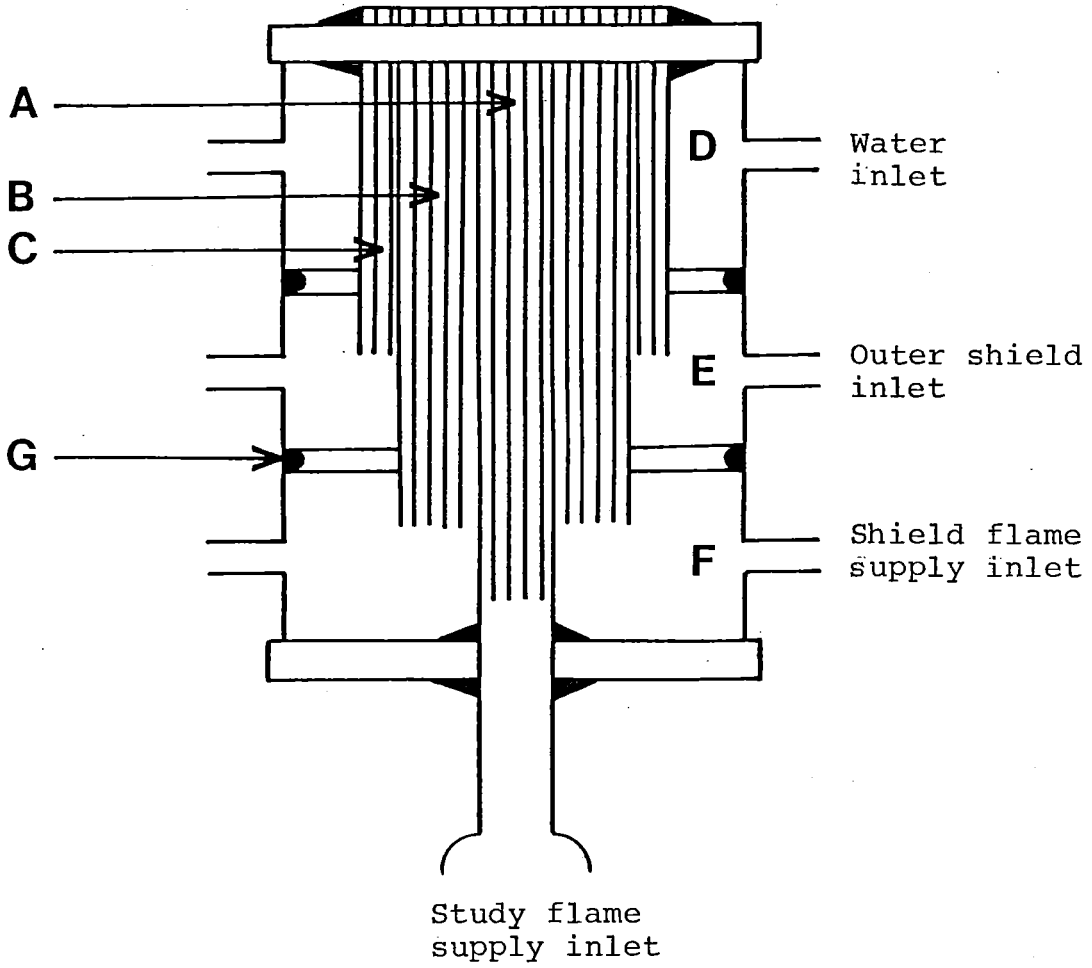

Fig. 1 Construction of the burner.

A Central study flame core

B Inner shield flame core

C Outer shield core

D Cooling water jacket

E Outer shield supply chamber

F Inner shield supply chamber

G Neoprene "0" ring

of the burner was also sealed with silicone rubber. A ground-glass ball joint at the central inlet allowed free movement of the burner and also provided a safety valve in case of strike-back, which did not occur.

The burner was mounted vertically on a threaded shaft which allowed adjustment over a height range of 10 cm. This allowed distances in the burnt gas region to be converted into a time scale by calculating the flow rate from the flow rate of unburnt gas, the cross sectional area of the central flame, the position of the flame front, determined from the intensity of CuH emission, and the final temperature of the burnt gas. A fume hood was positioned over the burner to prevent harmful products such as Pb, NH_3, and Tl from escaping into the laboratory. The inside of the fume hood was painted matt-black to absorb stray and scattered light.

II. FLAMES: THEIR COMPOSITION AND CONTROL

The gas handling system is illustrated in fig. 2. For the central study flame, flow rates were monitored with Hastings mass flow meters, and a voltage output proportional to the flow rate was displayed on a digital voltmeter. Uncertainty in the flow rates is given as 1%. Shield flame gas flow rates were monitored with simple capillary-type flowmeters with interchangeable capillaries and di-n-butyl phthalate as the manometric fluid. These were calibrated with a bubble meter and a stopwatch. Agreement between the mass-flowmeters and the capillary flowmeters was within 5%. During the course of the work,

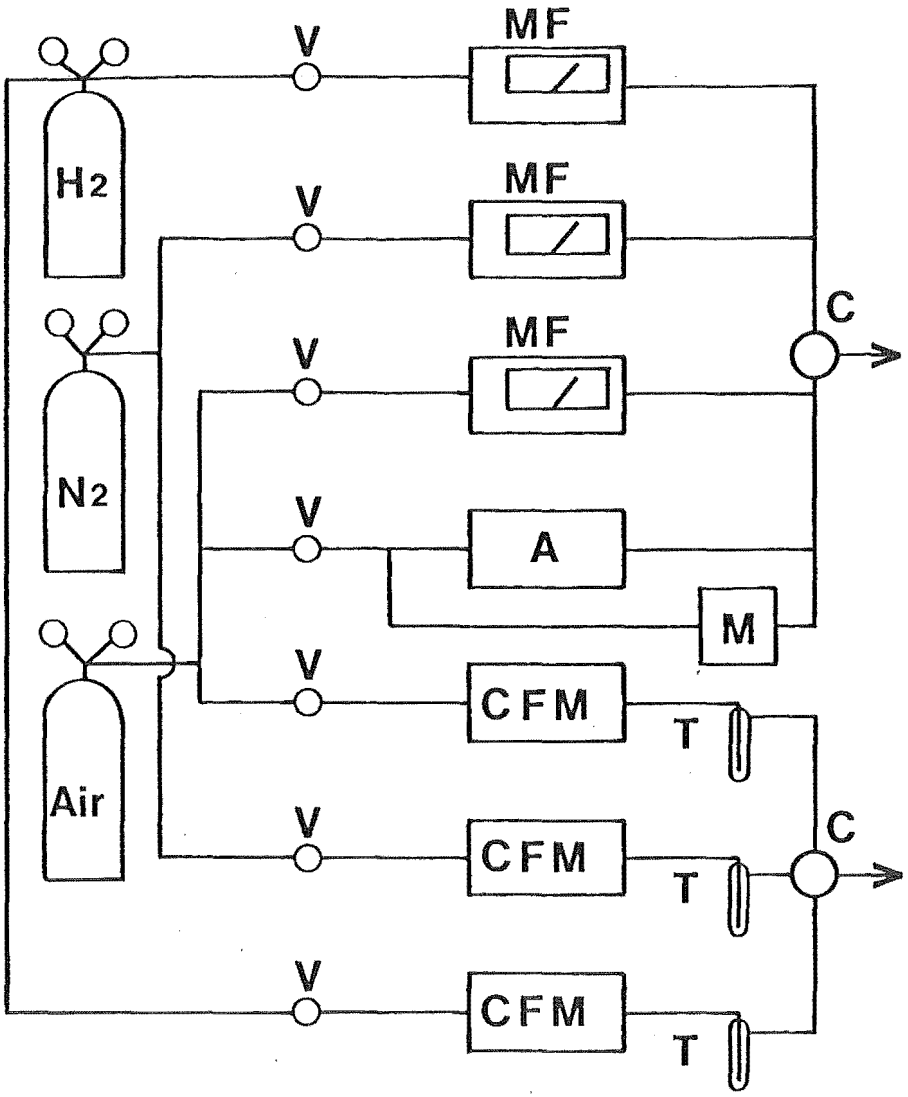

Fig. 2 Schematic representation of the gas handling system.

V Needle valve
MF Mass flowmeter
A Atomiser
M Mercury manometer
CFM Capillary flowmeter
T Trap
C Cyclone flow mixing chamber

it was found necessary to wash the air supply mass-flowmeter with solvent, as erroneous readings resulted after prolonged use with industrial compressed air. This presumably was due to the build up of a thin oil film on the temperature sensors of the flowmeter unit.

The gases used were commercial hydrogen, nitrogen and compressed air of industrial grades without further purification. In calculating gas flow rates for a given flame, it was assumed that the air consisted of exactly 20% oxygen and 80% nitrogen. Mixing of the gases prior to burning was accomplished in a small cyclone-flow mixing chamber with a volume of about 100 cm^3.

As in previous work[7,8,9], the flames were classified according to their unburnt composition. A family of flames is a group with the same, usually integral, nitrogen to oxygen ratio. In the flames used in this work the hydrogen to oxygen ratio took the values 2.0, 2.5, 3.0, 3.5, 4.0, 4.5.* Flames having these ratios were denoted by the letters A, F, K, P, U, Z respectively. The nitrogen to oxygen ratio, or family number, is indicated as a suffix.

---

* The mass flowmeters used in this work were supplied calibrated for delivery of air, and a correction factor of 1.03 allows delivery of H_2 to be monitored. For the flames used, this correction was not applied to the flow rates, but was used to calculate the composition of flames with flow rates read directly from the flowmeters. Thus flame Z6, in the present work would have had actual composition $H_2:N_2:O_2$ = (4.5 x 1.03):6:1. In all calculations, the exact composition of air was used.

For example, flame Z6 has unburnt composition

$$H_2:N_2:O_2 = 4.5:6:1$$

and P8 has composition

$$H_2:N_2:O_2 = 3.5:8:1 .$$

III. ADDITIVES

Metals were added to the unburnt gases as fine sprays of solutions of their salts. This was accomplished by diverting a portion of the air supply for the central flame through an atomiser, which is shown in Plate 1. Nitrates and chlorides of the metals were used, as these are known to be completely and rapidly fragmented in the reaction zone, unlike the more stable phosphates and sulphates[11]. All metallic salts used were of ANALAR grade.

The delivery of the atomiser was calculated by a comparison of a curve of growth of sodium D line thermal emission in the flame with the appropriate Van-der-Held curve, as described by James and Sugden[12]. The onset of self reversal, given by the change in slope from 1.0 to 0.5, allowed the density of sodium atoms to be calculated. The concentration of sodium atoms in flame K4, with an atomiser air supply of 40 $cm^3\ s^{-1}$ and a 1 M NaCl solution was calculated to be 5.3×10^{-5} atm. In all experimental flames, the concentration was no higher than 10^{-6} atm and typically 10^{-7} atm. The sodium emission curve of growth at 589.0 nm is shown in fig. 3.

IV TEMPERATURE MEASUREMENTS

Temperature measurements in the burnt gas region

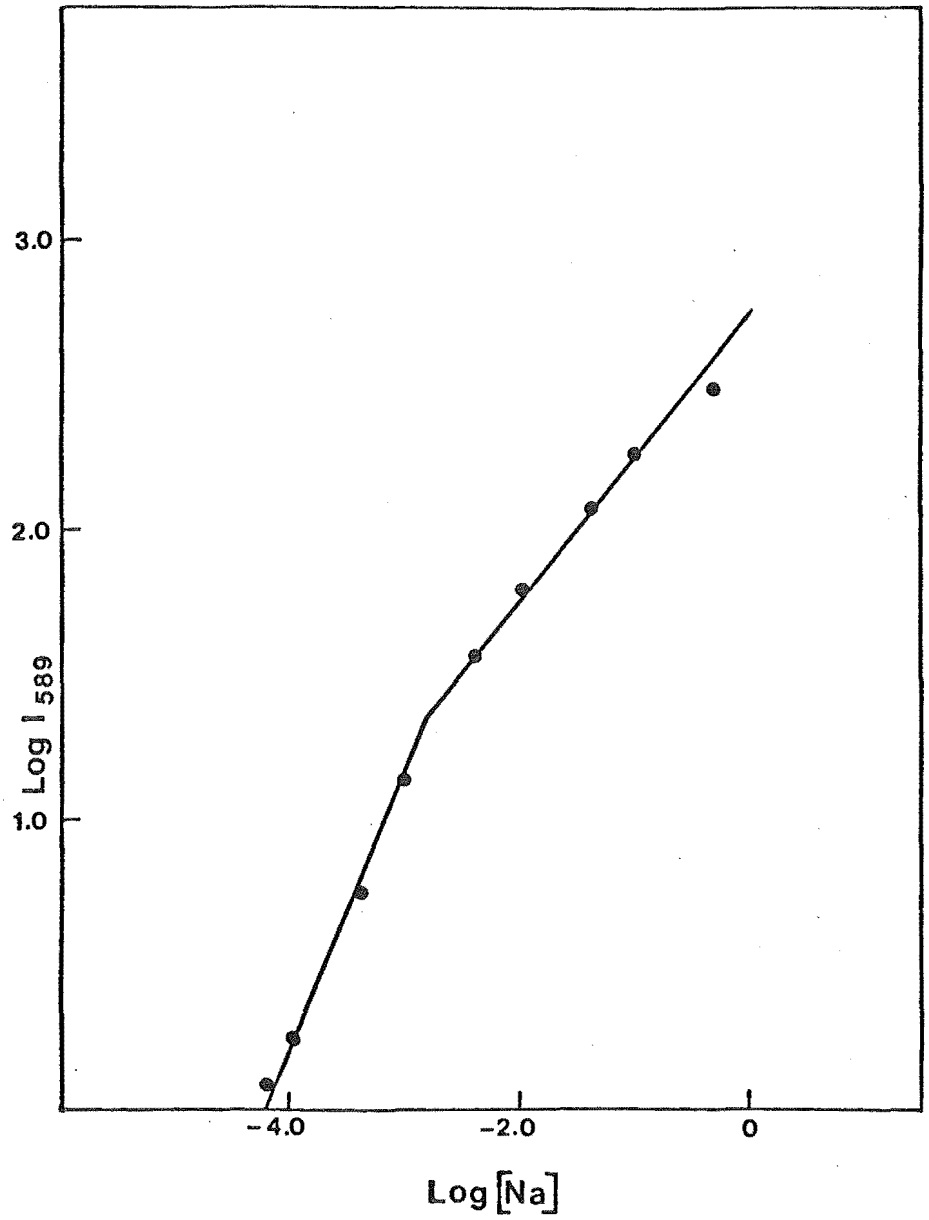

Fig. 3 Sodium emission curve of growth at 589.0 nm where [Na] is the concentration of sodium in the atomiser solution (moles.l^{-1}).

were obtained by the sodium D line reversal method. The usual procedure was adopted in making the reversal measurements[1]. A calibrated optical pyrometer was used to determine the colour temperature in the red of the image of a tungsten-strip filament lamp in the flame. These temperatures were corrected to the yellow from the emissivity data of de Voss[13]. The strip filament lamp was run from a stabilised A.C. mains supply of 240 V through a variac and a transformer and operated over a current range of 6A to 15A.

Line reversals were obtained photometrically using the optical scheme shown in fig. 4. The image of the filament in the flame was focussed onto the slits of a SPEX MINIMATE monochromator and the D.C. output of the photomultiplier (EMI 6255) was monitored with a high-speed KEITHLEY picoammeter. This detection system, without the lamp, was employed in all emission studies in this work.

Sodium reversal temperatures are a measure of the extent of electronic excitation of sodium atoms[1], so that for cool flames, there is a sharp upward curve near the reaction zone due to chemi-excitation of sodium atoms[14], and it is only downstream from the reaction zone, where [H] and [OH] are small, that the reversal temperatures may be taken as a measure of the true thermal temperature of the burnt gases.

All the flames used in this work had final temperatures greater than 1500 K. Under these conditions the sodium emission at distances greater than 10 mm may be considered to arise solely from thermal excitation with negligible contribution from chemi-excitation effects.

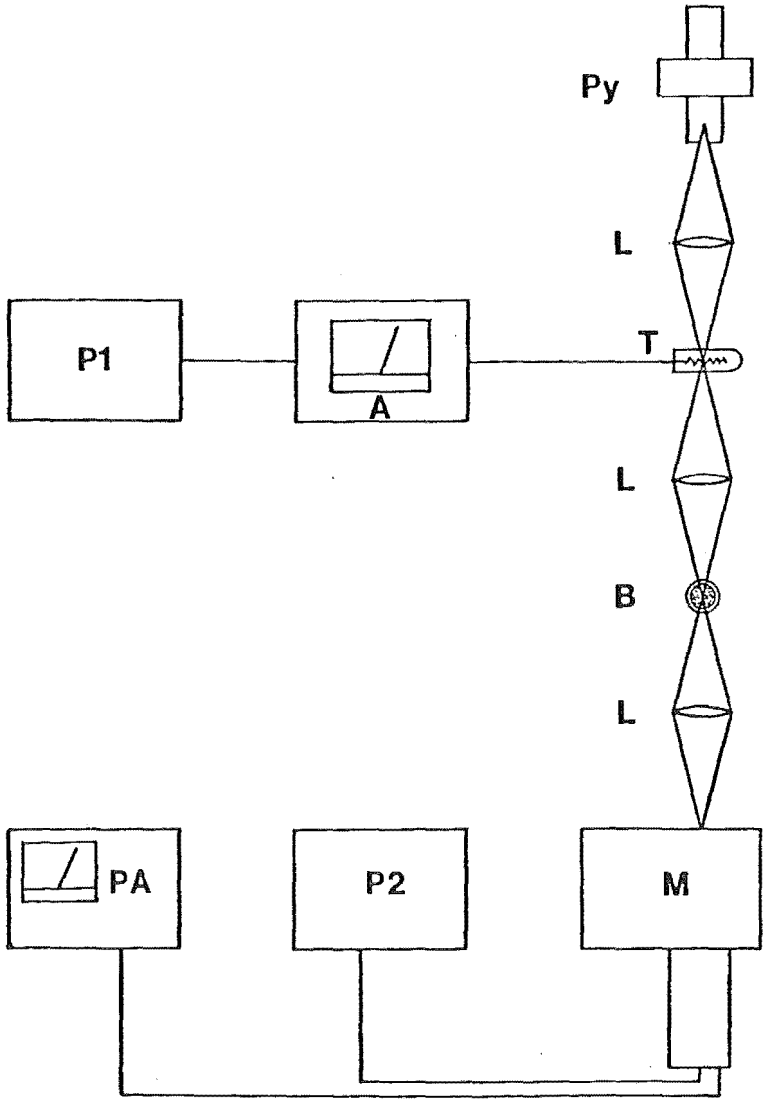

KEY:

P1 0 to 6V power supply
P2 0 to 2kV power supply
A Ammeter
L Lens
PY Optical Pyrometer
T Tungsten strip filament lamp
B Burner
M Monochromator
PA Picoammeter

Fig. 4
Temperature and emission measurement set up.

Temperature measurements were made by sodium reversal, at two to four points in each flame, and sodium D line emission at 589.0 nm was used to scale these temperatures for other points in the flame.

V. PHOTOMETER SENSITIVITY

In all fluorescence and emission studies in this work, the photometer consisted of a SPEX MINIMATE monochromator with an EMI 6255 photomultiplier having a standard 'tapered' dynode chain[15].

The response of the photometer to incident light was determined by viewing the spectral intensity distribution of a tungsten-strip filament lamp at a known temperature. The distribution of light from a tungsten lamp is given by Planck's law[16].

$$I(\lambda,T)d\lambda = E(\lambda,T)\ \frac{8\pi hc^2}{\lambda^5\ 4\pi}\ \left(\exp\left(\frac{hc}{\lambda kT}\right) - 1\right)^{-1} d\lambda$$

where $I(\lambda,T)d\lambda$ is in Watts. ster.$^{-1}$ m^{-2}, and is the intensity. $E(\lambda,T)$ is the emissivity of tungsten at a temperature T K and wavelength λ m, h is Planck's constant, c is the velocity of light m.s^{-1}, and k is the Boltzmann constant. Thus the number of photons emitted is given by $N(\lambda,T)$

$$N(\lambda,T) = \frac{I(\lambda,T)}{hc/\lambda} = E(\lambda,T)\ \frac{8\pi c}{4\pi\lambda 4}\ \left(\exp\left(\frac{hc}{\lambda kT}\right) - 1\right)^{-1}$$

where $N(\lambda,T)$ is in photons.s^{-1}.ster^{-1}.m^{-2}.

Since all measurements were made with the same optical arrangements, the fraction of these photons incident on the photomultiplier is constant for all wave-

lengths, assuming the monochromator to have constant dispersion. Hence $N(\lambda,T)$ represents the relative number of photons collected at a given wavelength. The relative sensitivity of the photometer is then given by S_{REL}, where

$$S_{REL} = \frac{I(pm)}{N(\lambda,T)} \quad \text{amperes. s photon}^{-1}.$$

and I(pm) is the measured anode current of the photomultiplier. The sensitivity curve as a function of wavelength λ is shown in fig. 5. This curve was used to determine the relative response of the photometer to fluorescence and emission at different wavelengths during this work.

VI. FLUORESCENCE MEASUREMENTS

A diagram of the experimental set-up is given in fig. 6 and is also shown in plate 1. The output of a pulsed nitrogen laser (AVCO model C5000 operated at 80 - 100 Hz) was focussed into an AVCO (model 4000) dye laser which incorporated interchangeable flowing dye cassettes enabling the dye to be circulated so that laser pumping at frequencies of 100 Hz or more could be used without local heating problems. The manual drive for the intra-cavity grating of the dye laser was modified, being equipped with a reduction gearing system to allow very fine control of the grating angle.

The tuned output of the dye laser, which had a band width typically of 0.05 nm to 0.1 nm was focussed in the centre of the burner by lens L_1. A concave mirror M_1 was chosen so that the reflected beam was returned at the same

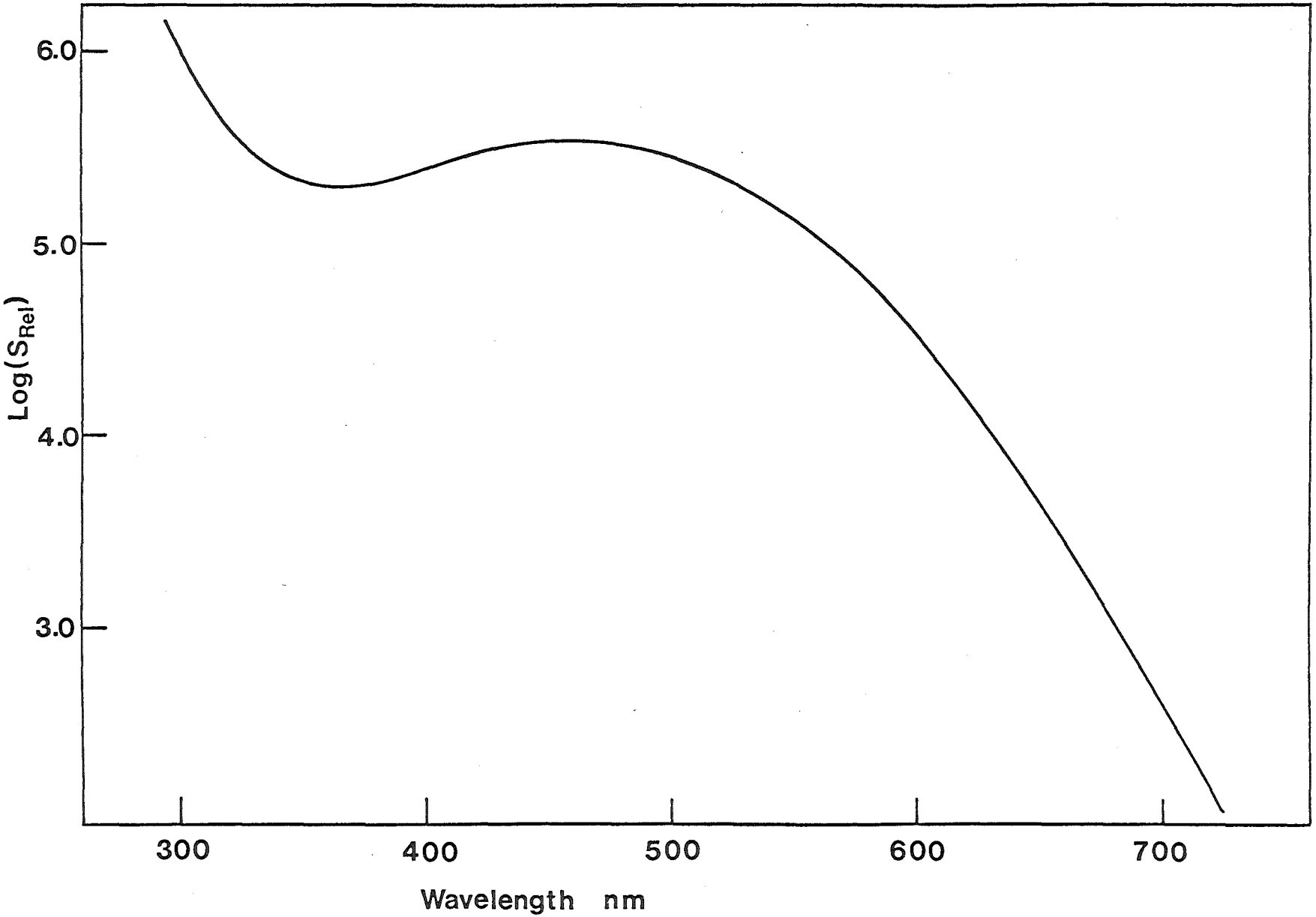

Fig. 5 Sensitivity of the monochromator-photomultiplier system.

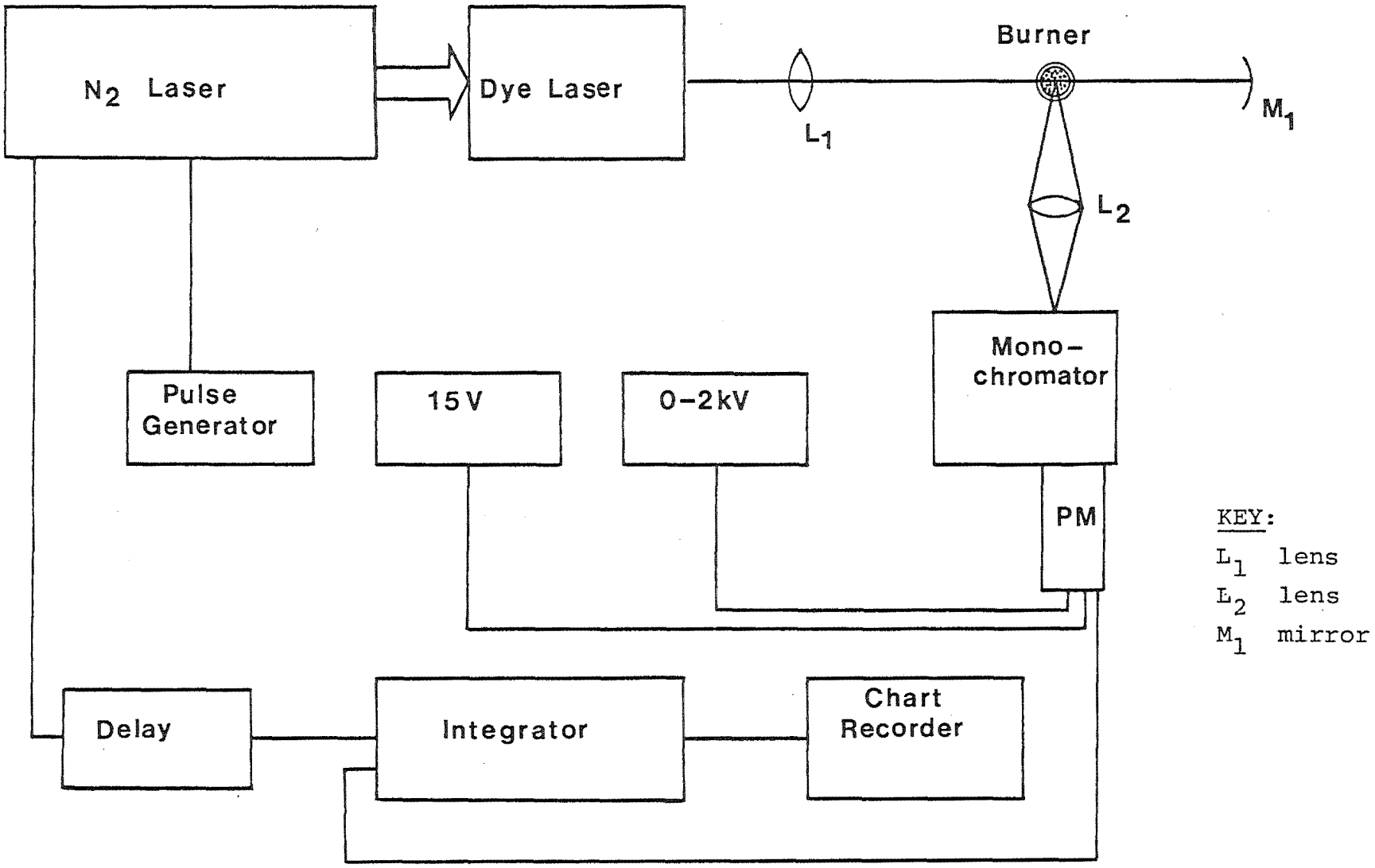

Fig. 6 Schematic representation of the laser fluorescence experimental apparatus.

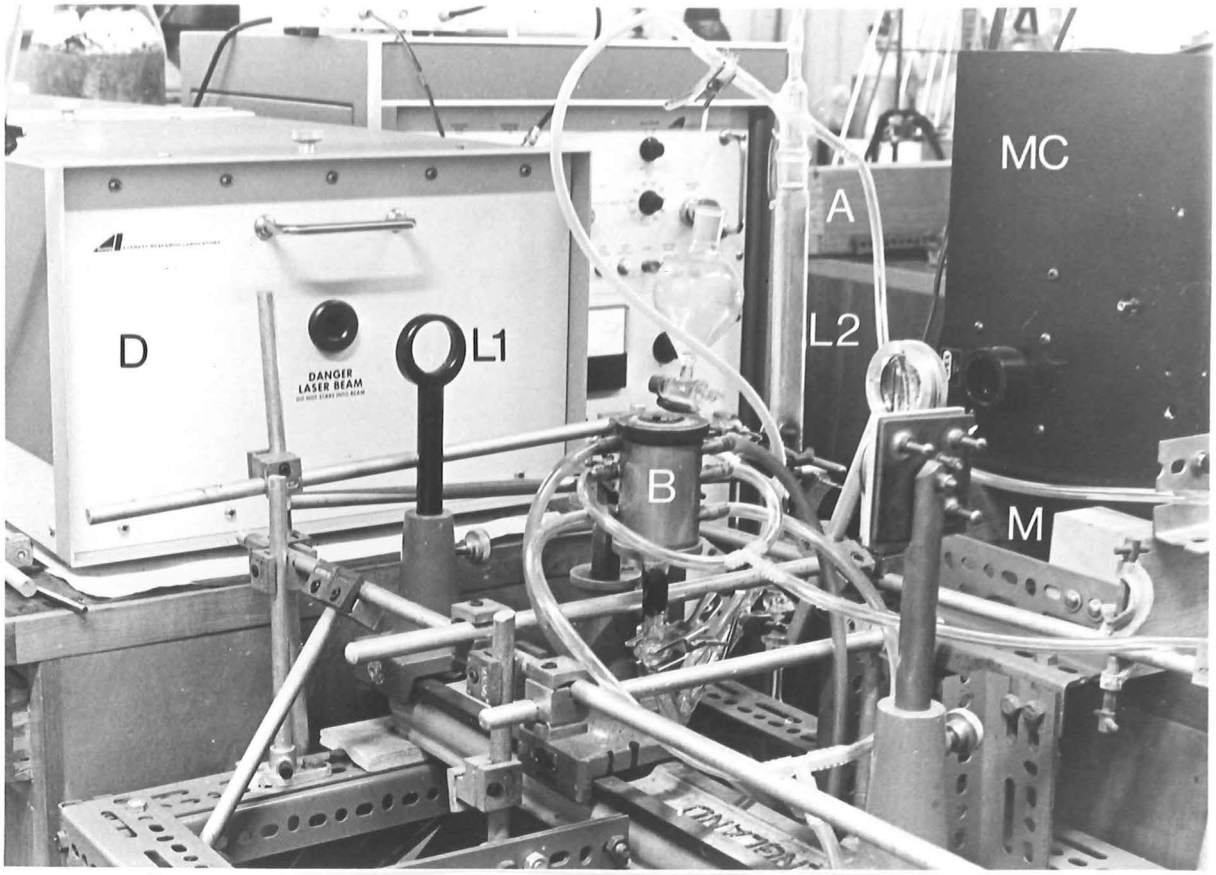

PLATE 1: Experimental apparatus layout

A	Atomiser
B	Burner
L_1	Laser focussing lens
L_2	Fluorescence collection lens
M	Concave mirror
D	Dye laser
MC	Monochromator

height in the flame, but displaced laterally by approximately 1 mm to 2 mm. Fluorescence intensity fluctuations due to minor flame instability were minimal, due to the flatness of the machined burner face, and hence of the flame front.

Fluorescence from the flame was focussed by lens L_2 onto the entrance slit of a SPEX MINIMATE monochromator (operated with a resolution of 1 nm) and monitored with an EMI 6255 photomultiplier. The lens system and burner were mounted on an optical bench which was rigidly bolted to a steel framework.

VII. ELECTRONIC MEASUREMENTS

The output of the photomultiplier was fed into a low-noise FET amplifier, the design of which is due to Mr R.L. Hooper and is given in appendix I, having a voltage gain of 3 and a 50 Ω output impedance. By varying the input resistor of this amplifier it was possible to obtain a preintegrated pulse of 3 μs from the fluorescence signal which had a lifetime of the order of nanoseconds. With the RC time constant of the amplifier input equal to 3 μs, all pulses shorter than about 0.3 μs were integrated, and the amplifier produced an output signal with peak amplitude proportional to the integrated fluorescence intensity, which can also be expressed as the number of photons collected during the pulse.

Preintegration of the signal in this manner allowed a longer gate width to be used, resulting in a smaller

duty factor* for the gated integrator, and hence better integration. The effects of laser trigger jitter and R.F. interference are minimised with preintegration[17].

The preintegrated signal was fed into a gated integrator which was constructed in the laboratory by Professor L.F. Phillips. This was gated open by a synchronising pulse which was brought from the laser, via a variable delay unit, also constructed in the laboratory. Synchronising pulses generated by the laser occur some 0.3 μs before the laser flash, and by suitable choice of delay time, coincidence of the laser fluorescence signal and the gate opening was obtained. The integrator gate width was normally set at 5 μs. The output was displayed on a digital voltmeter and also presented on a YOKOGAWA chart recorder.

In order to establish that the system responded linearly to fluorescence intensity, the fluorescence of lead was measured as a function of lead atom concentration, introduced to the flame as a fine spray of a solution of lead nitrate. Laser excitation at 405.8 nm was used to excite metastable Pb($6p\ ^3P_1$) to Pb($7s\ ^3P_1^o$) and the fluorescence at 364.0 nm due to the transition $7s\ ^3P_1^o \rightarrow 6p\ ^3P_0$ was measured for varying concentrations of lead in the atomiser solution. A plot of fluorescence intensity versus [Pb] in the atomiser solution is presented in fig. 7.

---

* Duty factor = $\frac{1}{f.t.}$: f = Repetition rate

t = gate width

Effective Time Constant = $RC_{eff} = \frac{RC\ (gate)}{f.t.}$

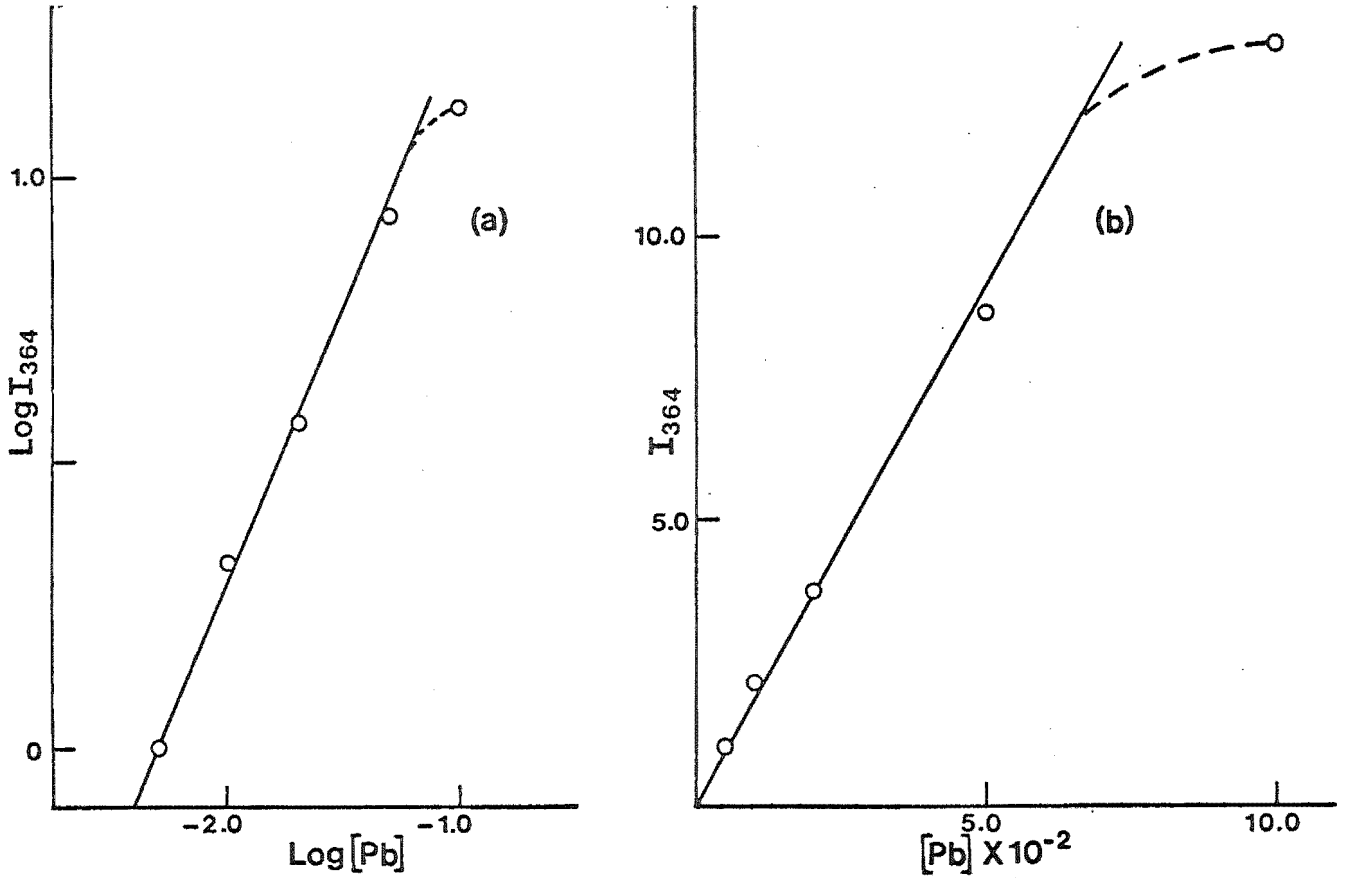

Fig. 7 Response of the fluorescence detection system to the fluorescence of lead at 364.0nm (a) Log I_{364} vs Log[Pb], slope = 1.0
(b) linear plot of measured intensity I_{364} vs [Pb]: [Pb] is the concentration of lead in the atomiser and is thus proportional to the number of lead atoms in the flame. [Pb] is in moles l^{-1}.

The point at [Pb] = 0.1 M corresponds to integrator overload, however all fluorescence measurements were made on the linear portion of the graph, and in the case of lead fluorescence, [Pb] was set at 10^{-2} M.

CHAPTER III

LASER STUDIES OF MINORITY SPECIES IN FLAMES

I. INTRODUCTION

This chapter describes the preliminary work which was done in a search for suitable minority species, or trace additives in flames, e.g. metal atoms or free radicals, for which laser fluorescence studies would provide information on the kinetics of various important processes in flames.

The laser fluorescence system as described in Chapter II, section VI, was used and has the principle advantages associated with laser techniques, that is, a high intensity light source, high monochromaticity (approx 0.1 nm), and good spatial resolution, as laser light can be focussed down to a very small spot. The use of a tunable dye laser enables studies to be carried out anywhere in the visible spectrum with suitable choice of dye, and frequency doubling can be used to extend the range into the ultraviolet.

In the course of the work, laser fluorescence has been used in attempts to characterise species such as NH, CH, SO_2, Tl, Cu, Na, and Pb. The following sections, II to IV, describe briefly the work on each species, leading up to the fluorescence studies on lead in which it was found that the intensities of the two emission lines at 368.3 nm and 364.0 nm could be used to obtain kinetic information on the spin-orbit relaxation process

$$Pb(7s\ ^3P_1^o) + M \rightarrow Pb(7s\ ^3P_0^o) + M \qquad 3.1$$

where M is a flame species such as flame radicals H, OH, or a bulk constituent such as H_2, H_2O, N_2.

II. METHYLIDYNE: CH

The role of the free radical CH in the production of soot in hydrocarbon combustion has been extensively studied and is reviewed by Lester and Wittig[18]. Much work has been done with emission and absorption techniques but these are often complicated due to the fact that CH profiles do not always match those of CH* emission[19] due to reactions such as

$$C_2 + OH \rightarrow CO + CH^* \qquad 3.2$$

$$C_2H + O \rightarrow CO + CH \qquad 3.3$$

Hayhurst[20] has indicated that species such as $C_3H_3^+$ are primary ions in the production of soot, as well as the well known CHO^+, and arise from processes such as

$$CH^* + C_2H_2 \rightarrow C_3H_3^+ + e^- \qquad 3.4$$

but is is suggested that CH* may not necessarily need to be excited. The idea that $C_3H_3^+$ is a primary ion is also suggested by Bowser[21] in shock tube studies using pure acetylene; however, CH is not observed. The vast number of reactions and products in a hydrocarbon flame contribute to the difficulty of any study made on them, however Bascombe[22] has made mass spectrometric studies of ions in $H_2/N_2/O_2$ flames seeded with a small amount of acetylene (about 1%). Attempts at monitoring CH via fluorescence have been made by Bulewicz et al[23], but were unsuccessful

because of high flame-emission noise. Barnes et al[24], were successful in measuring CH laser fluorescence at 431.5 nm ((0,0) band of $A^2\Delta \rightarrow X^2\Pi$) in an oxyacetylene flame.

The fluorescence experiment of Barnes et al[24] was reproduced in the present work in an unmetered oxyacetylene flame supported on a commercial welding torch. The fluorescence spectrum obtained is shown in fig. 8. It is interesting to note that the fluorescence spectrum disappeared when the supply of oxygen was reduced, and the flame made more fuel-rich, in agreement with Porter's mechanism[19] for the production of CH, which is given in 3.5

$$C_2H + O \rightarrow CO + CH \qquad 3.5$$

As noted by Barnes et al[24], the ground state CH was found to be localised in the thin reaction zone at the boundary of the inner core of the flame, which suggests the presence of very fast reactions which remove CH.

The well-defined structure and kinetics of $H_2/N_2/O_2$ flames (Fristrom and Westenberg[76]) enables them to be used as an excellent high temperature reaction medium for the study of minority species introduced to them. CH has been studied in emission and absorption in $H_2/N_2/O_2$ flames by Peeters et al[25], and Bulewicz et al[23]. In the present work it was hoped that the fluorescence of CH in oxy-acetylene flames could be extended to a study in premixed laminar $H_2/N_2/O_2$ flames.

Hydrocarbons were introduced to a wide range of premixed $H_2/N_2/O_2$ flames, as gases such as acetylene, methane and ethane. The flames used, varied from cool fuel-rich flames (T ~ 1500 K) to hot oxygen-rich flames

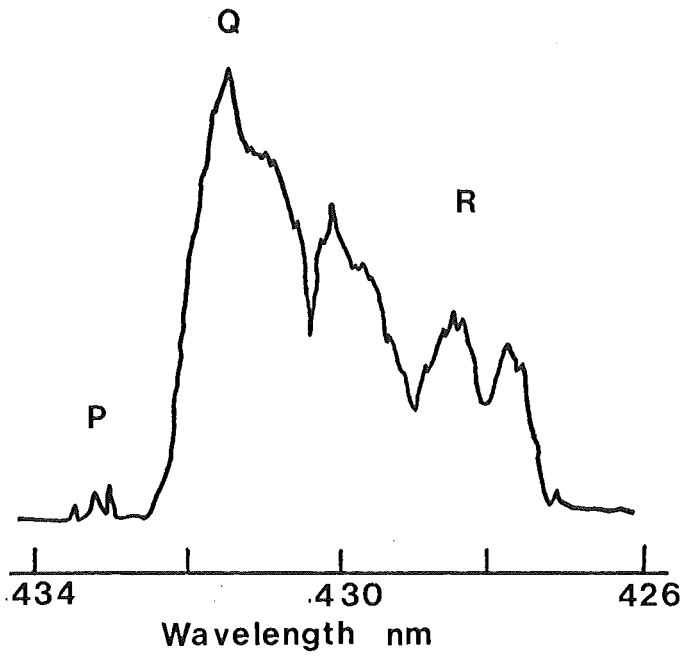

Fig. 8 Fluorescence spectrum of the (0,0) band of CH ($A^2\Delta \rightarrow {}^2X\Pi$) excited in the reaction zone of an oxy-acetylene flame at 431.5 nm.
Laser line width was 0.1 nm.

(T ~ 2500 K) and were supported on the burner described in chapter II, section I.

The experimental arrangement is as described in Chapter II, section VI, except that for some runs a special mirror system was devised so that the laser pulse could be made to traverse the flame up to six times. The laser pulse was obtained from the dye laser as shown in fig. 6, with a 5 x 10^{-4} molar solution of dimethyl POPOP in n-BuOH[26], operated at 100 Hz. Resonance fluorescence of CH at 431.5 nm, due to the $A^2\Delta \rightarrow X^2\Pi$ transition, was not observed in any of the $H_2/N_2/O_2$ flames, even at very high concentrations of additive (up to 10%) and at this stage it was decided to discontinue the study of CH fluorescence.

III. IMIDOGEN: NH

The importance of the free radical imidogen, NH, has been discussed by Nadler[27] in relation to reactions with free atomic oxygen and nitrogen in $NH_3/O_2/N_2$ flames. Further studies[28] revealed that the reactions 3.6 and 3.7 needed to be included in reaction schemes in order to account for observed concentration profiles.

$$NH + NO \xrightarrow{k_{3.6}} N_2 + OH \qquad 3.6$$

$$NH_2 + NO \xrightarrow{k_{3.7}} N_2 + OH_2 \qquad 3.7$$

Unfortunately their values for $k_{3.6}$ and $k_{3.7}$ differed from flash radiolysis determinations[29], by factors of about 10^3. The rate constant $k_{3.6}$ has more recently been measured[30], using fluorescence studies with microwave discharges, and

other studies[31,32] using NH fluorescence have been made on the kinetics of NH and O_2. Laser fluorescence of NH_2 has been reported[33,34], and recently, laser excited fluorescence of NH has been observed by Anderson[35] using dye laser excitation, and in a private communication to Anderson, laser fluorescence in flames has also been reported. However, the work in this thesis on NH was discontinued before this observation.

NH was produced in a series of $H_2/N_2/O_2$ flames by the addition of a small amount (about 1%) of NH_3 to the unburnt gases. Excitation at 337.1 nm, corresponding approximately to the $^3\Sigma \rightarrow {}^3\Pi$ transition, was provided from the output of a N_2 laser focussed into the flame. Fluorescence was not observed, even for a wide range of experimental conditions. This was probably due to the low concentration of NH in the flames studied.

IV. OTHER STUDIES, INCLUDING Tl, Na, Cu, Cs, Sn, Pb

Other fluorescence studies initiated in the present work involved laser fluorescence of thallium, sodium, copper, caesium, tin and lead. In the case of these metal atoms, the work was intended to yield height profiles of the absorbing species ($Tl\ ^2P_{3/2}$) or information about non-adiabatic collisions (Cu, Na, Pb, Cs, Sn).

Thallium was excited at 535.0 nm corresponding to the $6\ ^2P_{3/2} \rightarrow 7\ ^2S_{1/2}$ transition, in an excited-state laser fluorescence experiment. Metastable thallium atoms were previously observed using laser fluorescence by Fraser[36]. The fluorescence intensity at 535.0 nm was observed as a

function of distance from the flame reaction zone, and was found to have the form expected for thermal excitation to the metastable 6 $^3P_{3/2}$ state. Some flame profiles are presented in fig. 9. The observed profiles are consistent with the observations of Padley and Sugden[37].

Initial experiments involving the fluorescence of lead showed that the collision induced spin-orbit relaxation process 3.1, was important for hydrogen atoms as the colliding partner, and so the fluorescence of other species with closely lying upper energy levels (ΔE about 300 cm^{-1}) was investigated.

The resonance fluorescence of sodium (at 589.0 nm and 589.6 nm) and the fluorescence of copper (excitation at 510.5 nm and fluorescence intensity ratios at 570 / 578.2 and 324.7/327.3 nm) showed no changes with changing hydrogen atom concentration. Caesium was also added to a few flames and excited at both 455.5 nm and 459.3 nm in separate experiments. Fluorescence at the two wavelengths was monitored for both excitations, but laser scattering at these wavelengths was exceptionally strong and any fluorescence was masked by instrument overload. Experiments with tin as an additive were also unsuccessful, due to the formation of the stable tin oxide SnO (D_o = 521.0 $kJ.mol^{-1}$). At this stage it was decided to direct the course of work toward the more promising study of lead fluorescence.

$$Pb(^3P_1{}^o) + M \rightarrow Pb(^3P_0{}^o) + M^* \qquad 3.1$$

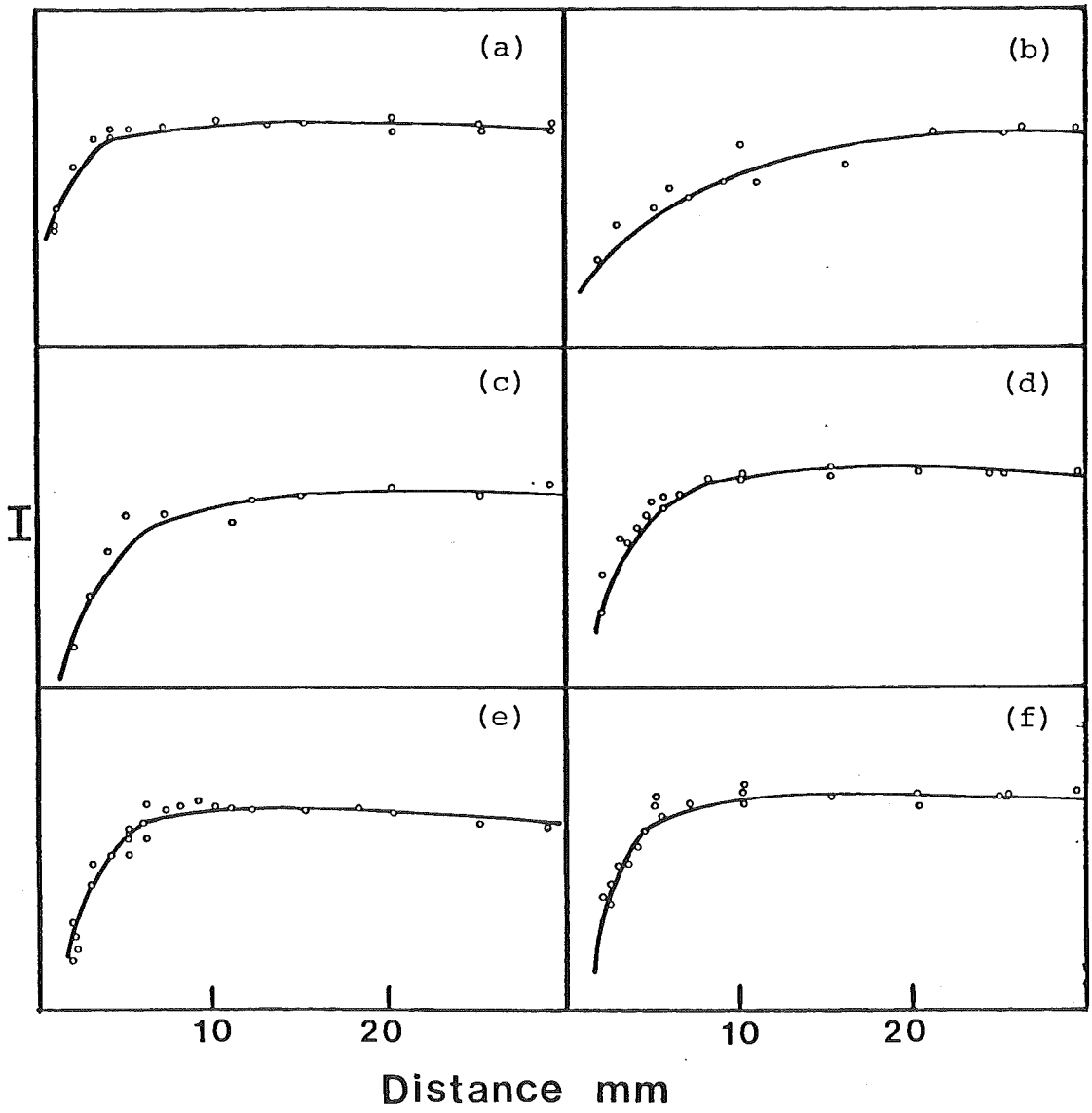

Fig. 9 Flame profiles of Thallium fluorescence Intensity I at 535.0 nm plotted as a function of distance from the reaction zone.

(a) flame Z5; T = 1807 K

(b) flame Z4; T = 1945 K

(c) flame Z6; T = 1696 K

(d) flame P4; T = 2120 K

(e) flame F6; T = 1927 K

(f) flame Z8; T = 1500 K

V. FLUORESCENCE OF LEAD

INTRODUCTION

Laser excited fluorescence of lead has been used for quantitative analysis by Kuhl and Spitschan[39] with excitation at 283.3 nm and fluorescence at 405.8 nm, and saturation studies of the metastable state $6p^2\ ^3P$ have been made using laser fluorescence by Bolshov et al[40]. Measurements of the quenching rates of excited lead atoms have been made by Jenkins[41] (7s $^3P_1^o$ state in flames), Mandl and Chen[42] (7s $^3P_1^o$ state in a heated cell at 900 K), and Husain and Littler[45] ($^1S_0$ and $^1D_2$ states from photolysis of tetraethyl lead). It has been shown, by Friswell and Jenkins[46], that under fuel-rich conditions in flames, Pb exists almost entirely as free atoms, however under fuel-lean conditions significant amounts of PbO are formed.

The relevant energy levels of Pb are represented in fig. 10 and are taken from Moore[47]. Fig. 10 also indicates the allowed transitions and lists the Einstein A coefficients.

In the determination of quenching rate constants for Pb(7s $^3P_1^o$), using atomic fluorescence, Jenkins[41] noted that the relative intensities of the lines at 368.3 nm, 364.0 nm and 405.8 nm had a non equilibrium ratio compared with values expected on the basis of complete equilibration between the 7s($^3P_1^o$) and 7s($^3P_0^o$) states. As expected, the $I_{405.8nm} : I_{364.0nm}$ ratio was correct, as these emissions originate from the same state, ($^3P_1^o$). However, the $I_{368.3} : I_{364.0}$ ratio was well below that

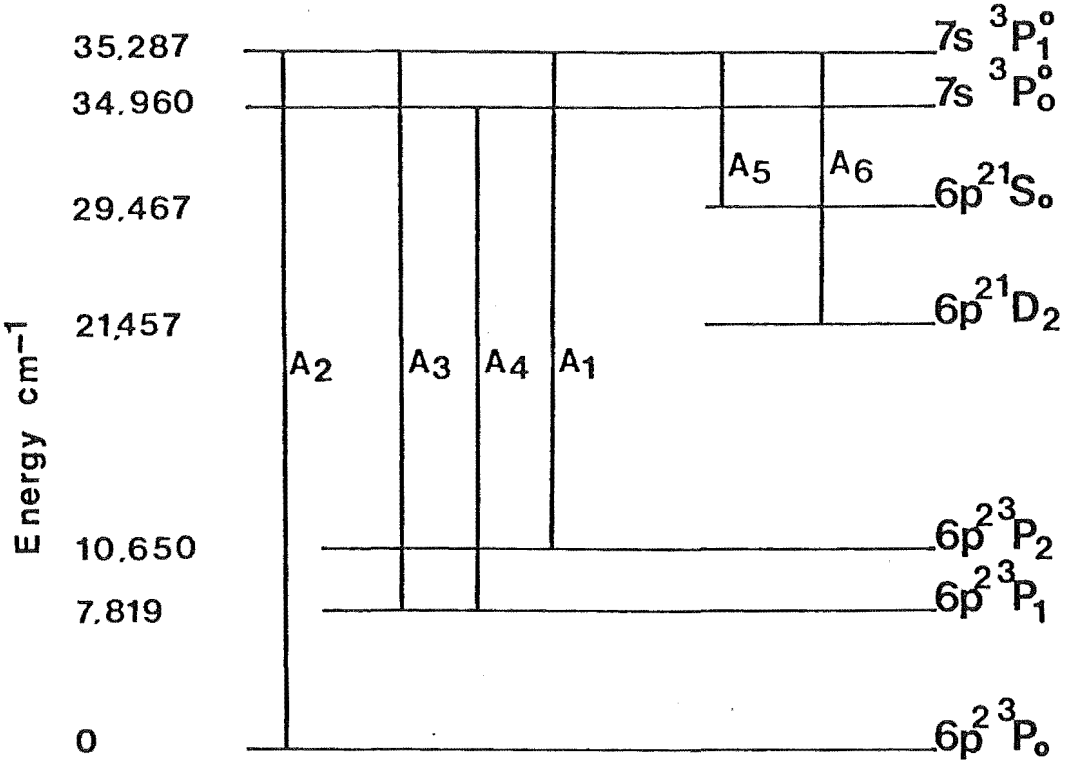

Fig. 10 Partial energy level diagram for lead. The values of the Einstein A coefficients used in this work are listed and referenced below.

A_1(104.8nm) = $9.65 \times 10^7 s^{-1}$. de Zaffra and Marshall [43]

A_2(283.3nm) = $5.28 \times 10^7 s^{-1}$. de Zaffra and Marshall

A_3(364.0nm) = $2.99 \times 10^7 s^{-1}$. de Zaffra and Marshall

A_4(368.3nm) = $1.72 \times 10^8 s^{-1}$. Penkin and Slavenas [44]

Energy levels not to scale.

corresponding to complete equilibrium, with r = 0.062 and r_e = 0.462 for the ratios of concentrations of the two states $^3P_1{}^0$ and $^3P_0{}^o$, where $r = \frac{N(^3P_0{}^o)}{N(^3P_1{}^o)}$. Jenkins accounted for this discrepancy by assuming that the Pb(7s $^3P_1{}^o$) → Pb(7s $^3P_0{}^o$) inter-level transfer was considerably slower than other de-excitation processes. It was also shown, that the state Pb($6p^2$ $^3P_1$) is populated by chemi-excitation, via reactions such as

$$H + OH + Pb \rightarrow H_2O + Pb^* \qquad 3.8$$

$$H + H + Pb \rightarrow H_2 + Pb^* \qquad 3.9$$

In the present work, laser fluorescence has been used to study the processes involved in the inter-level transfer of 3.10.

$$Pb(7s\ ^3P_1{}^o) \rightarrow Pb(7s\ ^3P_0{}^o) \qquad 3.10$$

Rate constants have been obtained for the reaction 3.1 where M is a hydrogen atom, and where M is a bulk constituent, including N_2, H_2, H_2O.

$$Pb(7s\ ^3P_1{}^o) + M \rightarrow Pb(7s\ ^3P_0{}^o) + M^* \qquad 3.1$$

FLUORESCENCE STUDIES

Lead was introduced to a series of premixed, laminar-flow, hydrogen-rich $H_2/N_2/O_2$ flames, ranging from Z8 (1500 K) to A4 (2385 K), as a fine spray of lead nitrate. Chemi-excitation and thermal excitation to the metastable Pb($6p^2$ $^3P_2$) state, and to Pb($6p^2$ $^3P_1$) state allowed laser excitation to the 7s $^3P_1{}^o$ and 7s $^3P_0{}^o$ states respectively in separate experiments. Fluorescence at 368.3, 364.0 and 405.8 nm was monitored using the

experimental scheme represented in fig. 6.

The study involved two fluorescence schemes. In the first set of experiments laser excitation at 405.8 nm (using the dye α-NND) was used to populate the state 7s $^3P_1^o$, and fluorescence was monitored at 368.3 nm (7s $^3P_0^o \rightarrow$ 6p $^3P_1$) and at 364.0 nm (7s $^3P_1^o \rightarrow$ 6p $^3P_1$). In the second set, excitation at 368.3 nm (using the dye PBD) was used to populate the state 7s $^3P_0^o$, and fluorescence was monitored at 368.3 nm (7s $^3P_0^o \rightarrow$ 6p $^3P_1$) and at 405.8 nm (7s $^3P_1^o \rightarrow$ 6p $^3P_2$). A representative diagram is presented in fig. 11 and illustrates both experimental schemes.

In the first case, represented in fig. 11(a), fluorescence intensities were obtained by tuning the spectrometer to 364.0 nm and measuring the background with no lead added to the flame; lead was then introduced to the flame and the signal averaged over about 30 seconds. The spectrometer was then tuned to the line at 368.3 nm and the signal averaged over a similar period of time. There was no signal recorded due to emission at either 368.3 nm or 364.0 nm. These measurements were repeated at millimeter randomised intervals of distance from the reaction zone in the flame, and repeated several times for each flame. About 50 to 60 measurements were taken in each flame from 0 - 28 mm, weighted significantly in the region close to the reaction zone, i.e. 0 - 10 mm, in order to define the region of greatest change in fluorescence ratio more accurately. The signal to noise ratio varied from flame to flame, the cool flames having considerably better S/N ratio than hot ones in which thermal emission was more

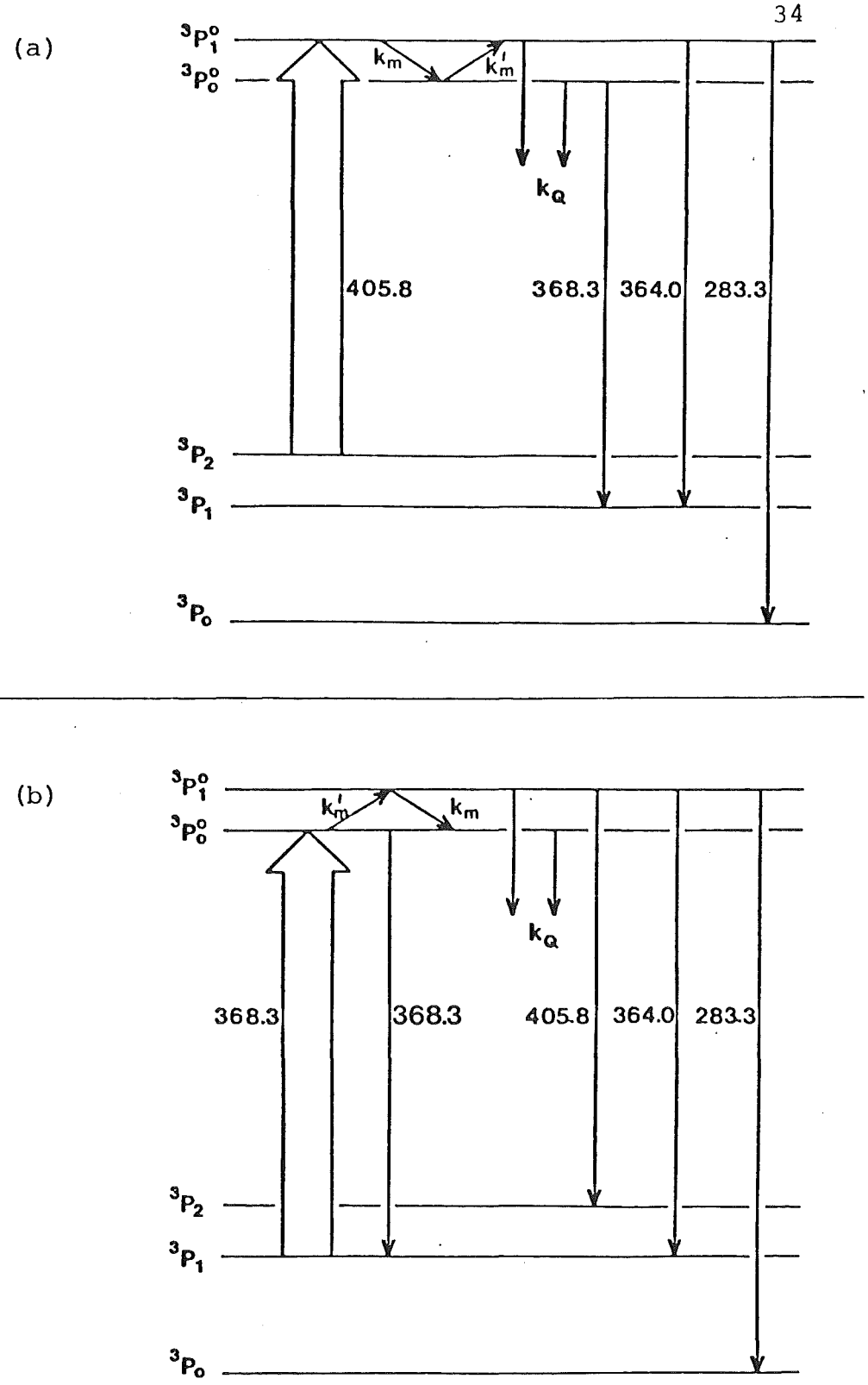

Fig. 11 Schematic representation of fluorescence experiments: (a) excitation at 405.8 nm and fluorescence observed at 368.3 and 364.0 nm: (b) excitation at 368.3 nm and fluorescence observed at 368.3 and 405.8 nm.

pronounced. In all cases, S/N ratio was better than 7:1 and 3:1 for 364.0 and 368.3 nm respectively. A typical fluorescence spectrum is presented in fig. 12 along with a background scan.

In the second set of experiments, fluorescence intensities were superimposed on the scattered laser signal at 368.3 nm. It was established that there was no background contribution at 364.0, 368.3 and 405.8 nm from flame emission, with Pb introduced to the flame (see fig. 13). The signal due to the scattering at 368.3 nm (with no Pb added to the flame) was first measured and averaged for about 30 sec. Lead was then sprayed into the flame and the resulting signals at 368.3 nm and 405.8 nm were measured, again averaging at each wavelength for about 30-60 sec. for each point measured. This procedure was repeated for a number of points in the flame at distances of 0 - 28 mm from the reaction zone, in order to obtain a flame profile. It was important to take background measurements at each distance from the reaction zone, to take account of stray laser scattering off the burner face. A fluorescence scan indicating the relative intensities of fluorescence and background is shown in fig. 13. The signal to noise ratio in all runs was better than 7:1 and 3:1 for the lines at 368.3 and 405.8 respectively.

FLUORESCENCE RESULTS

For the excitation at 405.8 nm, the fluorescence at 368.3 nm was compared to that at 364.0 nm and the ratio r plotted as a function of distance from the reaction zone,

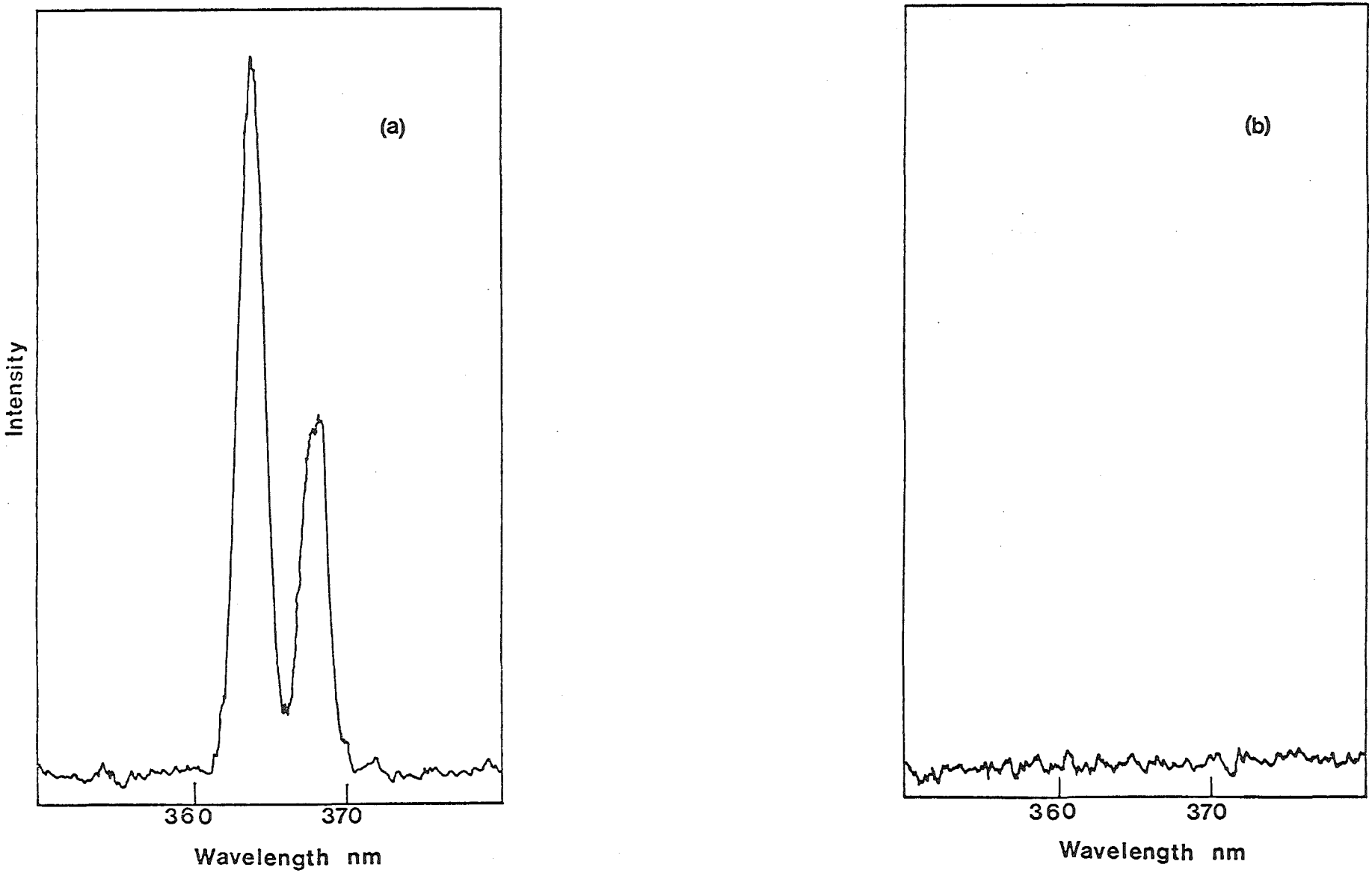

Fig. 12 Pb fluorescence excited at 405.8 nm: (a) Typical scan of lines at 364.0 and 368.3 nm, gain = 1; (b) background scan, laser off and Pb in flame, gain = 3.

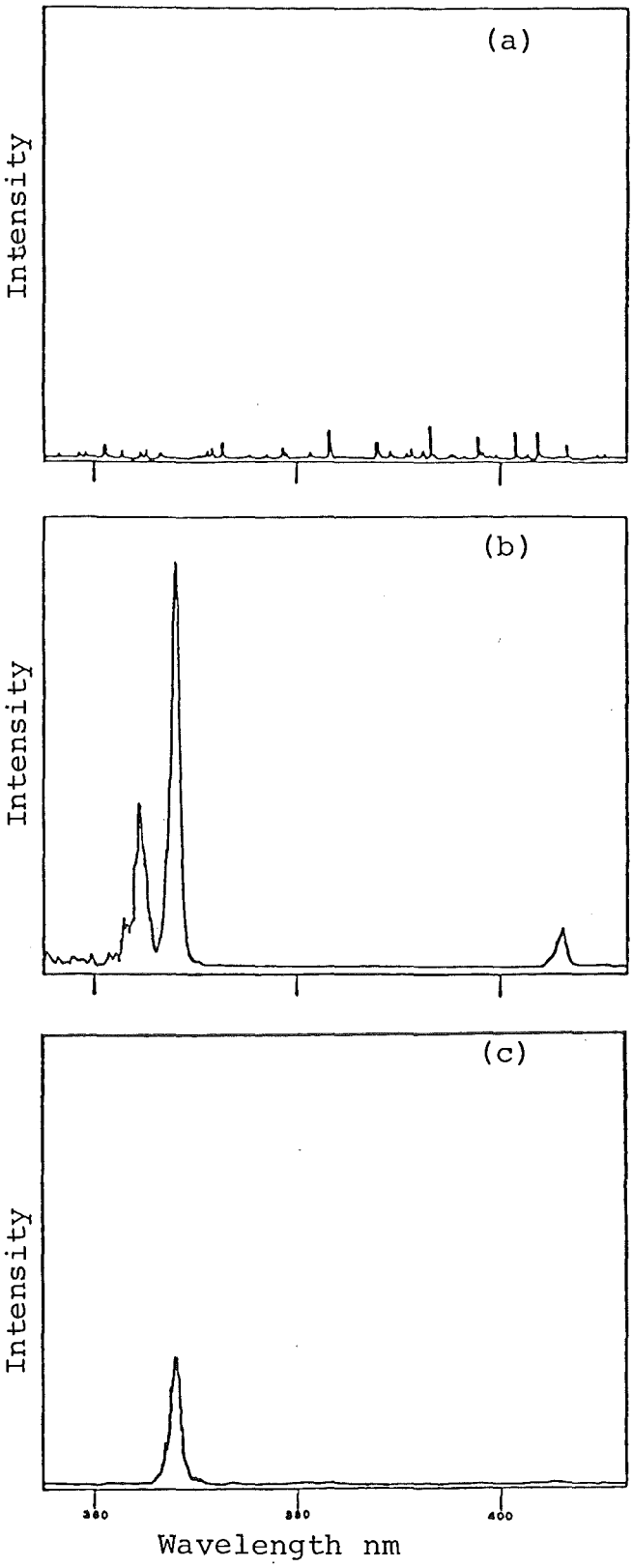

Fig 13 Typical spectra of Pb fluorescence excited at 368.3 nm in flame Z6.
(a) Background only, laser off, Pb added to flame, gain = 100; (b) Pb fluorescence at 368.3, and 405.8 nm. Gain at 364.0 nm = 20, gain at 368.3 and 405.8 nm = 1.
(c) Scattered laser light at 368.3 nm, gain = 1, no Pb added.

where

$$r = \frac{I_{368.3nm}}{I_{364.0nm}} \qquad 3.11$$

Figure 14 presents some typical results of such plots, and it can be seen that as noted by Jenkins[41], the ratio r is considerably lower than that expected if there were complete equilibration between the two states 7s $^3P_1^o$ and 7s $^3P_0^o$. For example, at 1400 K, if equilibrium existed between the two states, r_e = 2.686 and at 1800 K the ratio would be r_e = 2.49. The other important feature of the plots given in fig. 14, is that there is a marked increase in r close to the reaction zone for all flames, and there is a levelling out to a constant value in the post reaction-zone gas stream. This feature strongly implies that the relaxation process 3.1

$$Pb(^3P_1^o) + M \rightarrow Pb(^3P_0^o) + M^* \qquad 3.1$$

is most effective, when M is a flame radical such as H, OH or O, since all other species such as H_2, O_2, N_2, H_2O reach a near steady state value within the reaction zone, and it is only by relatively slow termolecular reactions in the post reaction zone gas stream that H, OH, and O are removed[48].

In the set of experiments using excitation at 368.3 nm, the fluorescence at 368.3 nm was compared to that at 405.8 nm after a correction to allow for the difference in spectrometer/photomultiplier sensitivity had been made. The ratio of the two intensities, denoted as r', is given by

$$r' = \frac{I_{405.8nm}}{I_{368.3nm}} \qquad 3.12$$

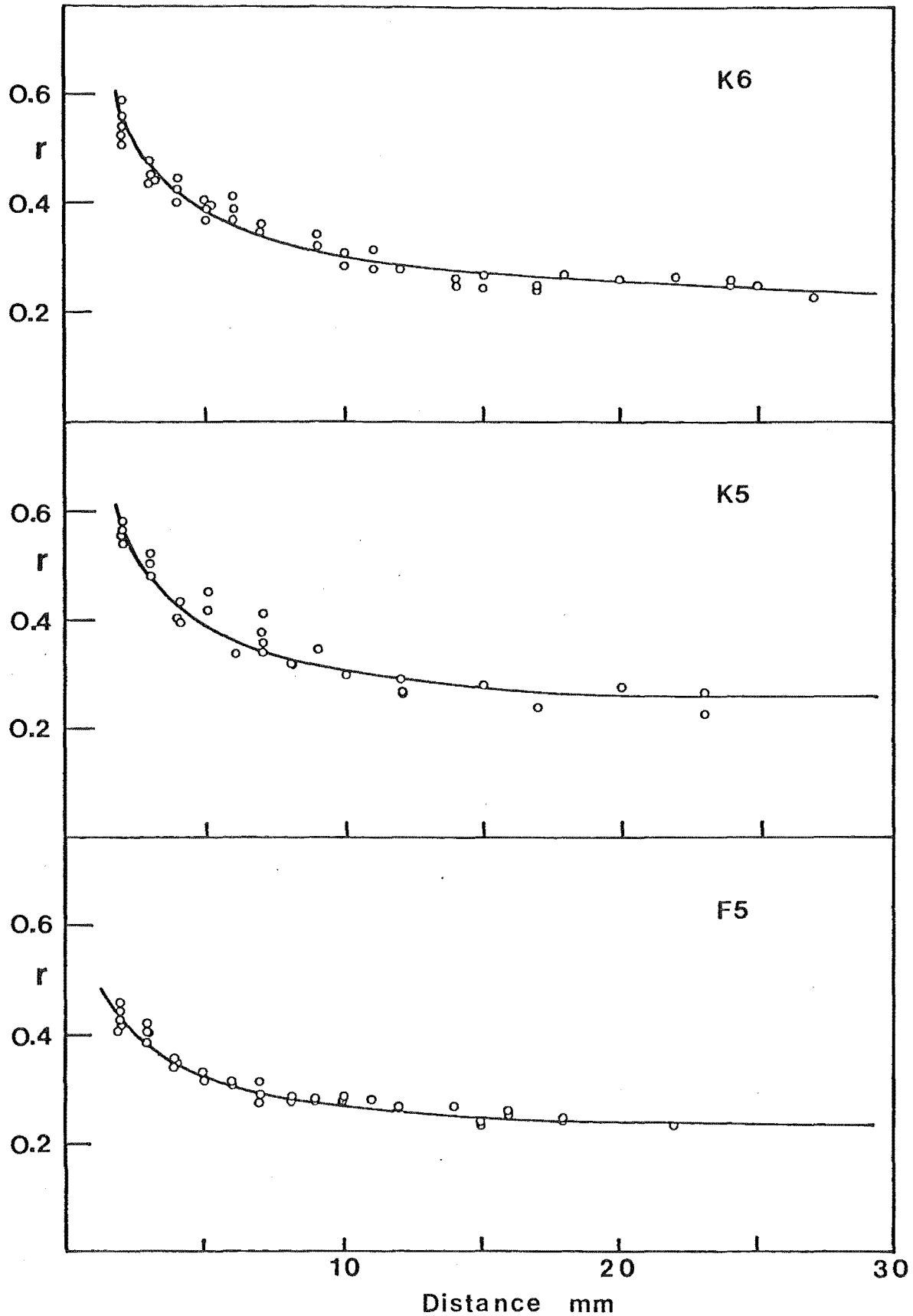

Fig. 14(a) Fluorescence ratio $r = \frac{I_{368.3}}{I_{364.0}}$ as a function of distance from the burner face. Excitation at 405.8 nm.

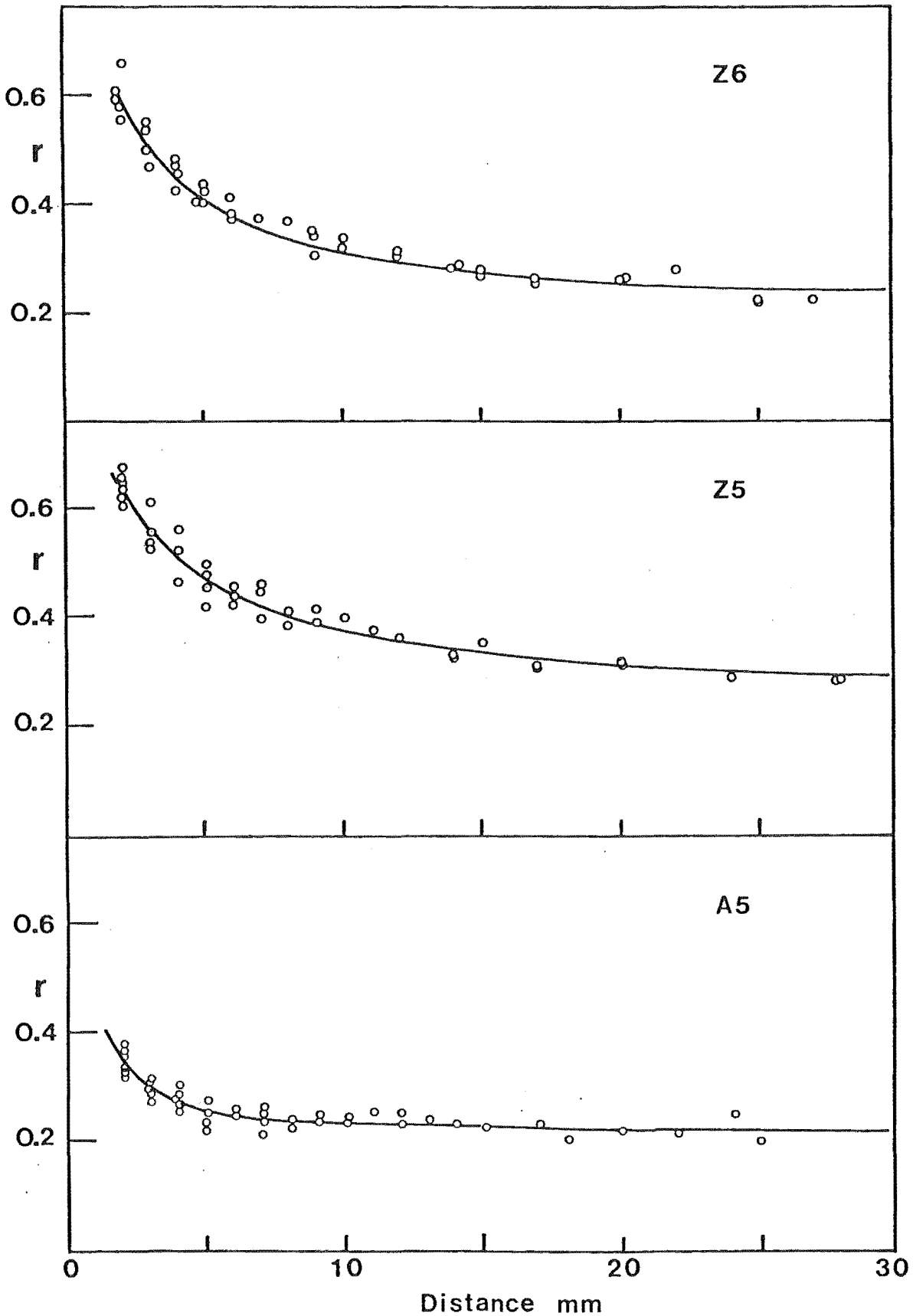

Fig. 14(b) Fluorescence ratio $r = \frac{I_{368.3}}{I_{364.0}}$ as a function of distance from the burner face.

Results for some typical flames are presented in figure 15, where r' is plotted as a function of distance from the reaction zone. Again it is noted that the populations of $^3P_1^o$ and $^3P_0^o$ do not reach their equilibrium values, since at 1400 K, $r'_e = 1.2$ and at 1800 K, $r'_e = 1.29$. The marked increase in r' near the reaction zone is again present, this time indicating that the reverse process of 3.1, namely 3.13

$$Pb(^3P_0^o) + M^* \rightarrow Pb(^3P_1^o) + M \qquad 3.13$$

is most effective when M is a flame radical.

The values of r obtained by Jenkins[41] at 1 cm from the reaction zone of his hydrogen and oxygen flames, diluted with various gases, are in agreement with those found in the present work. Unfortunately, an exact comparison cannot be made, since the compositions of the flames of Jenkins, and their temperatures, do not coincide with the present work; however, a value quoted for concentration ratios at 1 cm in a flame for which T = 1400° K, gives r = 0.356 which compares favourably with the results of this work.

In order to establish the dependence of r and r' on flame radicals, it is necessary to consider the various processes which characterise the structure of $H_2/N_2/O_2$ flames, and establish the dependence of flame radicals on composition and time. Chapter IV deals with this and obtains the dependence of r and r' on flame radicals.

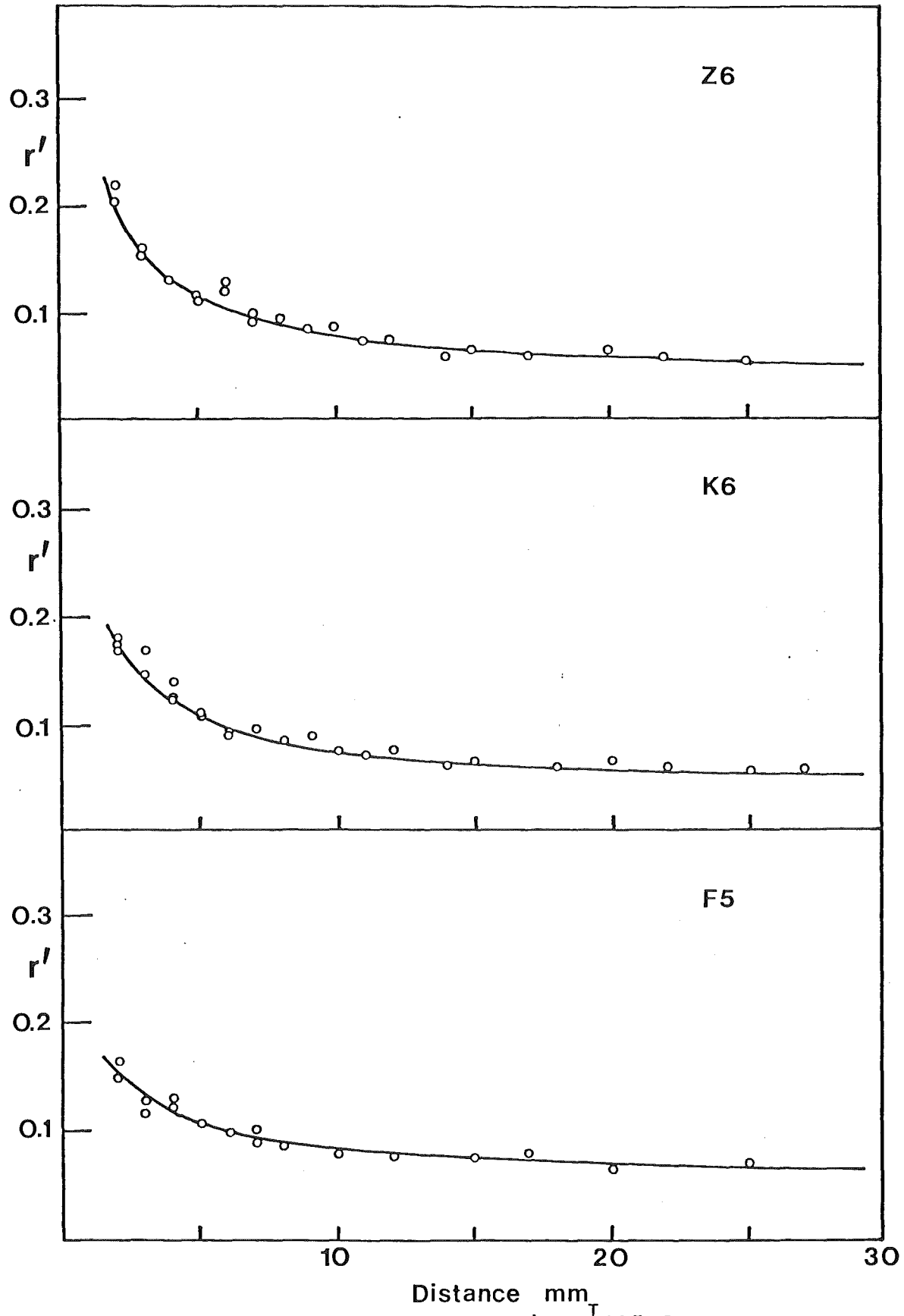

Fig. 15 Fluorescence ratio $r' = \frac{I_{405.8}}{I_{368.3}}$ as function of distance from the burner face. Excitation at 368.3 nm.

CHAPTER IV

LEAD FLUORESCENCE AND HYDROGEN ATOM CONCENTRATION

I. INTRODUCTION

In many flames, radicals exist in concentrations far in excess of their thermodynamic equilibrium values[49,50]; however, it is possible to relate the concentrations of H, OH, and O to the concentrations of the bulk constituents by way of the following reactions which are at equilibrium:

$$H + H_2O \overset{K_1}{\rightarrow} OH + H_2 \qquad 4.1$$

$$OH + OH \overset{K_2}{\rightarrow} H_2O + O \qquad 4.2$$

$$H + OH \overset{K_3}{\rightarrow} H_2 + O \qquad 4.3$$

$$H + O_2 \overset{K_4}{\rightarrow} OH + O \qquad 4.4$$

If the concentration of one radical species (usually H) is known absolutely these equilibria enable the concentrations of other radicals to be calculated from the known equilibrium constants and concentrations of bulk constituents H_2 and H_2O

At flame temperatures, the reactions 4.1 to 4.4 are fast, and the equilibria are rapidly established[49]. Thus we have:

$$[OH] = K_1[H][H_2O]/[H_2] \qquad 4.5$$

$$[O] = K_1K_3[H]^2[H_2O]/[H_2]^2 \qquad 4.6$$

so that in a fuel-rich flame we can consider $[OH] \propto [H]$ and $[O] \propto [H]^2$.

II. RELATIVE [H] MEASUREMENT

In a hydrogen-rich flame, the concentration of free hydrogen atoms, [H], is related to the intensity of the CuH band at 428.0 nm, when copper is added to the flame[51]. Addition of a fine spray of an aqueous copper solution to a hydrogen flame leads to the production of excited copper hydride, CuH^*

$$Cu + H + M \rightarrow CuH^* + M \qquad 4.7$$

The transition of CuH^* to the ground state (0-0 band of $A \rightarrow X$) is accompanied by emission at 428.0 nm:

$$CuH^* \rightarrow CuH + h\nu_{428} \qquad 4.8$$

The intensity of emission is directly proportional to the concentration of H atoms in the flame gases, so that measurements of CuH emission may be used to determine relative [H] in a flame. It is important to note however, that the relative hydrogen atom concentration from point to point in a flame, determined in this manner, cannot be used to determine relative concentrations between different flames, due to a significant temperature coefficient of the emission at 428.0 nm[51].

Hydrogen atom concentration decay in the flame obeys pseudo second order kinetics[49], so [H] is related to time according to equation 4.9

$$\frac{1}{[H]} = \frac{1}{[H]_o} + kt \qquad 4.9$$

Hence a plot of $[H]^{-1}$ versus time (or distance) from the reaction zone is linear. Similarly a plot of $(I_{CuH}{}^*)^{-1}$ versus time (or distance) from the reaction zone is linear and absolute values of [H] determined at any point in the

flame may be used to scale the values of $(I_{CuH^*})^{-1}$ to reciprocal hydrogen atom concentrations at any other point in the flame.

Relative hydrogen atom concentrations were determined using this method for all flames studied in this work. Copper was added to the flame as an aqueous solution of 0.01 M copper nitrate. The emission at 428.0 nm was measured, using the photometric system described in Chapter II, at 0.5 mm intervals over the region 0 to 25 mm from the reaction zone. The position of the reaction zone was taken to correspond with peak [H], and was determined by observing the position of peak emission of the CuH band.

III. ABSOLUTE [H]

Absolute hydrogen atom concentrations were determined using the Li/LiOH method[49]. This method depends on the measurement of the fraction of added lithium in the flame which is combined in the form of lithium hydroxide according to equation 4.10

$$Li + H_2O \overset{K_{Li}}{\rightarrow} LiOH + H \qquad 4.10$$

If $[Li]_T$ is the total lithium added to the flame, then we have the relation:

$$\frac{[LiOH]}{[Li]} = \left(\frac{[Li]_T}{[Li]}\right) - 1 \qquad 4.11$$

Hence we have that

$$\left(\frac{[Li]_T}{[Li]}\right) - 1 = K_{Li}\frac{[H_2O]}{[H]} = \phi$$

where K_{Li} is the equilibrium constant of equation 4.10.

The ratio $[Li]_T/[Li]$ was obtained by comparison of emission intensities for the sodium-D lines at 589.0/589.6 nm and the close lithium doublet at 670.8 nm. Since sodium added to the flame is unaffected by reactions such as 4.10, a measurement of its concentration in the flame is a measure of total lithium which is added to the flame in a known ratio to the sodium concentration.

A mixed solution of 10^{-3} M sodium chloride and 2×10^{-2} M lithium acetate was sprayed into the flame from the atomiser and a number of measurements at 589.0/589.6 nm and 670.8 nm were made at each point in the flame. This was done for two or three points in the flame. The value of ϕ was calculated from the relative emission intensities using equation 4.12

$$1 + \phi = \frac{I_{Na} M_{Li} f_{Li} S_{Li} \lambda^2_{Na}}{I_{Li} M_{Na} f_{Na} S_{Na} \lambda^2_{Li}} \exp\left(\frac{h\nu_{Na} - h\nu_{Li}}{kT}\right) \qquad 4.12$$

where I_{Na} and I_{Li} are the intensities for Na at 589.0/589.6 nm and Li at 670.8 nm respectively, M are concentrations in the atomiser solution, f's are transition probabilities, S's are relative photometer sensitivities and λ's and ν's are the wavelengths and frequencies respectively for the resonance doublets.

The equilibrium constant K_{Li} was derived from molecular partition functions and is given in equation 4.13.

$$K_{Li} = h\frac{\pi^{\frac{1}{2}}}{8^{\frac{1}{2}}} \left(\frac{2\, M_{LiOH} M_H}{M_{Li} M_{H_2O}}\right)^{\frac{3}{2}} \left(\frac{I_{LiOH}}{I_{H_2O}}\right) \Pi \left(\frac{1-e^{-h\nu_{H_2O}/kT}}{1-e^{-h\nu_{LiOH}/kT}}\right) \times (kT)^{-\frac{1}{2}} \exp\left(\frac{-\Delta H^o(o)}{kT}\right)$$

where $I_{H_2O} = (I_x I_y I_z)^{\frac{1}{2}}$ 4.13

where M is the relative atomic or molecular mass in grams, and I stands for moment of inertia. The product

$$\Pi \frac{(1-e^{-\frac{h\nu_{H_2O}}{kT}})}{(1-e^{-\frac{h\nu_{LiOH}}{kT}})}$$

is taken over all the vibrations of H_2O and LiOH. LiOH was assumed to have linear structure[52]. The relevant vibrational data, and bond lengths and enthalpies of formation are given in appendix II and are taken from the JANAF thermochemical tables[53]. Numerical values of K_{Li} at temperatures corresponding to flames studied were obtained using formula 4.13 in a computer program run on a RADIO SHACK TRS 80 micro computer using LEVEL II BASIC.

The heat of reaction ΔH^o was calculated from the heats of formation at 0 K of Li, H_2O, OH, and H, given in the JANAF thermochemical tables[53], and a value of 58.7 kJ for LiOH.

A value of 435 $kJ.mol^{-1}$ was used for the dissociation energy of Li - OH instead of the JANAF value of 430.1 ± 21 $kJ.mol^{-1}$. This value is still within the experimental uncertainty of the JANAF value and corresponds to a value of 58.7 kJ for the heat of formation of LiOH[75]. The reason for adopting a slightly high value is that it results in a smaller negative temperature coefficient for the reaction 5.1, so that the fact that we observe a negative temperature coefficient is not due to the fact that the value of D^o_{Li-OH} was too small. For the flames used in this work, values of [H] at 1.5ms from the reaction zone are plotted as a function of T^{-1} and presented in figure 16.

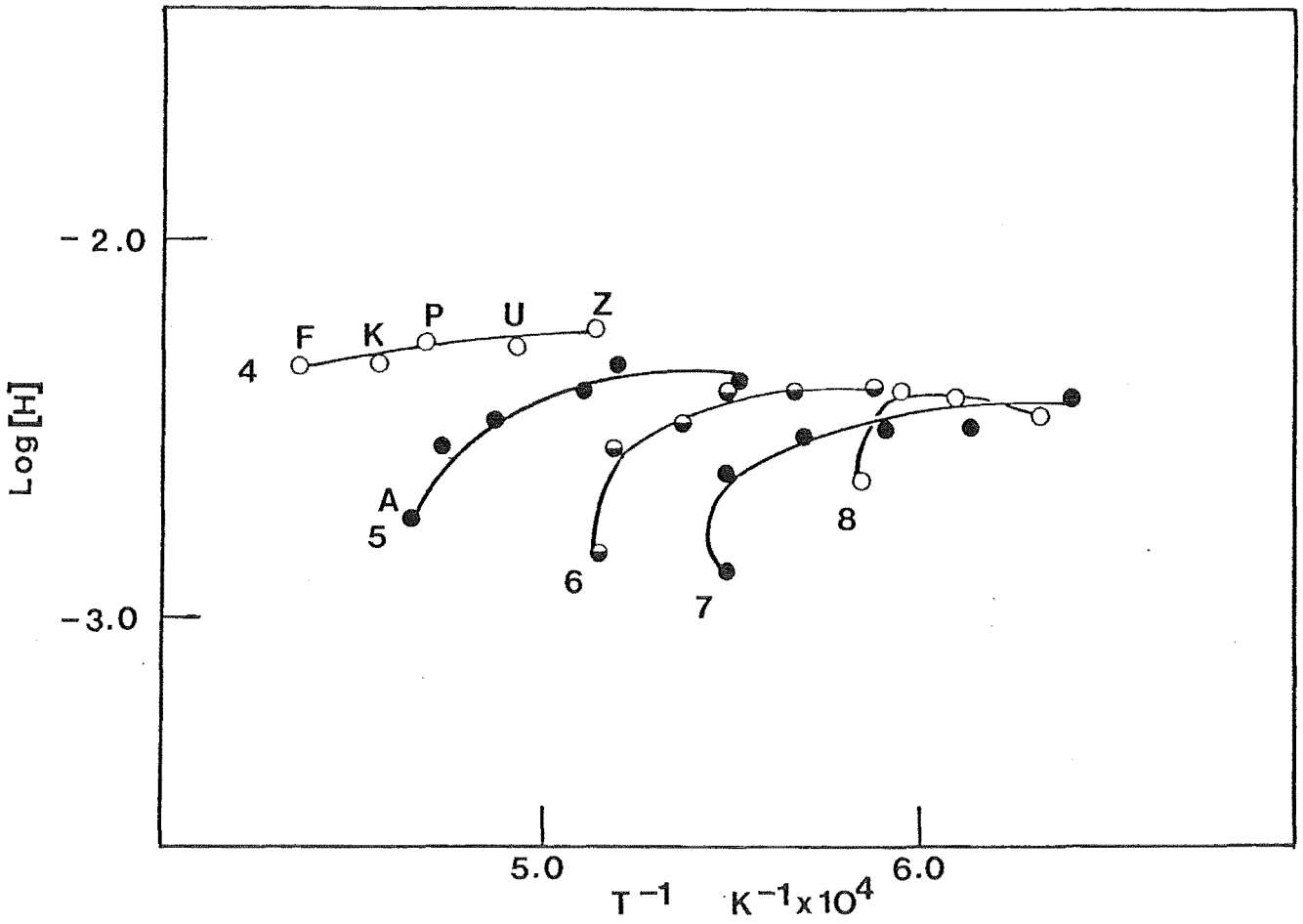

Fig. 16 Concentrations of atomic hydrogen measured at 1.5 ms from the reaction zone. The shading of points indicates families of flames (same N_2:O_2 ratio) identified by the number associated with each curve. Within each family, H_2:O_2 ranges from Z(4.5) to A(2.0) but family 4 ranges from Z(4.5) to F(2.5) and family 8 from U (4.0) to F(2.5).

IV. THE DEPENDENCE OF r AND r' on [H]

It was shown in figures 14 and 15 that the ratios of fluorescence r and r' were strongly peaked toward the reaction zone, which implied that the reaction 3.1

$$Pb(^3P_1{}^o) + M \rightleftharpoons Pb(^3P_0{}^o) + M \qquad 3.1$$

was most effective when M was a flame radical, namely H, OH or O.

It seemed that OH and H would be most likely to be important since the concentration of O atoms is generally two orders of magnitude below those of H and OH in hydrogen-rich flames[54].

Assuming that the rate of spin orbit relaxation, responsible for the shape of the curves in figure 14, is associated with either H or OH, rather than O, then to a first approximation (which is justified in section V.I), we may write

$$r = a\,H + b \qquad 4.15$$

or

$$r = a'I_{CuH} + b' \qquad 4.16$$

where a is associated with the rate constant of equation 3.1 for hydrogen atoms and b depends on the rate constant of equation 3.1 for M = N_2, H_2, H_2O. A similar expression may also be obtained for r'.

Direct plots of r versus I_{CuH} for a selection of flames are given in figure 17 and the correlation is seen to be excellent. According to equation 4.6, the concentration of oxygen atoms is directly proportional to the concentration of hydrogen atoms squared, and hence by

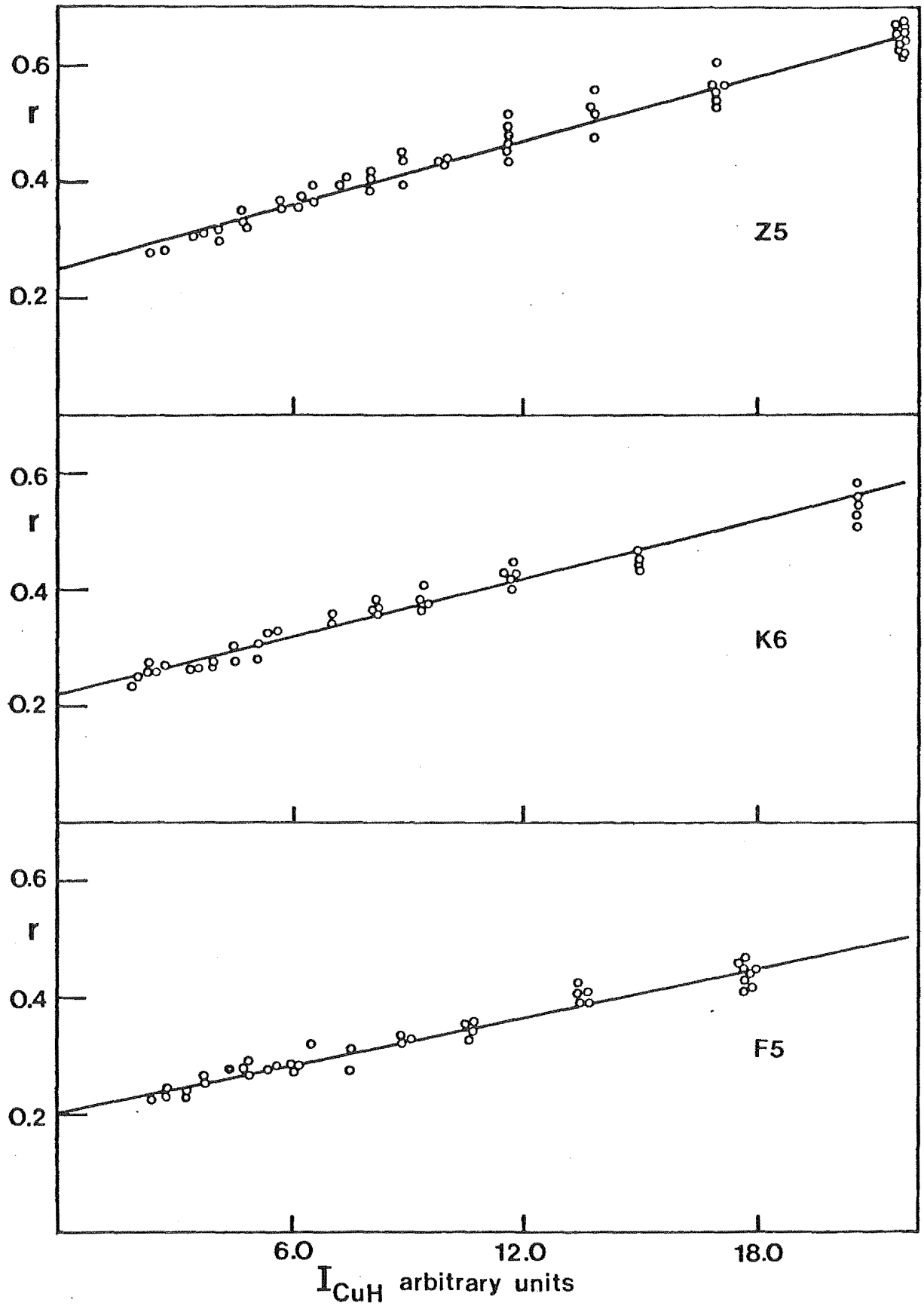

Fig. 17 Correlation of $r = \frac{I_{368.3}}{I_{364.0}}$ with relative hydrogen atom concentration given by I_{CuH}.

equation 4.7, is also proportional to $(I_{CuH})^2$. Plots of r versus $(I_{CuH})^2$ are given in figure 18, and it is obvious that there is no linear relationship between r and $(I_{CuH})^2$, so that oxygen atoms can be discounted as being significant in the process of spin orbit relaxation as given by equation 4.14.

For the flames studied in this work, it is found that the effect due to flame radicals is smaller when [H] is low, for example in the oxygen-rich flame A5(figure 14), and larger when [H] is large in the hydrogen-rich flame Z6(figure 14). Because of the family effect of equation 4.5, we expect [OH] to be greater in flame A5, than in flame Z6. Also, H atoms are typically an order of magnitude more abundant than OH radicals in hydrogen rich flames[7], so that H atoms rather than OH radicals are considered to be responsible for the observed effect. This assumption is proved to be correct when values of k_H, the rate of spin-orbit relaxation due to hydrogen atoms, are calculated. Any effect due to OH radicals would appear as a family effect (similar to the plots of [H] versus reciprocal temperature) due to the variation of [OH] in equation 4.5 with changing ratio $[H_2O]/[H_2]$ from flame to flame. That there is no obvious family effect can be seen from figure 19. It is possible however, that a small family effect does exist, but the magnitude of the scatter in figure 19 excludes any estimation of this.

It is concluded that the process of spin-orbit relaxation as given by equation 3.1 is best expressed as

$$Pb(^3P_1{}^o) + H \xrightarrow{k_H} Pb(^3P_0{}^o) + H \qquad 4.16$$

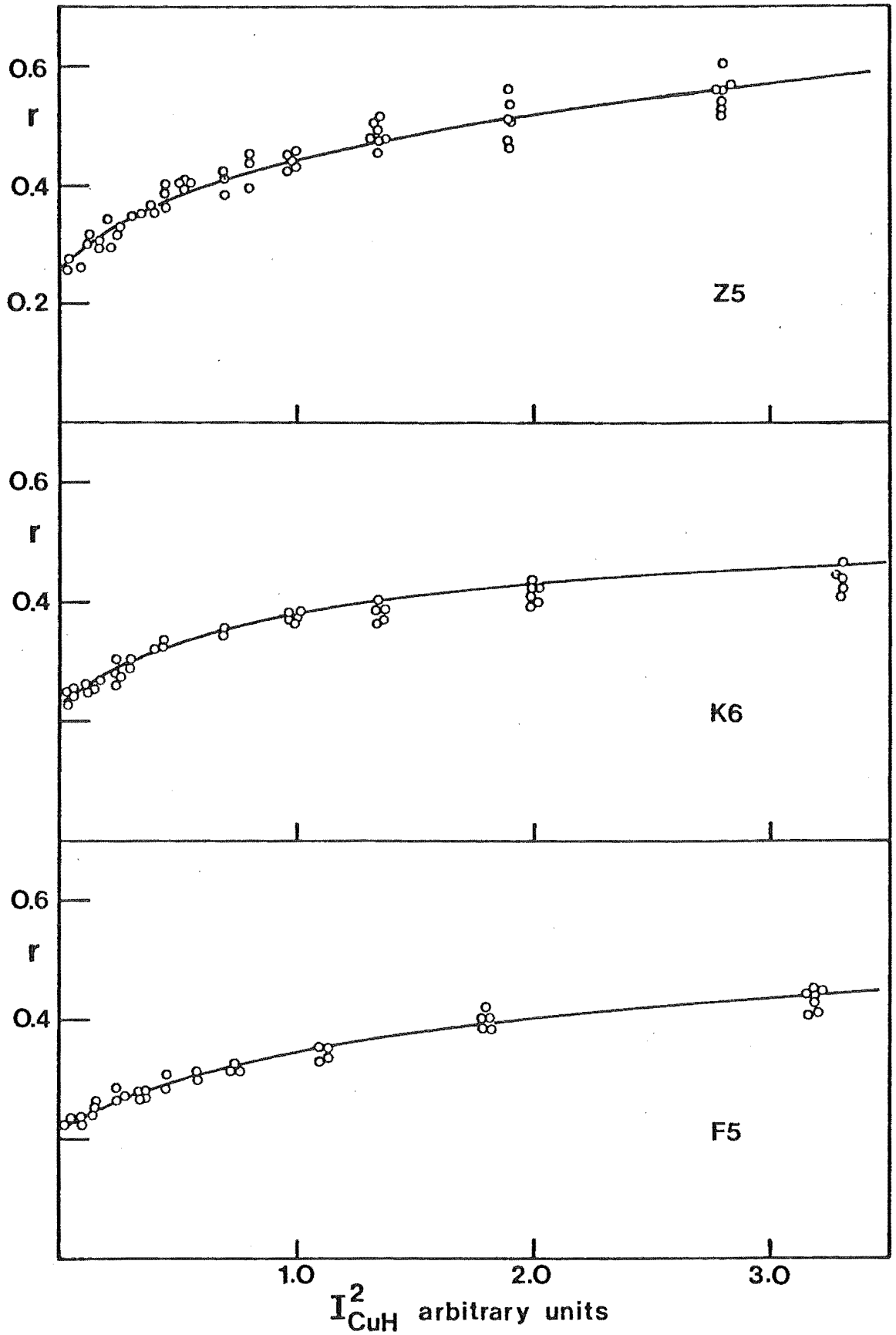

Fig. 18 Correlation of $r = \frac{I_{368.3}}{I_{364.0}}$ with relative oxygen atom concentration given by I^2_{CuH}.

The curves indicate a dependence of r on [H] rather than [O].

$$Pb(^3P_1{}^o) + M \overset{k_M}{\rightarrow} Pb(^3P_0{}^o) + M \qquad 4.17$$

as well as the respective reverse reactions. In equation 4.17, M is any of the bulk constituents of the flame, namely H_2, N_2 and H_2O.

CHAPTER V

I. EVALUATION OF k_H AND k_M

With reference to the fluorescence schemes given in figure 11, processes which are important in deriving expressions for k_H and k_M are listed 5.1 to 5.10,

$$Pb(^3P_1^o) + H \rightarrow Pb(^3P_0^o) + H \qquad 5.1$$

$$Pb(^3P_1^o) + M \rightarrow Pb(^3P_0^o) + M \qquad 5.2$$

$$Pb(^3P_1^o) + Q \rightarrow Pb + Q \qquad 5.3$$

$$Pb(^3P_0^o) + Q \rightarrow Pb + Q \qquad 5.4$$

$$Pb(^3P_0^o) + H \rightarrow Pb(^3P_1^o) + H \qquad 5.5$$

$$Pb(^3P_0^o) + M \rightarrow Pb(^3P_1^o) + M \qquad 5.6$$

$$Pb(^3P_1^o) \rightarrow Pb + h_{\nu 405.8} \qquad 5.7$$

$$Pb(^3P_1^o) \rightarrow Pb + h_{\nu 283.3} \qquad 5.8$$

$$Pb(^3P_1^o) \rightarrow Pb + h_{\nu 364.0} \qquad 5.9$$

$$Pb(^3P_0^o) \rightarrow Pb + h_{\nu 368.3} \qquad 5.10$$

where Q is any quencher species in the flame gases, such as H_2O, N_2, H_2, and is thus essentially the same as M. The Einstein transition probabilities for processes 5.7 to 5.10 are designated A_1 to A_4 respectively and are given in fig. 10. These values are the same as those used by Jenkins[41], and are referenced in fig. 10. The rate constants for reactions 5.1 and 5.2 are designated k_H and k_M respectively. If we denote the rate constants for reactions 5.5 and 5.6, as k'_H and k'_M, then we can relate k'_H to k_H by the principle of detailed balancing.

$$\frac{k'_H}{k_H} = \frac{[Pb(^3P_1{}^o)]}{[Pb(^3P_0{}^o)]} = \frac{g_1}{g_0} \exp(-hc\bar{\omega}/kT)$$

$$= 3 \exp(-hc\bar{\omega}/kT)$$

$$\frac{k'_H}{k_H} = K_{eq} \qquad 5.11$$

where $\bar{\omega}$ = 327.3 cm^{-1} (3.916 kJ mol^{-1}) is the energy separation of $Pb(^3P_1{}^o)$ and $Pb(^3P_0{}^o)$, g_1 and g_0 are the statistical weights of the states $^3P_1{}^o$ and $^3P_0{}^o$ respectively, and the other symbols have their usual meanings.

From the above, we can write:

$$k'_H = k_H K_{eq} \qquad 5.12$$

and similarly

$$k'_M = k_M K_{eq} \qquad 5.13$$

For the case of excitation at 405.8 nm, the steady state condition for $Pb(^3P_0{}^o)$ may be written as in 5.14, denoting $Pb(^3P_0{}^o)$ as Pb^o and $Pb(^3P_1{}^o)$ as Pb^1

$$\frac{d}{dt}[Pb^o] = 0 = (k_H[H] + k_M[M])[Pb^1] - [P_b{}^o]$$
$$(K_{eq}(k_H[H] + k_M[M]) + k_Q[Q] + A_4) \qquad 5.14$$

this rearranges to

$$\frac{[Pb^o]}{[Pb^1]} = \frac{k_H[H] + k_M[M]}{K_{eq}(k_H[H] + k_M[M]) + k_Q[Q] + A_4} \qquad 5.15$$

so that the ratio of fluorescence intensities, r, is given by 5.16

$$r = \frac{I_{368.3}}{I_{364.0}} = \frac{A_4[Pb^o]}{A_3[Pb^1]} \qquad 5.16$$

$$= \frac{A_4(k_M M + k_H H)}{A_3(K_{eq}(k_H H + k_M M) + k_Q Q + A_4)} \qquad 5.17$$

Similarly, for the case of excitation at 368.3 nm, under steady state conditions, we have that

$$\frac{d}{dt}[Pb^1] = 0$$

$$= K_{eq}(k_H[H] + k_M[M])[Pb^o]$$

$$-(k_M[M]+k_H[H]+k_Q[Q]+A_1+A_2+A_3)[Pb^1] \qquad 5.18$$

Writing $A_1 + A_2 + A_3 = A_5$, 5.18 rearranges to

$$\frac{[Pb^1]}{[Pb^o]} = \frac{K_{eq}(k_H[H] + k_M[M])}{k_M[M] + k_H[H] + k_Q[Q] + A_5} \qquad 5.19$$

so that the ratio of fluorescence intensities r' is given by 5.20 and 5.21

$$r' = \frac{A_1[Pb^1]}{A_4[Pb^o]} = \frac{I_{405.8}}{I_{368.3}} \qquad 5.20$$

$$= \frac{A_1K_{eq}(k_H[H] + k_M[M])}{A_4(k_M[M] + k_H[H] + k_Q[Q] + A_5)} \qquad 5.21$$

Equations 5.17 and 5.21 can be arranged to give

$$k_H[H] + k_M[M] = \frac{rA_3(A_4 + k_Q[Q])}{A_4 - rK_{eq}A_3} \qquad 5.22$$

and

$$k_H[H] + k_M[M] = \frac{r'A_4(A_5 + k_Q[Q])}{A_1K_{eq} - r'A_4} \qquad 5.23$$

The cross sections used to obtain k_Q were taken from Jenkins[41] and are listed in table 1 and refer to quenching of the $^3P_1{}^o$ state. These values are total quenching rates for $^3P_1{}^o$ and hence include a contribution from reaction 5.2, however, by subtracting the measured effect of reaction 5.2, a 'bare' quenching rate constant k_Q is obtained for each flame gas mixture. The same value of k_Q has been used for both reactions 5.3 and 5.4, that is, the quenching rates for

$^3P_1^o$ and $^3P_0^o$ have been assumed to be identical. This was necessary as there are no available values for quenching cross-sections for $^3P_0^o$.

In practice, since k_M (and hence k_Q) was not known to begin with, initial values of k_H and k_M were obtained by a

TABLE 1: Cross-sections for the quenching of Pb 7s $^3P_1^o$

Quencher	$\sigma^2 \times 10^{16}$ cm^2	Ref.
H_2	0.4 ± 0.1	Jenkins[41]
	0.016	Mandl and Chen[42]
H_2O	8 ± 2	Jenkins[41]
N_2	5.7 ± 0.5	Jenkins[41]
	5.7	Mandl and Chen[42]

least-squares fit of the right hand side of equations 5.22 or 5.23 to the decay of [H], obtained by the LiOH and CuH methods, as described in Chapter IV, using the cross-sections given by Jenkins[41]. The resulting value of k_M was subtracted from k_Q and the least squares routine repeated. In most cases only one iteration of this type was necessary because k_M is typically less than k_Q by about a factor of 10. That this is so can be seen from table 4 (page 66).

To a first approximation then, since k_M and k_H are small in comparison to k_Q, and with [H] typically of the order of 10^{-2} atm, the numerator of equation 5.17 can be set equal to $k_Q[Q]$ which is constant in any one flame. Hence equation 5.17 can be approximated to equation 5.24

$$r = \frac{A_4[Pb^1]}{A_3[Pb^o]} = \frac{A_4}{A_3} \times \frac{(k_H[H] + k_M[M])}{(k_Q[Q] + A_4)K_{eq}} \qquad 5.24$$

so that

$$r = \frac{A_4}{A_3} \times \frac{[Pb^1]}{[Pb^o]} = A(k_H[H] + k_M[M]) \qquad 5.25$$

where $A = \frac{A_4}{A_3} \cdot \frac{1}{(k_Q[Q] + A_4)K_{eq}}$

It can be seen that equation 4.15 is identical to 5.25, where

$$a = A.k_H$$

and $$b = A.k_M[M]$$

II. THE DEPENDENCE OF r AND r' ON LASER PULSE DURATION AND INTENSITY

The use of a short laser pulse (nominal range 2 to 10 ns) requires the consideration of possible effects due to saturation of absorption, and the possibility that insufficient time will be available during the pulse for the steady state condition, assumed in equations 5.18 and 5.14, to be established.

Saturation occurs when the photon density of the exciting radiation is such that the rate of absorption becomes greater than the normal processes of de-excitation of the excited state, namely spontaneous emission and quenching. Under these conditions and with increasing exciting photon density, the population of the excited state asymptotically approaches a limiting value dependent on the ratio of the degeneracies of the excited state and the lower state. When this occurs, stimulated emission becomes the

dominant process leading to depopulation of the excited state[55,56].

To assess the importance of the possibility of the laser pulse being too short to establish a steady state between Pb 7s $^3P_1^o$ and $^3P_0^o$, and the extent of saturation, the differential equations corresponding to the mechanism 5.1 to 5.10, and 5.26 to 5.29 were integrated numerically with typical values of rate constants (obtained from experimental values of r and r'), H atom concentration, temperature, laser power, pulse width, beam focal diameter, and laser bandwidth, assuming the laser pulse to have a Gaussian profile.

$$Pb(6s\ ^3P_2) + h\nu_{405.8} \rightarrow Pb^1 \qquad 5.26$$

$$Pb^1 + h\nu_{405.8} \rightarrow Pb(6s\ ^3P_2) + 2h\nu_{405.8} \qquad 5.27$$

$$Pb(6s\ ^3P_1) + h\nu_{368.3} \rightarrow Pb^o \qquad 5.28$$

$$Pb^o + h\nu_{368.3} \rightarrow Pb(6s\ ^3P_1) + 2h\nu_{368.3} \qquad 5.29$$

The Einstein B coefficients for the processes 5.26 to 5.29 were calculated from the related A coefficients for spontaneous emission, by the formulas:

$$A_{21} = B_{21} \frac{8\pi h\nu_0^3}{c^3}$$

$$B_{21}g_2 = B_{12}g_1$$

where g_1 and g_2 are the degeneracies of the lower and upper states 1 and 2 respectively[57].

The rate of excitation into an excited state is given by

$$\frac{dn_2}{dt} = n_1 B_{12} \rho(\nu) \qquad 5.30$$

where $\rho(\nu)$ is the uniform laser spectral energy density in $J.m^{-3}.s^2$ which was calculated by means of equation 5.31

$$\rho(\nu) = \frac{\Phi}{S.c\Delta\nu} \qquad 5.31$$

where Φ is the laser power in $J.s^{-1}$, $\Delta\nu$ is the laser bandwidth in s^{-1}, S is the beam cross-sectional focal area in m^2, and c is the velocity of light. For a typical run, the laser power was taken to be 200 W, after including losses due to the focussing lens and collimation, which corresponds to about 20% of the total laser output.

The effect of laser pulse length on the integrated ratios and peak intensity ratios can be seen by studying table 2. It is apparent that the integrated light intensity ratio and the calculated steady state ratio are in good agreement, even for light pulses which are much shorter than those likely to be encountered in practice.

The agreement between the peak intensity ratio and the steady state ratio is lost when the duration of the light pulse is decreased, but it should be noted that the detection system which was used in this work functioned as an integrator rather than a peak detector, so that the ratio of integrated intensities is the relevant quantity. Also, it is unlikely that pulse lengths of less than 2 ns were available from the laser.

For excitation at both 405.8 nm and 368.3 nm, time profiles of the concentrations of the two upper states, Pb 7s $^3P_1^o$ and $^3P_0^o$, and the lower states, Pb 6p $^3P_1$ and $^3P_0$ both denoted as Pb(6p ^3P), are given in appendix III. For excitation at 405.8 nm the condition of saturation is achieved when the ratio

Table 2 Numerical test of the steady-state assumption for the mechanism 5.1 to 5.10 and 5.26 to 5.29

[Assumed: T=2000K, $k_H = 1.5 \times 10^{-9}$, $k_M = 1.0 \times 10^{-11}$ (k's in $cm^3.molecule^{-1}.s^{-1}$), Gaussian laser pulse]

Excitation	Pulse length ns FWHM	H atm.	Ratio (peak)	Ratio (integral)	Ratio (steady state)
405.8 nm, Ratio = r	4	.001	.1776	.1821	.1821
		.003	.2199	.2252	.2252
		.01	.3564	.3639	.3639
	2	.001	.1677	.1821	.1821
		.003	.2080	.2252	.2252
		.01	.3387	.3639	.3639
	1	.001	.1487	.1821	.1821
		.003	.1848	.2252	.2252
		.01	.3034	.3639	.3639
	.5	.001	.1294	.1821	.1821
		.003	.1547	.2252	.2252
		.01	.2556	.3639	.3639
368.2 nm, Ratio = r'	4	.001	.05776	.05935	.05935
		.003	.07224	.07419	.07419
		.01	.1212	.1242	.1242
	2	.001	.05431	.05935	.05935
		.003	.06796	.07419	.07419
		.01	.1142	.1242	.1242
	1	.001	.04786	.05935	.05935
		.003	.05992	.07419	.07419
		.01	.1009	.1242	.1242
	.5	.001	.03966	.05935	.05935
		.003	.04966	.07419	.07419
		.01	.08366	.1242	.1242

$Pb(^3P_1{}^o)$: $Pb(6s\ ^3P_2)$

reaches 3:5. From the time profiles of appendix III (a) and (b), it can easily be seen that this condition is never met and the maximum achieved is about 1:5, corresponding to 30% saturation.

Similarly, for excitation at 368.3 nm, the ratio

$Pb(^3P_0{}^o)$: $Pb(6s\ ^3P_1)$

must reach 1:3 at saturation, and as shown in appendix III (c) and (d), this ratio does not exceed 1:9 for a 0.1 mm focal diameter. It is also important to note that the whole reaction zone (1 cm wide) is viewed by the horizontal slits of the spectrometer, so that the focal diameter ranges from 0.5 mm to about 0.1 mm in the viewing region.

The profile obtained using a high laser output of 1 kW and a 0.1 mm focal diameter is given in appendix III (e), and shows that while the concentrations approach 70% saturation at the peak laser intensity, the agreement between the integrated intensity ratio and the steady state ratio is maintained. The effect of laser saturation on the present work can be dismissed also by studying the derivations of the steady state equations 5.18 and 5.14. In both cases, a knowledge of the emission and absorption rates involving the directly populated state is not required in the steady state derivation. However, under saturated conditions the fluorescence at 368.3 nm, excited at 368.3 nm, will be modified by a contribution from stimulated emission, but this effect is expected to be minimal, since stimulated emission occurs only in the direction of propagation of the laser pulse and would not be detected above the fluorescence signal at right angles to

the beam[58].

III. RESULTS FOR k_H AND k_M

The program used to derive k_H and k_M from equations 5.22 and 5.23 consisted of a least-squares routine which fitted the right hand side of equation 5.22 or 5.23 to the decay of hydrogen atom concentration.

A list of values for k_H and k_M is given in table 3, which distinguishes those values obtained by excitation at 405.8 nm from those obtained by excitation at 368.3 nm. These results are also presented in figures 19 and 20, plotted as a function of temperature. The absolute deviations, expressed as percentage of k_H are also given in table 3.

The plot of k_M versus temperature given in figure 20 shows three important features. First, the process of spin-orbit relaxation, as given by equation 4.17, where M is one of the flame bulk constituents, namely H_2, N_2, or H_2O, is moderately fast since k_M is of the order of 10^{-11} cm^3. $molecule^{-1}$. s^{-1} in all flames. Second, the rate constant k_M shows a positive temperature coefficient (varying approximately as $T^{1.8}$). Third, the rate constant shows no marked "family effects". In other words, variation of flame gas composition at constant temperature does not have a marked effect on k_M. This implies, since $k_Q[Q]$ is the largest term in the denominator in equations 5.17 and 5.32, see table 4, that the relative quenching cross-sections for H_2, N_2 and H_2O are not seriously in error. It should be noted that the cross-sections quoted by Jenkins for N_2 and

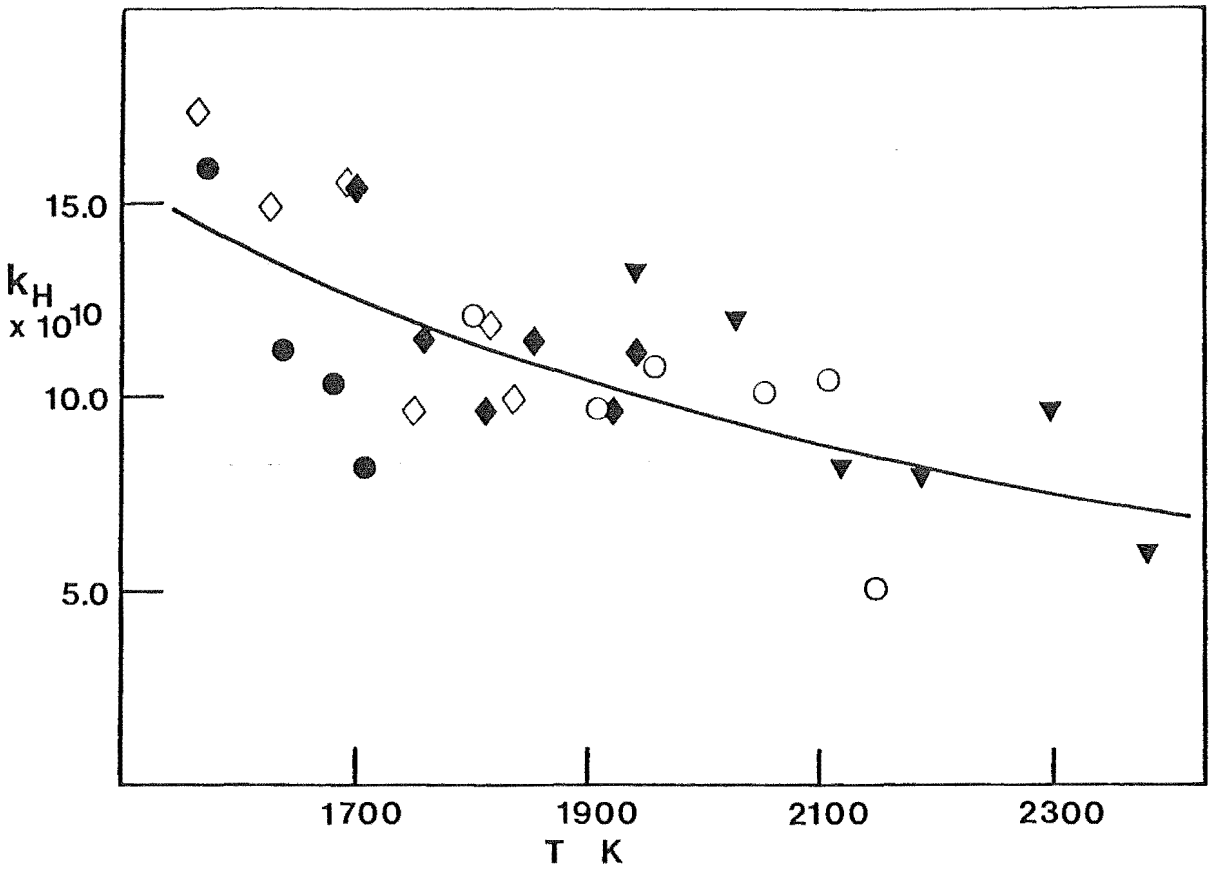

Fig. 19 The variation of k_H with temperature T. The solid line corresponds to a $T^{-1.7}$ dependence. Families of flames are distinguished by different symbols. k_H is in $cm^3.molecule^{-1}.s^{-1}$.

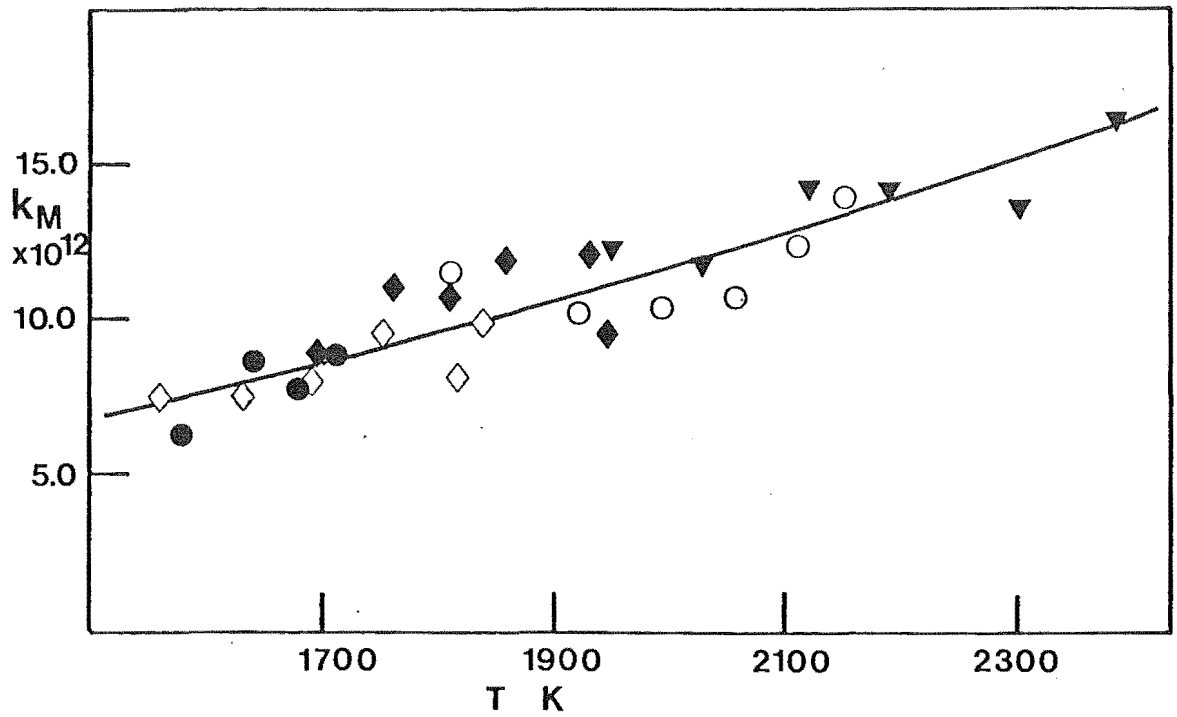

Fig. 20 The variation of k_M with temperature T. The solid line corresponds to a $T^{1.8}$ dependence. The symbols for various families are the same as in Fig. 19. k_H is in $cm^3.molecule^{-1}.s^{-1}$.

Table 3(a). Excitation at 405.8 nm

Flame	Temperature K	$k_H x10^{10}$ $cm^3.mol^{-1}.s^{-1}$	$k_M x10^{12}$ $cm^3.mol^{-1}.s^{-1}$	% deviation
U8	1575	15.93	6.21	12.2
P8	1640	11.03	8.75	11.3
K8	1680	10.23	8.04	11.4
F8	1710	8.01	8.78	12.3
Z7	1560	17.4	7.56	
U7	1630	15.04	7.54	8.5
P7	1689	15.5	8.05	8.5
K7	1750	9.63	9.63	7.8
F7	1835	9.98	9.77	7.9
A7	1815	11.8	8.17	9.5
Z6	1696	15.4	8.96	5.6
U6	1760	11.3	11.12	8.1
P6	1810	9.64	10.9	11.8
K6	1856	11.4	11.9	5.9
F6	1927	9.6	1.21	7.9
A6	1945	11.1	9.5	10.2
Z5	1807	12.0	11.4	5.9
U5	1920	9.4	10.3	6.2
P5	1958	10.9	10.5	8.3
K5	2055	10.1	10.8	8.2
F5	2110	10.3	12.4	6.2
A5	2148	4.36	13.9	7.1
Z4	1945	13.5	12.2	7.5
U4	2027	12.1	11.7	11.2
P4	2120	8.2	14.3	6.2
K4	2188	7.9	14.1	10.4
F4	2300	9.7	13.6	9.3
A4	2385	5.9	16.5	6.7

Table 3(b). Excitation at 368.3 nm

Flame	Temperature K	$k_H x10^{10}$ $cm^3.mol^{-1}.s^{-1}$	$k_M x10^{12}$ $cm^3.mol^{-1}.s^{-1}$	% deviation
U7	1630	19.0	4.46	7.6
Z6	1696	23.7	4.72	12.2
K6	1856	12.6	6.94	7.9
Z5	1807	23.3	5.08	9.1
P5	1958	17.2	5.87	7.4
F5	2110	11.4	10.5	11.3
F4	2300	14.0	10.3	9.0

H_2O are in agreement with the results of Mandl and Chen[42], but Jenkins'[41] value of $\pi.\sigma_{H_2}^2 = 1.3 \times 10^{-16}$ cm^3 is considerably different from that of Mandl and Chen, who obtain $\pi.\sigma_{H_2}^2 = 0.05 \times 10^{-16}$ cm^3. However, the contribution of $k_{H_2}[H_2]$ to $k_Q[Q]$ is quite small ($k_{H_2} \simeq 5 \times 10^{-11}$ cm^3. molecule^{-1}. s^{-1}, and $k_Q \simeq 3 \times 10^{-10}$ cm^3. molecule^{-1}. s^{-1}) since $[H_2]$ is typically of the order of 10^{-2} atm, as can easily be seen by studying table 4.

TABLE 4

FLAME	[H] atm	$k_Q[Q]$ s^{-1}	$k_H[H]$ s^{-1}	$k_M[M]$ s^{-1}
	1.4×10^{-2}	9.59×10^{8}	6.46×10^{7}	4.56×10^{7}
K6	9.49×10^{-3}		4.38×10^{7}	
T = 1856 K	2.56×10^{-3}		1.18×10^{7}	
F5	1.34×10^{-2}	9.56×10^{8}	4.72×10^{7}	4.27×10^{7}
T = 2110 K	5.95×10^{-3}		2.09×10^{7}	
	2.0×10^{-3}		7.05×10^{6}	
Z5	2.19×10^{-2}	8.62×10^{8}	1.07×10^{8}	4.63×10^{7}
T = 1807 K	6.55×10^{-3}		3.19×10^{7}	
	2.54×10^{-3}		1.24×10^{7}	

The values of r and r' corresponding to different heights in the flame gas, and all relevant flame parameters were stored on magnetic disc for easy access. All data points for each run were included in the initial determinations of k_H and k_M but, in some cases, those points which deviated from the least-squares line by more than twice the standard deviation were removed, and the least-squares routine repeated. These points were considered to be 'wild' points

(in the worst cases, six points out of sixty were removed, and only seven flames were treated this way; typically, about two or three points were removed), and could easily have arisen from atomiser or laser power fluctuation during a measurement, or slight off-line tuning of the monochromator.

As can be seen from table 3, the values of k_H and k_M obtained by excitation at both 368.3 nm and 405.8 nm are not in good agreement, although the results are broadly compatible. The uncertainty associated with the values of k_H and k_M can be estimated from the uncertainty in hydrogen atom concentrations, quenching rates and the absolute deviations associated with the least-squares fit of r to hydrogen atom concentration. Taking an uncertainty in $\Delta H^{O}(0)$ for equation 4.10 to be 5 $kJ.mol^{-1}$, the resulting uncertainty in [H] is calculated to be about 30%. Also, a 0.2 mm error in determining the flame front will result in an approximate uncertainty of 10% in [H] in the region 2 mm to 5 mm above the burner face, and since this is the region which defines the slope of graphs such as in fig. 17, it is justified to place an uncertainty of 40% on [H]. The uncertainty in quenching rate constants can be taken as that corresponding to the quenching by H_2O and N_2, and for most flames, this amounts to about 10%. In the majority of cases, the mean deviation of k_H, and hence k_M, obtained from a least squares fit of r to [H], is about 10%, so that the total uncertainty associated with a value of k_H or k_M can be estimated, in a first approximation*, as 60%.

* This estimation is in error in that random errors associated with k_H and k_M have been compounded with systematic errors (50%).

CHAPTER VI

PREDICTIONS OF RATE CONSTANTS BY MODEL CALCULATIONS

I. INTRODUCTION

The calculation of rate constants for collisionally induced atomic and molecular transitions usually involves calculating the probabilities of non-adiabatic transitions, which arise from crossing of potential curves corresponding to wave functions of the transient molecules formed during the collision.

The theory of curve crossing was developed independently by Landau[59], Zener[60], and Stuckelberg[61], and has been applied successfully, with various modifications, to a number of atomic and molecular systems[62]. However, the basic Landau-Zener theory has a number of limitations, due to assumptions made in its derivation, which restrict its region of applicability. These have resulted in a number of modifications by various workers in attempts to extend its range of validity[63].

In spite of its defects, the Landau-Zener theory is very useful in providing at least a qualitative description of how curve crossing influences collisions between atomic systems, and the theory is quantitative in many cases[62]. The essential features of the theory and its modifications are outlined in the following sections.

The results of its application to the Pb* + H and Pb* + H_2O systems, to predict rate constants, are presented and compared with the experimental values.

II. THE THEORY OF CURVE CROSSING

Curve crossing in a system of two colliding atoms in an inelastic encounter is normally described in terms of a tendency for the two electronic states of the unperturbed diabatic wave functions, ϕ_1 and ϕ_2, to mix as they become degenerate at a crossing point, given by V_x and R_x in fig. 21. When the relative velocity of the two colliding atoms is high, the mixing is weak, and the system will tend to remain in one of the diabatic states, so that the translational motion of the colliding partners is governed by V_1 or V_2. At low velocities however, where the mixing term is dominant, the system will remain in one of its adiabatic states ψ_1 or ψ_2, and the translational motion is governed by V_1' or V_2'.

The potential energy curves of the adiabatic wave functions ψ_1 and ψ_2 exhibit an avoided crossing with a minimum energy separation $2\varepsilon_{12}$, where ε_{12} is the matrix element of the perturbation which mixes the original diabatic wave functions ϕ_1 and ϕ_2.

The Landau-Zener theory predicts that the probability of a transition from one diabatic curve to another is given by

$$P_{12} = \exp(-2\pi\varepsilon_{12}^2/hv|F_1 - F_2|) \qquad 6.1$$

where v is the relative velocity of the colliding partners along their line of centres (radial velocity), and F_1 and F_2 are the slopes of the potential curves in the region of crossing. This is equivalent to the probability that the system will remain in one of the adiabatic states. Consequently, since the system must be represented by either a diabatic or an adiabatic state, the probability that it will

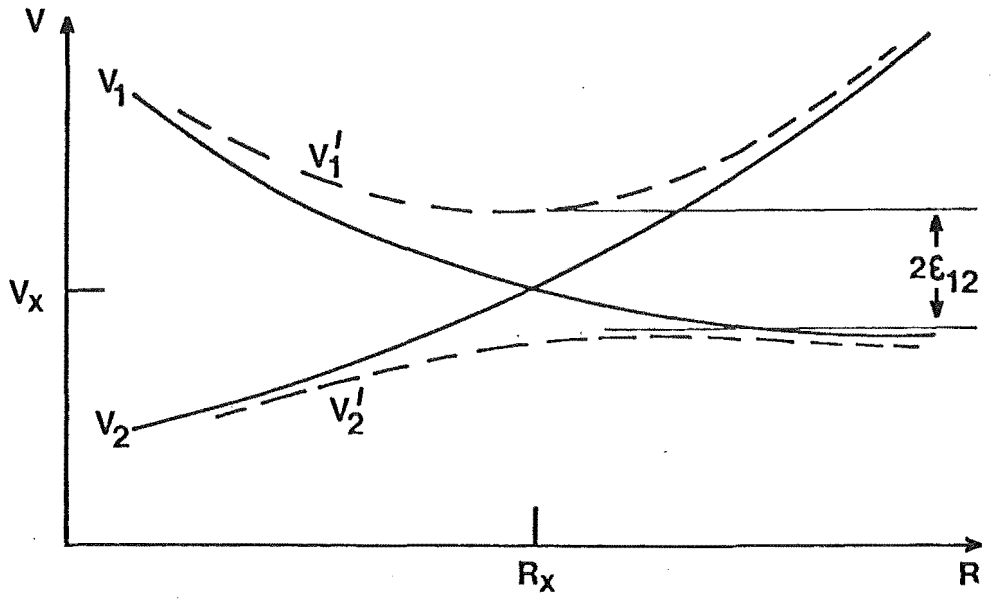

Fig 21. Potential curve for a two-state curve crossing. V_1 and V_2 are the potentials of the unperturbed diabatic wave functions ϕ_1 and ϕ_2 respectively. V_1' and V_2' are the potential curves of the adiabatic wave functions ψ_1 and ψ_2 which result from a mixing of the diabatic wave functions ϕ_1 and ϕ_2.

remain in one of the diabatic states will be $1 - P_{12}$, which is equivalent to a transition from one adiabatic state to the other.

In an atomic collision, the system must pass through the crossing region twice: once when the atoms approach each other, and again when they recede, so that the total probability of a transition is given by

$$P = 2P_{12}(1 - P_{12}) \qquad 6.2$$

This is the basic Landau-Zener formula. The approximations made in its derivation can be summarised as follows:

$$\varepsilon_{12} = \text{a constant} \qquad 6.3$$

$$v = (2E/\mu)^{\frac{1}{2}} = \text{a constant} \qquad 6.4$$

$$F_i = \frac{dV_i}{dx} = \text{a constant} \qquad 6.5$$

where μ is the reduced mass of the colliding atoms with energy E. In equation 6.5, the assumption is that the slopes given by F_1 and F_2 are constant in the region of the crossing, i.e. the potential curves V_i are linear. A modified form of equation 6.2 has been given by Stuckelberg[61], who obtained

$$P = 4P_{12}(1 - P_{12})\sin^2\tau \qquad 6.6$$

for the total crossing probability, where τ is given by

$$\tau = \frac{\pi}{4} + \int_{r_1}^{R_x} \left(\frac{2\mu}{h^2}[E-V_1]\right)^{\frac{1}{2}} dr - \int_{r_2}^{R_x} \left(\frac{2\mu}{h^2}[E-V_2]\right)^{\frac{1}{2}} dr \qquad 6.7$$

where r_1 and r_2 are the classical turning points for the motion of energy E on curves V_1 and V_2 respectively, and R_x is the crossing radius as shown in fig. 21. The $2 \sin^2\tau$ factor arises from interference between the wave functions for incoming and outgoing particles. Equation 6.6 is known as the Landau-Zener-Stuckelberg formula, and embodies the same assumptions, given in equations 6.3 to 6.5, as equation 6.2. When τ is large, due to integration over a large number of trajectories, corresponding to a range of neighbouring potential curves (such is the case when a number of rotational levels are included in V_1 and V_2) then equation 6.6 reduces to equation 6.2.

With reference to fig. 21, it can be seen that the assumptions given by equations 6.3 and 6.4 are valid provided that the region in which they apply is sufficiently small. The effective width of the crossing region is dependent on the magnitude of the velocity $\dot{v}$. At low velocities, it is defined as the region Δr in which the diabatic curves are significantly different from the adiabatic curves. For this case, the "static width" is given by

$$\Delta r = 4\ \varepsilon_{12}/|F_1 - F_2| \qquad 6.8$$

At high velocities, the width of the crossing region is governed by the size of the region over which the phase

difference between the wave functions ϕ_1 and ϕ_2 is small. For this case, the "dynamic width" is given by

$$\Delta r = 2(2hv/|F_1 - F_2|)^{\frac{1}{2}} \qquad 6.9$$

Thus, as the velocity becomes larger, and the width of the crossing region becomes greater, it is obvious that the equations 6.3 and 6.4 will not hold over the entire crossing region. However, it can be shown[64] that the Landau-Zener formula is valid provided that

$$\varepsilon = (E\Delta F/2F\varepsilon_{12}) >> 1 \qquad 6.10$$

and

$$E/\varepsilon_o >> 2 \qquad 6.11$$

where

$$\Delta F = |F_1 - F_2|,\ F = (|F_1.F_2|)^{\frac{1}{2}} \text{ and}$$

$$\varepsilon_o = (h^2F^4/2\mu\Delta F^2)^{\frac{1}{3}}$$

For the case where the transition region includes the turning point for classical motion on the 'mean potential' with slope F, the assumption of constant velocity is again invalid; however, Nikitin[65] has obtained the result given in equation 6.13 for the probability near the turning point.

$$P = \pi^2\ B^{4/3}\{A_i(-E/\varepsilon_o)\}^2 \qquad 6.13$$

where $A_i(y)$ is the Airy function as tabulated by Abramovitz and Stegun[66], and

$$B = (2\varepsilon_{12}F/\varepsilon_o\Delta F)^{1\frac{1}{2}} << 1 \qquad 6.14$$

At energies E which are well above V_x, equation 6.13 reduces to

$$P = 4\pi\varepsilon_{12}^2/hv\Delta F \qquad 6.15$$

which is identical to the Landau-Zener formula in equation 6.2, when P_{12} is small.

When $E << V_x$, for example when the potential curves include a large rotational term corresponding to a large impact parameter, as in fig. 22(b), the system must reach R_x by quantum-mechanical tunnelling. For these cases, Nikitin[67] has obtained the result

$$P = 2\pi\varepsilon_{12}^2/(h|v|\Delta F).\exp(-\tfrac{4}{3}|\tfrac{E}{\varepsilon_o}|^{1\frac{1}{2}}) \qquad 6.16$$

The formulae above apply to cases where the curve crossing is fully allowed[68]. For a fully allowed transition,

$$\Delta\Omega = 0 \qquad 6.17$$

where Ω is the total angular momentum of the transient diatomic molecule. Where

$$\Delta\Omega = \pm 1 \qquad 6.18$$

the crossing probability is small, and is given by

$$P_{12} = 2\pi\omega_x^2.J(x)_{12}^2/\Delta FhV \qquad 6.19$$

Here ω_x is the angular velocity of rotation of the molecular axis in a plane perpendicular to the angular momentum vector of the colliding atoms, and $J(x)_{12}$ is the matrix element of the angular momentum operator J(x) between the diabatic wave functions. Transitions of this sort occur where the coupling arises from a failure of the electrons to keep up with the rotational motion of the nuclei[63].

III AVERAGING OVER IMPACT PARAMETER AND VELOCITY DISTRIBUTION

For a given impact parameter b and collision energy $E = \frac{1}{2}\mu v_o^2$, the radial component of the relative velocity is given by

$$v^2 = 2(E - V_{eff})/\mu \qquad 6.20$$

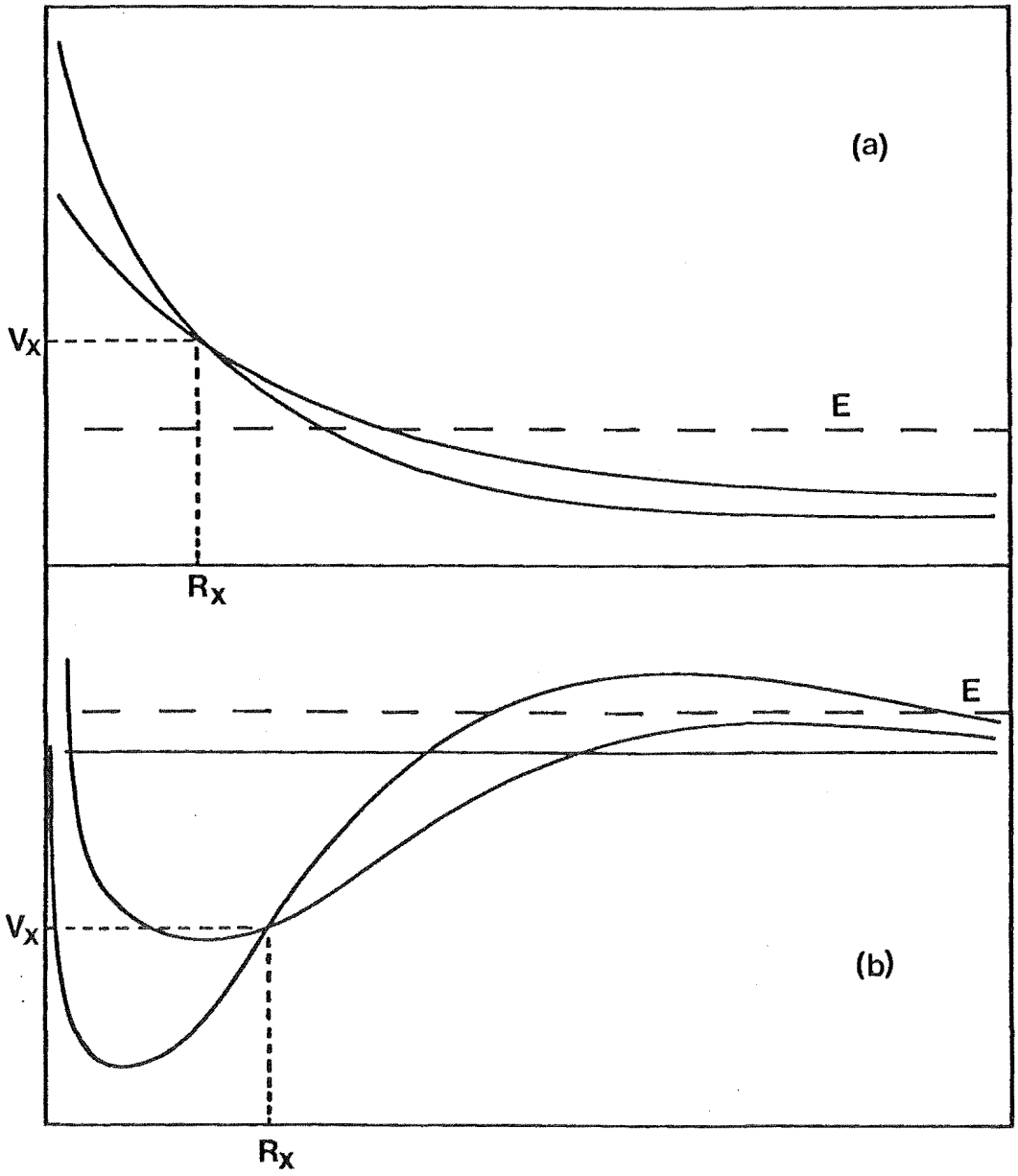

Fig. 22 Tunnelling to the crossing point given by R_x, V_x: (a) large rotational energy component, $E < V_x$ with tunnelling from below: (b) moderate rotational component, $E > V_x$ with tunnelling from above.

where V_{eff} includes a rotational energy component, and is given by

$$V_{eff}(r) = V(r) + \mu v_o^2 b^2/2r^2 \qquad 6.21$$

and V(r) is the energy given by one of the original diabatic curves. This has the effect of moving the crossing potential V_x to higher values as the rotational energy increases, giving rise to a centrifugal barrier at moderate energies, and a repulsive potential at high rotational energies, and introduces the possibility of tunnelling to R_x. This point is illustrated in fig. 22.

For the curve in fig. 22(a), at energies below V_x it is possible to reach R_x by quantum-mechanical tunnelling. Alternatively, if a rotational barrier exists when the energy is greater than V_x, then the system may reach R_x by tunnelling through the barrier. This point is illustrated in fig. 22(b).

For a given probability $P(b,v_o)$ which takes tunnelling and turning points into account, the velocity dependent probability is obtained by integrating over all the impact parameters which make a significant contribution to the probability, so that we have

$$P(v_o) = \frac{2\int_o^{bmax} P(b,v_o)\,bdb}{bmax^2} \qquad 6.22$$

where b_{max} is the largest value of b which has a significant contribution. The collision cross-section is therefore given by

$$\sigma(v_o) = \pi b_{max}^2(v_o) \qquad 6.23$$

Crossing is possible, without tunnelling, over the range where

$$0 < b < R_x[1 - (V_x/E)]^{\frac{1}{2}} \qquad 6.24$$

so that b_{max} is given by

$$b_{max} = R_x[1 - (V_x/E)]^{\frac{1}{2}} \qquad 6.25$$

if tunnelling is negligible. This has the effect of producing a $T^{-\frac{1}{2}}$ dependence of b_{max} and a T^{-1} dependence of the cross section when $-V_x >> E$.

If the effects of tunnelling and turning points are neglected, then the product of collision cross-section and crossing probability at a given velocity v_o is obtained as[69]

$$\sigma(v_o)P(v_o) = \frac{4\pi^2\varepsilon_{12}^2 R_x^2 (2\mu[E-V_x])^{\frac{1}{2}}}{h\Delta FE} \qquad 6.26$$

when $\Delta\Omega = 0$. When $\Delta\Omega = \pm 1$, the result is given as

$$\sigma(v_o)P(v_o) = \frac{16\pi^2 J(x)_{12}^2 \, 2^{\frac{1}{2}}(E-V_x)^{1\frac{1}{2}}}{3h\mu^{\frac{1}{2}}\Delta F.E} \qquad 6.27$$

The average cross-section and probabilities are obtained by integrating $P(v_o)$ and $\sigma(v_o)$ over the Maxwell distribution of speeds at a given temperature, to obtain $P(T)$ and $\sigma(T)$. The rate constant is then calculated as

$$k(T) = (\gamma)^{-1}\sigma(T)P(T)\left(\frac{8RT}{\pi\mu}\right)^{\frac{1}{2}} \qquad 6.28$$

where $(\gamma)^{-1}$ is a statistical weight factor, equal to the fraction of collisions which populate the state from which crossing is allowed.

IV COLLISIONS OF MOLECULES

The theory of non-adiabatic collisions involving molecules has been reviewed by Tully[70] and is discussed in books by Child[71] and Nikitin[72]. Because of the number of

degrees of freedom associated with molecules, it is necessary to consider the crossings of multidimensional potential energy surfaces, rather than two dimensional potential curves for atomic collisions, and a single transition may involve a number of such crossings. In many cases it appears that the transition probability can be described by the Landau-Zener formula, treating the molecule as a single atom. In calculating rate constants for the bulk constituents, the system Pb* + H_2O was used, and P_{12} was calculated using equation 6.19.

V COLLISIONS OF Pb* AND H

A correlation diagram for $Pb(^3P^o)$ + $H(^2S_{\frac{1}{2}})$ is given in fig. 23 where it has been assumed that the $^2\Sigma$ state is less stable than the $^2\Pi$ state[73]. It can be seen that there are two possibilities for crossings. In the first case, the crossing has $\Delta\Omega = 0$, and statistical weight $\frac{1}{3}$, in the second case, $\Delta\Omega = -1$, with statistical weight $\frac{2}{3}$. The probability of crossing for $\Delta\Omega = -1$ is expected to be small compared with that for $\Delta\Omega = 0$.

VI CALCULATIONS

Calculations were performed for the Pb* + H and Pb* + H_2O systems using Morse potentials, Lennard-Jones 6 - 12 potentials, and in some cases, Morse potentials which had been modified by hand so that the effect of the shape of the curve in the vicinity of the crossing could be investigated.

Potentials were calculated at forty values of internuclear distance ranging from slightly less than the smaller r_e value to about 20 nm. With all potentials used, the

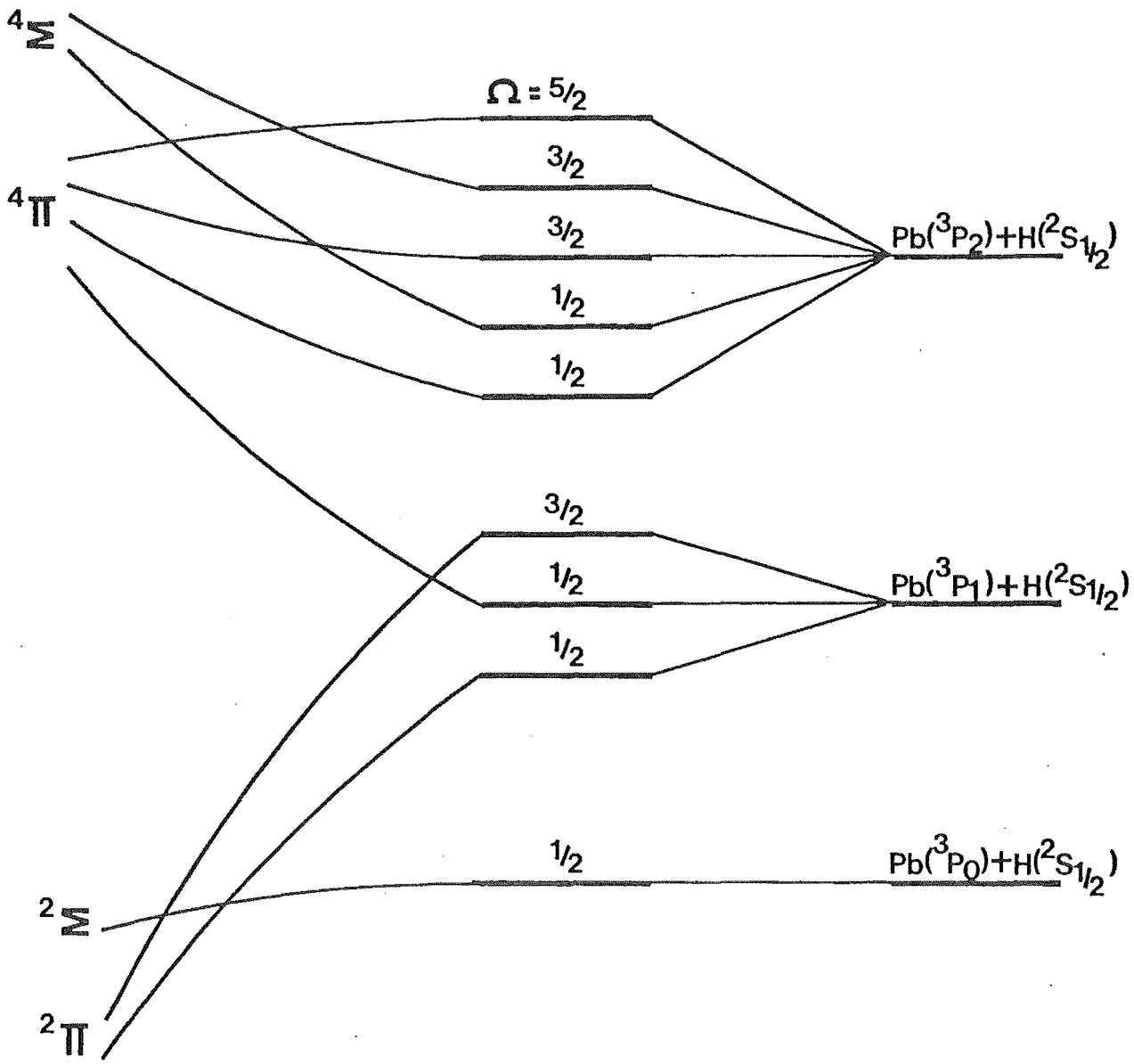

Hund's case (a) Small internuclear distance

Hund's case (c) Large internuclear distance

separated atoms

Fig. 23 Correlation diagram for PbH.

dissociation limits were adjusted to give a separation of 3.196 kJ mol^{-1}, corresponding to the separation of the $^3P_1^o$ and $^3P_0^o$ states of lead.

For each potential curve, a set of thirty different curves were constructed by adding different amounts of rotational energy, which covered the range of velocities and impact parameters which would be encountered in the calculation over the temperature range of interest.

The values of R_x and ΔF were calculated using the original potential curves with no rotational energy added, and the values of V_x, F_1, F_2 and F were calculated once the rotational energy had been added.

For each ε_{12} value used (chosen between 1 kJ mol^{-1} and 10^{-3} kJ mol^{-1}), a set of thirty equally spaced gas velocities was chosen to cover the Maxwell distribution up to three times the mean speed $\bar{v}$, and the value $3\bar{v}$ was used as the upper limit of integration when integrating $P(v_o)$ and $\sigma(v_o)$. The crossing width Δr was calculated as the larger of the two values given by equations 6.8 and 6.9, and the corresponding potential energy range in the crossing region was calculated as

$$\Delta E = F.\Delta r \qquad 6.29$$

For each value of energy E, the corresponding b_{max} was calculated by equation 6.25 and P(b,V) was calculated for a succession of b values which were incremented in steps of $b_{max}/30$. The actual potential energies corresponding to these values of the parameters V and b were obtained by interpolation between the curves of V_{eff} previously calculated.

If the energy was such that tunnelling through a

rotational barrier was required in order to reach R_x, the barrier transmission probability was calculated using the WKB formula[74]. For energies which were above V_x by more than $\frac{1}{2}\Delta E$, P was calculated by equation 6.2 with v equal to $[2(E - V_x)/\mu]^{\frac{1}{2}}$. For energies which fell within the range of the crossing region ΔE, so that the effects of the turning point became significant, P was calculated by equation 6.13 when the absolute value of the argument of the Airy function was less than 2. When the value of the argument was greater than 2, and for $E > V_x$, equation 6.15 was used, and for $E < V_x$, equation 6.16 was used. This procedure was necessary in order to avoid the oscillations of the Airy function, which are not taken into account properly in calculations employing finite velocity increments.

Once the values of P(v) had been obtained for a particular value of ε_{12}, $\sigma(T)$ was calculated for a number of temperatures using equation 6.23, P(T) was calculated by integrating $P(v_o)$ over the Maxwell distribution of speeds and the rate constant was calculated at each temperature using equation 6.28, with $\gamma = 1$ for the Pb* + H_2O system and $\gamma = \frac{1}{3}$ for the Pb* + H system.

The program used in the calculations was developed mainly by Professor L.F. Phillips of this department, using MICROSOFT fortran, and run on a Radio Shack TRS-80 microcomputer.

VII RESULTS OF CALCULATIONS

A selection of results for the Pb* + H system are presented in table 5. It can be seen that the observed magnitude of the rate constant and the sign of the tempera-

ture coefficient of k(T) can be reproduced, by suitable choice of ε_{12} and R_x, provided that $-V_x$ is made sufficiently large to produce a definite negative temperature coefficient. This is a direct result of the negative temperature dependence of b_{max}. With Lennard-Jones potentials, the energy dependence of b_{max} is usually swamped by a large positive temperature dependence of P(T). The results for the modified Morse curves are given in table 6, and the corresponding potential curves are shown in fig. 24. The original Morse curves were modified to give an indication of the effect of changing the shapes of the trajectories in the crossing region for a given well depth and vibrational frequency away from the crossing region. The effect is seen to be small, and the results of the temperature dependence are not much different from those obtained with the original potentials.

The results of calculations for the Pb* + H_2O system are given in Table 7, using Lennard-Jones 6 - 12 potentials. If the potential curves are made sufficiently deep for crossing to occur in the region where F_1 and F_2 are positive, the calculations yield a negative temperature coefficient for k_M, but if the crossing occurs at $R_x < r_e$ for both curves, so that F_1 and F_2 are both negative, the resulting k_M has a positive temperature coefficient.

Table 8 indicates the relative importance of the assumptions made in the Landau-Zener formula when the subroutines which include corrections for tunnelling and turning point are omitted. While the effect of the tunnelling is quite small, the effect of the turning point is quite significant. When the effect of the turning point was ignored, the simple Landau-Zener formula was used with

the assumption of constant velocity.

VIII COMPARISON OF THEORY AND EXPERIMENT

For the Pb* + H system a logarithmic plot of the temperature dependence of the experimental values of k_H is given in figure 24(a). The data were subjected to a least-squares routine to obtain the magnitude of the temperature exponent. The results of the power fit gave a temperature coefficient corresponding to a power of T of -1.7 ± 0.7 at the 95% confidence level. The 95% confidence band is taken as lying between the limits of twice the standard deviation from the mean.

For the Pb* + H_2O system, a similar plot is given in fig. 24(b). The power fit of k_M to temperature T, yielded a temperature coefficient corresponding to a power of T of 1.8 ± 0.3 at the 95% confidence level.

Although the magnitudes of the temperature coefficients are not identical with those predicted by the Landau-Zener theory, the differences are possibly just within the limits of error. The magnitudes of the absolute values of k_H and k_M can be reproduced, and the signs of the temperature coefficients are predicted correctly. The theoretically predicted powers of T are about -0.5 for the Pb* + H system, and +0.45 for the Pb* + H_2O system. Clearly further work is needed to determine experimental potential curves for the excited states of PbH.

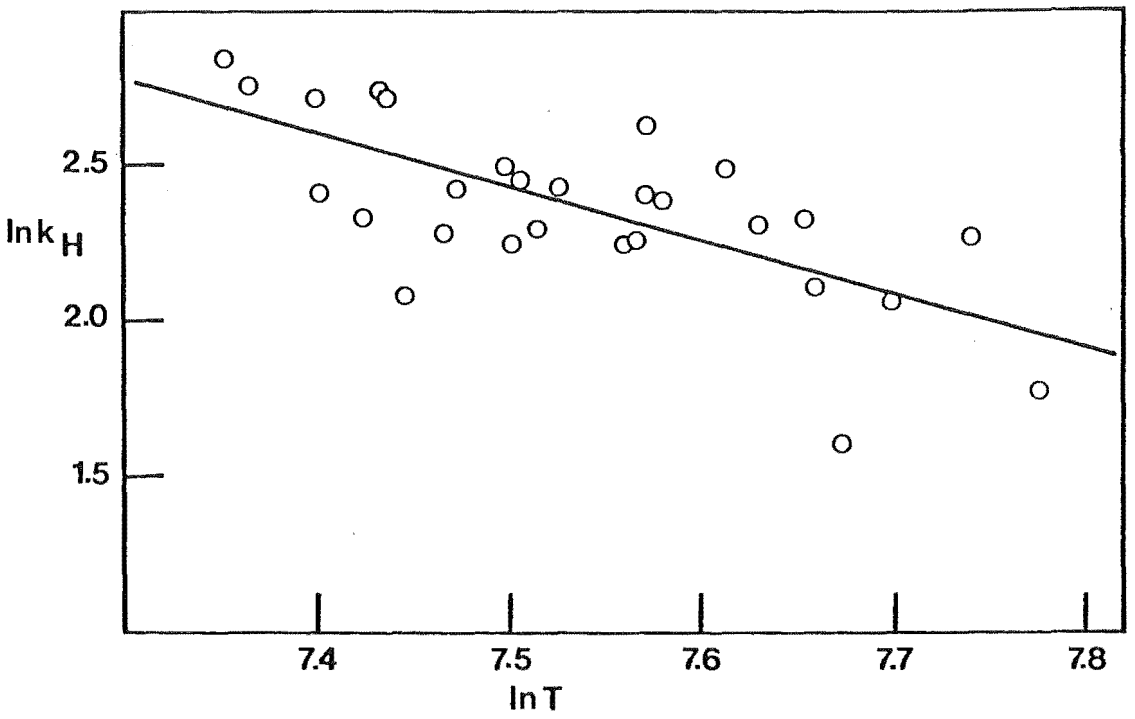

Fig. 24 (a) Regression of $\ln k_H$ on lnT; k_H is given in units of 10^{-10} cm.^{3} molecule.$^{-1}$ s^{-1}. T in ^{0}K.

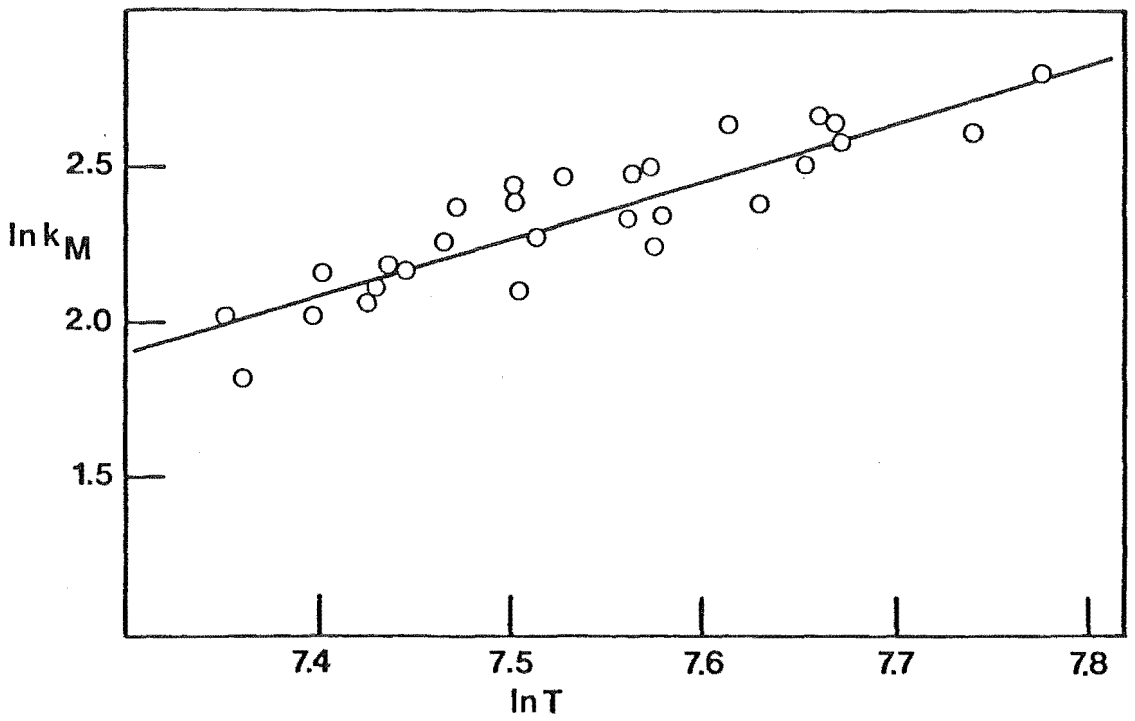

Fig. 24 (b) Regression of $\ln k_M$ on lnT; k_M is given in units of 10^{-12} cm.^{3} molecule.$^{-1}$s^{-1}. T in ^{0}K.

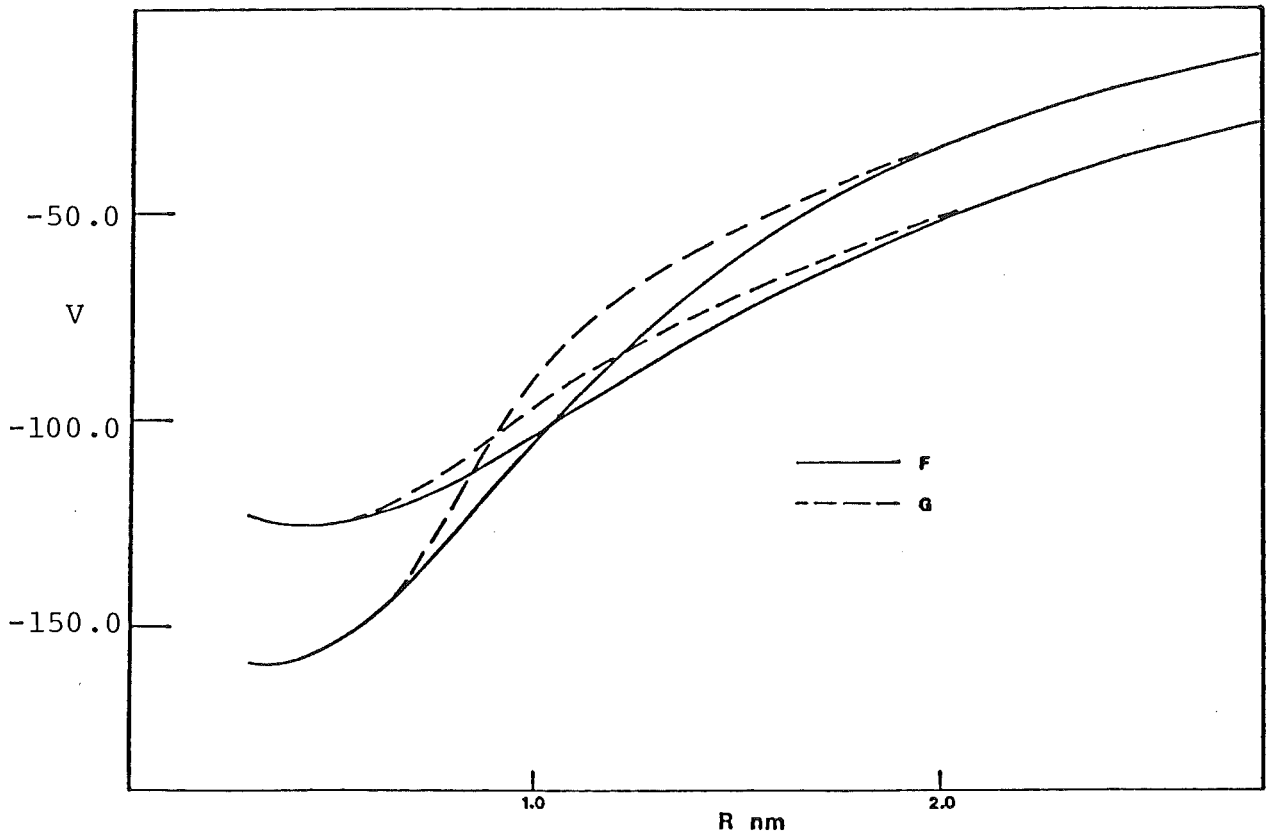

Fig. 25(a) Modified Morse potentials. The solid lines given by F are the potential curves of the Morse functions for the parameters given in Table 5(a). The curves given by G are the modified potentials, (see Table 6). V is in kJ mol^{-1}.

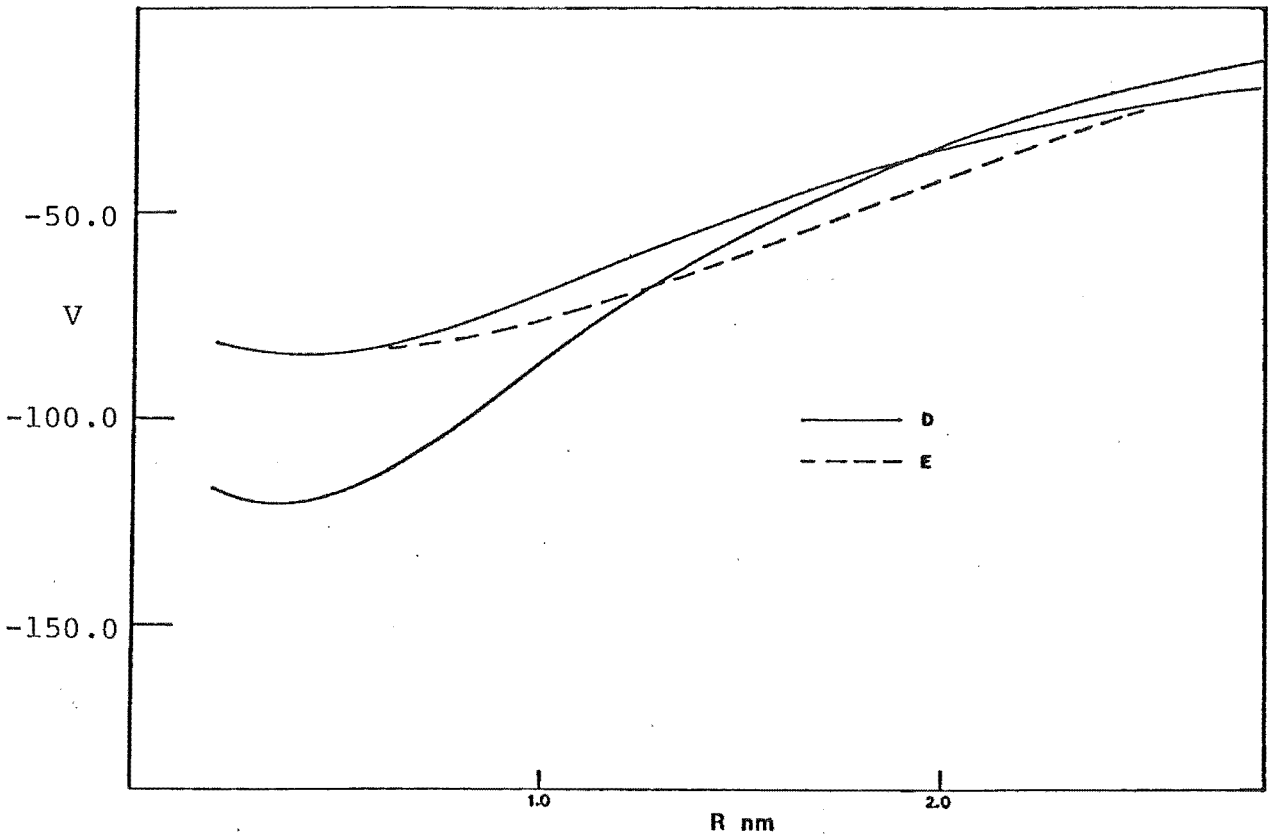

Fig. 25(b) Modified Morse potentials. The solid lines given by D are the potential curves of the Morse functions for the parameters given in Table 5(b). The curve given by E is the modified potential crossing with the deeper Morse curve, (see Table 6). V is in kJ mol^{-1}.

TABLE 5

Representative results of model calculations for k_H, with tunnelling and turning-point effects included.

(a) Morse curves (D_e = 160 (upper curve) and 120 $kJ.mol^{-1}$, $10^8 r_e$ = 3.5 and 4.5 cm, ω_e = 800 and 500 cm^{-1}; $10^8 R_X$ = 10.50 cm, V_X = -100.6 $kJ.mol^{-1}$)

$\varepsilon_{12}/kJ.mol^{-1}$	T/K	$10^9 k_H$	$10^2 P(T)$	$10^{13}\sigma(T)/cm^2$
0.3162	1400	3.84	3.65	5.81
0.3162	2000	3.24	3.54	4.23
0.3162	2600	2.85	3.43	3.37
0.100	1400	0.396	0.376	5.81
0.100	2000	0.334	0.365	4.23
0.100	2600	0.293	0.353	3.37

(b) Morse curves (D_e = 120 and 80 $kJ.mol^{-1}$, $10^8 r_e$ = 3.5 and 4.0 cm, ω_e = 600 and 400 cm^{-1}; $10^8 R_X$ = 17.75 cm, V_X = 41.4 $kJ.mol^{-1}$)

$\varepsilon_{12}/kJ.mol^{-1}$	T/K	$10^9 k_H$	$10^2 P(T)$	$10^{13}\sigma(T)/cm^2$
0.3162	1400	4.52	3.36	7.42
0.3162	2000	3.86	3.21	5.56
0.3162	2600	3.45	3.08	4.54
0.100	1400	0.452	0.336	7.42
0.100	2000	0.386	0.321	5.56
0.100	2600	0.345	0.308	4.54

(c) Morse curves (D_e = 160 and 120 $kJ.mol^{-1}$, $10^8 r_e$ = 5.5 and 6.0 cm, ω_e = 800 and 500 cm^{-1}, $10^8 R_X$ = 13.18 cm, V_X = -93.75 $kJ.mol^{-1}$)

$\varepsilon_{12}/kJ.mol^{-1}$	T/K	$10^9 k_H$	$10^2 P(T)$	$10^{13}\sigma(T)/cm^2$
0.3162	1400	6.43	4.14	8.58
0.3162	2000	5.60	4.14	6.25
0.3162	2600	5.00	4.07	4.98
0.100	1400	0.665	0.428	8.58
0.100	2000	0.579	0.428	6.25
0.100	2600	0.518	0.421	4.98

(Cont'd)

TABLE 5 (Cont'd)

(d) Morse curves (D_e = 80 and 40 kJ.mol^{-1}, $10^8 r_e$ = 3.5 and 4.0 cm, ω_e = 500 and 300 cm^{-1}; $10^8 R_X$ = 10.90 cm, V_X = -52.66 kJ.mol^{-1})

ε_{12}/kJ.mol^{-1}	T/K	$10^9 k_H$	$10^2 P(T)$	$10^{13}\sigma(T)$/cm^2
0.3162	1400	34.7	34.3	5.59
0.3162	2000	31.4	32.4	4.47
0.3162	2600	29.2	30.7	3.75
0.100	1400	6.42	5.43	5.59
0.100	2000	5.63	4.97	4.47
0.100	2600	5.07	4.57	3.85

(e) Lennard-Jones curves (D_e = 80 and 60 kJ.mol^{-1}, $10^8 r_e$ = 5.0 and 5.2 cm; $10^8 R_X$ = 6.108 cm, V_X = -40.92 kJ.mol^{-1})

ε_{12}/kJ.mol^{-1}	T/K	$10^9 k_H$	$10^2 P(T)$	$10^{13}\sigma(T)$/cm^2
1.00	1400	1.52	9.66	0.870
1.00	2000	1.68	11.9	0.652
1.00	2600	1.81	13.8	0.533
0.3162	1400	1.75	1.11	0.870
0.3162	2000	0.202	1.43	0.652
0.3162	2600	0.224	1.71	0.533

(f) Lennard-Jones curves (D_e = 120 and 100 kJ.mol^{-1}, $10^8 r_e$ = 5.0 and 5.1 cm; $10^8 R_X$ = 6.349 cm, V_X = -50.44 kJ.mol^{-1})

ε_{12}/kJ.mol^{-1}	T/K	$10^{11} k_H$	$10^2 P(T)$	$10^{13}\sigma(T)$/cm^2
1.00	1400	1.36	6.67	1.13
1.00	2000	1.59	8.77	0.839
1.00	2600	1.83	10.9	0.680
0.3162	1400	0.150	0.073	1.13
0.3162	2000	0.19	0.10	0.839
0.3162	2600	0.23	0.137	0.680

(Cont'd)

TABLE 5 (Cont'd)

(g) Lennard-Jones curves (D_e = 40 and 25 kJ.mol^{-1}, $10^8 r_e$ = 2.1 and 2.3 cm, $10^8 R_X$ = 2.411 cm, V_X = -27.36 kJ.mol^{-1}.)

ε_{12}/kJ.mol^{-1}	T/K	$10^9 k_H$	$10^2 P(T)$	$10^{15}\sigma(T)$/cm^2
1.00	1400	0.123	7.03	9.67
1.00	2000	0.111	6.89	7.40
1.00	2600	0.101	6.67	6.16
0.3162	1400	0.0133	0.758	9.67
0.3162	2000	0.0119	0.740	7.40
0.3162	2600	0.0108	0.711	6.16

Variation of k_H with temperature for calculated values given above: Morse curves;

ε_{12}/kJ.mol^{-1}	(a)	(b)	(c)	(d)
0.3162	$T^{-0.48}$	$T^{-0.44}$	$T^{-0.41}$	$T^{-0.28}$
0.100	$T^{-0.49}$	$T^{-0.44}$	$T^{-0.40}$	$T^{-0.38}$

Lennard-Jones curves;

ε_{12}/kJ.mol^{-1}	(e)	(f)
1.00	$T^{0.28}$	$T^{0.48}$
0.3162	$T^{-0.40}$	$T^{0.69}$

These results indicate that with suitable choice of Morse curves, the sign of the temperature coefficient can be reproduced. Deep potential wells show a larger negative value for the temperature coefficient and shallow potential wells show a smaller value. The calculations using Lennard-Jones 6-12 potentials show mostly positive temperature variations for k_H and do not predict the experimental results.

TABLE 6

Values of k_H obtained from model calculations using modified Morse curves as shown in Fig. 25.

Table lettering is the same as that used in Fig. 25.

(a) Original Morse curve from Table 5(b).

Modified curve shown as curve E in Fig. 25.

ε_{12}/kJ.mol^{-1}	T/K	$10^9 k_H$	$10^2 P(T)$	$10^{13}\sigma(T)$/cm^2
0.3162	1400	6.14	5.75	5.90
0.3162	2000	5.24	5.57	4.34
0.3162	2600	4.62	5.38	3.48
0.100	1400	0.646	0.604	5.90
0.100	2000	0.549	0.585	4.34
0.100	2600	0.484	0.563	3.48

(b) Original Morse curves from Table 5(a).

Modified curve shown as curve G in Fig. 25.

ε_{12}/kJ.mol^{-1}	T/K	$10^9 k_H$	$10^2 P(T)$	$10^{13}\sigma(T)$/cm^2
0.3162	1400	1.61	2.07	4.30
0.3162	2000	1.38	2.04	3.13
0.3162	2600	1.23	2.00	2.48
0.100	1400	1.65	2.11	4.30
0.100	2000	1.41	2.08	3.13
0.100	2600	1.25	2.04	2.49

Variation of k_H with temperature for calculated values given above:

ε_{12}/kJ.mol^{-1}	0.3162	0.100
Table 5 (b)	$T^{-0.44}$	$T^{-0.44}$
Table 6(a)	$T^{-0.46}$	$T^{-0.47}$
Table 5 (a)	$T^{-0.48}$	$T^{-0.49}$
Table 6 (b)	$T^{-0.43}$	$T^{-0.45}$

The signs and the magnitudes of the calculated temperature coefficients do not vary significantly when the original Morse curves are modified in the region of crossing.

TABLE 7

Values of k_M obtained from model calculations (Relative molecular mass of M = 18, Lennard-Jones, 6 - 12 potentials used throughout)

(a) D_e = 16 (upper curve) and 10 kJ.mol^{-1}, $10^8 r_e$ = 3.5 and 3.7 cm; $10^8 R_X$ = 3.79 cm; V_X = -13.73 kJ.mol^{-1}, F_1 and F_2 both positive.

ε_{12}/kJ.mol^{-1}	T/K	$10^{11} k_M$	$10^2 P(T)$	$10^{14} \sigma(T)$/cm^2
0.316	1400	28.3	14.9	1.421
0.316	2000	25.4	13.9	1.140
0.316	2600	23.5	13.1	0.986
0.100	1400	3.30	1.70	1.421
0.100	2000	2.88	1.58	1.140
0.100	2600	2.66	1.48	0.986

(b) D_e = 4.0 kJ.mol^{-1}, both curves, $10^8 r_e$ = 3.5 and 3.6 cm; $10^8 R_X$ = 3.10 cm, V_X = +0.703 kJ.mol^{-1}, F_1 and F_2 both negative.

ε_{12}/kJ.mol^{-1}	T/K	$10^{11} k_M$	$10^2 P(T)$	$10^{14} \sigma(T)$/cm^2
1.00	1400	5.62	15.3	0.274
1.00	2000	6.32	14.0	0.282
1.00	2600	7.21	13.8	0.286
0.316	1400	0.571	1.55	0.274
0.316	2000	0.659	1.46	0.282
0.316	2600	0.774	1.49	0.286

(c) D_e = 4.0 kJ.mol^{-1}, both curves, $10^8 r_e$ = 3.5 and 3.7 cm; $10^8 R_X$ = 3.27 cm, V_X = -2.93 kJ.mol^{-1}, F_1 and F_2 both negative.

ε_{12}/kJ.mol^{-1}	T/K	$10^{11} k_M$	$10^2 P(T)$	$10^{14} \sigma(T)$/cm^2
1.00	1400	14.4	22.0	0.489
1.00	2000	16.3	23.9	0.445
1.00	2600	17.9	23.3	0.420
0.316	1400	1.79	2.74	0.489
0.316	2000	2.08	2.92	0.445
0.316	2600	2.31	3.02	0.420

(Cont'd)

TABLE 7 (Cont'd)

(d) D_e = 8.0 and 6.0 kJ.mol^{-1}, $10^8 r_e$ = 5.5 and 5.7 cm; $10^8 R_X$ = 5.21 cm, V_X = -6.78 kJ.mol^{-1}, F_1 and F_2 both negative.

ε_{12}/kJ.mol^{-1}	T/K	$10^{11} k_M$	$10^2 P(T)$	$10^{14} \sigma(T)$/cm^2
0.316	1400	17.0	7.23	1.76
0.316	2000	18.5	7.73	1.50
0.316	2600	19.8	8.02	1.35
0.100	1400	1.84	0.781	1.76
0.100	2000	2.01	0.841	1.50
0.100	2600	2.16	0.815	1.35

Variation of k_M with temperature for calculated values given above:

ε_{12}/kJ.mol^{-1}	(a)	(b)	(c)	(d)
0.316	$T^{-0.3}$	$T^{0.4}$	$T^{0.35}$	$T^{0.25}$
0.100	$T^{-0.35}$	$T^{0.49}$	$T^{0.41}$	$T^{0.26}$

Provided the potential curves are chosen to cross where F_1 and F_2 are both negative, the signs of the temperature coefficients are predicted. It can be seen that shallow potential wells produce larger temperature variations and deeper wells produce smaller variations.

TABLE 8

Effect of bypassing tunnelling and turning-point subroutines on the results of model calculations of k_H. (Morse curves, D_e = 120 and 80 kJ.mol^{-1}, $10^8 r_e$ = 5.0 and 6.0 cm, ω_e = 800 and 500 cm^{-1}; $10^8 R_X$ = 13.3 cm, V_X = -56.9 kJ.mol^{-1})

(a) = all subroutines included;

(b) = no tunnelling through rotational barrier;

(c) = no tunnelling from below V_X;

(d) = effect of turning points disregarded.

ε_{12}/kJ.mol^{-1}	T/K	(a) $10^9 k_H$	(b) $10^9 k_H$	(c) $10^9 k_H$	(d) $10^9 k_H$
0.3162	1400	7.633	7.498	7.617	8.057
0.3162	2000	6.599	6.519	6.582	7.134
0.3162	2600	5.873	5.820	5.856	6.472
0.1000	1400	0.8189	0.8041	0.8179	0.9363
0.1000	2000	0.7056	0.6969	0.7045	0.8385
0.1000	2600	0.6262	0.6205	0.6251	0.7738

CHAPTER VII

CONCLUSION

The aim of the work described in this thesis was to develop the technique of laser fluorescence as a method of investigating reaction kinetics in combustion systems. It was hoped that by introducing trace additives to well characterised flames the rates of their reactions with minority flame species (free radicals) could be measured.

Initial investigations were concerned with the detection of the free radicals methylidyne (CH) and imidogen (NH) using laser excited fluorescence, but no results were obtained which would have encouraged further studies. In the case of CH, laser fluorescence was observed only in very hot oxy-acetylene flames and was limited to the very thin reaction zone. Attempts to extend this observation to premixed $H_2/N_2/O_2$ flames were not successful due to very low concentrations of CH, implying the presence of very fast reactions which remove it. Detection of NH by laser fluorescence in premixed $H_2/N_2/O_2$ flames was also unsuccessful, although it was quite easily seen in emission. The most plausible explanation for this is the poor matching of the NH absorption peak at 336.1 nm and the nitrogen laser emission at 337.1 nm. The use of frequency doubling from a dye laser at 672 nm, or a short-wavelength dye pumped by an excimer laser would allow excitation directly into the (0,0) band at 336.1 nm and possible kinetic studies.

Laser studies of metal atoms in flames were mainly confined to thallium and lead, although some significant measurements were made with copper and sodium. The fluorescence studies of thallium showed that excitation into the 6s $^3P_{\frac{3}{2}}$ state occurs primarily as a result of thermal excitation, and that chemiexcitation effects are absent.

The fluorescence studies of lead showed that the process 4.16

$$Pb(^3P_1{}^o) + H \xrightarrow{k_H} Pb(^3P_0{}^o) + H \qquad 4.16$$

was effective in competing with process 4.17

$$Pb(^3P_1{}^o) + M \xrightarrow{k_M} Pb(^3P_0{}^o) + M \qquad 4.17$$

where M is one of the bulk constituents of the flame such as H_2O, N_2 or H_2. The rates of the reactions were determined by observing the relative populations of the 7s $^3P_1{}^o$ and 7s $^3P_0{}^o$ states from fluorescence measurements. Experimental values of k_H and k_M are typically 10^{-9} $cm^3.molecule^{-1}.s^{-1}$ and 10^{-11} $cm^3.molecule^{-1}.s^{-1}$ respectively, with k_H showing a negative temperature dependence, varying as $T^{-1.7}$, and k_M showing a positive temperature dependence, varying as $T^{1.8}$. The discrepancy between the results obtained by excitation at 368.3 nm and 405.8 nm is most likely due to a change in scattered laser intensity at 368.3 nm. When lead atoms are added to the flame a portion of the laser light which would normally have been scattered is absorbed. This is not taken into account in the fluorescence measurements, and results in a slightly high value of $r' = \frac{I_{364.0}}{I_{368.3}}$ and hence k_H.

Model calculations based on the Landau-Zener theory of curve crossing collisions enabled rate constants and the

signs of the temperature dependencies for the spin orbit relaxation between Pb(7s $^3P_1^o$) and Pb(7s $^3P_0^o$) to be predicted. The magnitudes of the temperature coefficients were not well reproduced by the application of the Landau-Zener theory. For k_H, model calculations predicted a temperature variation corresponding to approximately $T^{-0.5}$ compared to the experimental value of $T^{-1.7}$, whereas for k_M, the predicted value was approximately $T^{0.4}$ and the experimental value was $T^{1.7}$.

The failure of the Landau-Zener model to correctly predict the temperature dependencies is most likely due to the lack of information available on the potential curves corresponding to the transient molecules formed during the collisions. It would be of considerable value to establish the vibrational frequencies and dissociation energy of excited PbH; this work is being initiated in the laboratory at present.

Precise determinations of the quenching rates of Pb(7s $^3P_0^o$), which are unavailable at the present, are needed since the assumption that they are identical to those of Pb(7s $^3P_1^o$) may account for part of the discrepancy between the two sets of rate constants obtained by excitation at 368.3 nm and 405.8 nm.

Experiments with collision partners other than hydrogen atoms may show spin-orbit relaxation effects similar to those observed in this work. The introduction of rare gases or halogens to flames may result in suitable interactions. Some work on halogens has been initiated but complications due to flame structure modification appear to give ambiguous results. In future work, better signal to noise ratios may be obtained by using lead halide dissociation lasers.

APPENDIX 1

Low noise F.E.T. amplifier used for preintegration.

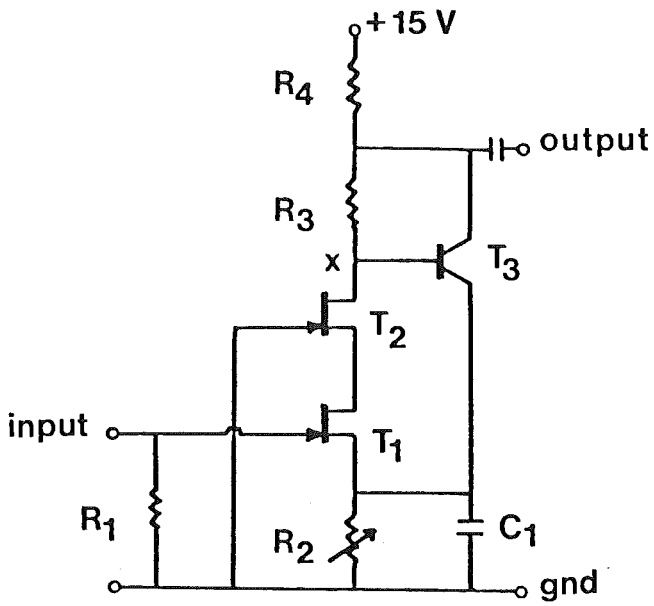

R_1 = 27kΩ
R_2 = 270Ω preset to give 10V at X.
R_3 = 2.7kΩ
R_4 = 1.5kΩ
T_1 = 2N4222A
T_2 = 2N4220A
T_3 = 2N5227

For a voltage gain of 85 C_1 = 30μF.
For a voltage gain of 5, C_1 was omitted.
With R_1 = 27kΩ the amplifier had an observed time constant of 3 to 5μs.

APPENDIX II

Data used in the calculation of $\Delta H^{o}(0)$, in equation 4.13, taken from JANAF thermochemical tables[53]. Bond angles are given as L(XYZ), bond lengths as R(XY) and vibration frequencies as ω

H	$\Delta H_f^o(0)$	=	216.028 kJ.mol^{-1}
OH	$\Delta H_f^o(0)$	=	38.798 kJ.mol^{-1}
	R(OH)	=	9.706 nm
	ω	=	3570 cm^{-1}
H_2O	$\Delta H_f^o(0)$	=	238.92 kJ.mol^{-1}
	R(OH)	=	9.584 nm
	L(HOH)	=	104.45^{o}
	ω(OH)	=	3657 cm^{-1}
	$\omega(HOH)_1$	=	1594.6 cm^{-1}
	$\omega(HOH)_2$	=	3765 cm^{-1}
LiOH	$\Delta H_f^o(0)$	=	58.7 kJ.mol^{-1}
	R(LiO)	=	15.82 nm
	R(OH)	=	9.7 nm
	L(LiOH)	=	180^{o}
	ω(LiO)	=	630 cm^{-1}
	ω(OH)	=	3661 cm^{-1}
	ω(LiOH)	=	362 cm^{-1}
Li	$\Delta H_f^o(0)$	=	159.13 kJ.mol^{-1}

APPENDIX III (a)

TIME EVOLUTION OF PB FLUORESCENCE
TEMPERATURE= 2000
LASER POWER (WATTS)= 200
BEAM DIAMETER(MM)= .5
LASER BANDWIDTH(SEC-1)= 2E+11
FLASH FWHM(SEC)= 5E-09
H (MINUS)= .01
LASER EXCITES PB(3P1)STATE

N	TIME(NS)	PB(3P1)	PB(3P0)	PB 6P(3P)
40	1.4	269.81	5.0482	8.64959E+08
80	2.8	1249.24	34.2138	8.6499E+08
120	4.2	6257.86	179.655	8.6496E+08
160	5.6	26825.1	886.361	8.64941E+08
200	7	98543.1	3165.4	8.6477E+08
240	8.39999	318618	10265.2	8.6425E+08
280	9.79997	834977	29122.5	8.6282E+08
320	11.2	1.92327E+06	70667.2	8.5952E+08
360	12.5999	3.76383E+06	147765	8.5296E+08
400	13.9999	6.3463E+06	263737	8.41974E+08
440	15.3999	9.86993E+06	402914	8.2526E+08
480	16.7999	1.11698E+07	527828	8.06973E+08
520	18.1999	1.16732E+07	595267	7.86917E+08
560	19.5998	1.05869E+07	596647	7.6855E+08
600	20.9998	8.31944E+06	492669	7.55869E+08
640	22.3998	5.67415E+06	364373	7.45369E+08
680	23.7998	3.35926E+06	255356	7.48597E+08
720	25.1998	1.72681E+06	132692	7.3981E+08
760	26.5998	776286	65686.6	7.3693E+08
800	27.9997	299179	28494.7	7.3654E+08
840	29.3997	101588	10691.7	7.3542E+08
880	30.7998	38259.2	3688.45	7.3639E+08
920	32.1998	7982.82	1114.34	7.3639E+08
960	33.5999	1882.12	382.892	7.365E+08
1000	34.9999	481.612	74.8197	7.3639E+08

INTEGRATED INTENSITIES:

I364 = 9.69617E+16 I369 = 2.73816E+16 RATIO= .366878

PEAK INTENSITIES:

I364 = 3.49763E+14 I369 = 1.03173E+14

RATIO= .29498

STEADY STATE RATIO= .366861

Excitation at 405.8 nm from $^3P_2$ state with 0.5mm focal diameter. Saturation occurs when the ratio PB(3P1):PB 6P(3P) reaches 3:5; maximum achieved is 1:60.

APPENDIX III (b)

TIME EVOLUTION OF PB FLUORESCENCE
TEMPERATURE= 2000
LASER POWER (WATTS)= 200
BEAM DIAMETER(MM)= .1
LASER BANDWIDTH(SEC-1)= 2E+11
FLUOR FWHM(SEC)= 1E-09
N (GRAMS)= .01
LASER EXCITES PB(3P1)STATE

N	TIME(NS)	PB(3P1)	PB(3P0)	PB 6P(3P)
40	.4	3725.41	28.7187	8.64993E+08
80	.8	43528.6	420.636	8.64946E+08
120	1.2	360436	3931.69	8.64556E+08
160	1.6	2.18776E+06	27069.6	8.62255E+08
200	2	9.6988E+06	137775	8.52256E+08
240	2.4	3.69656E+07	519116	8.2284E+08
280	2.8	6.93155E+07	1.42504E+06	7.6805E+08
320	3.2	1.00961E+08	2.8652E+06	6.7595E+08
360	3.6	1.30225E+08	4.41357E+06	5.9627E+08
400	4	1.25586E+08	5.42884E+06	5.3818E+08
440	4.4	1.0445E+08	5.69834E+06	5.03111E+08
480	4.8	7.72565E+07	5.25561E+06	4.86265E+08
520	5.2	5.1612E+07	4.46075E+06	4.78684E+08
560	5.6	3.24639E+07	3.42586E+06	4.79961E+08
600	6	1.9642E+07	2.51844E+06	4.88471E+08
640	6.4	1.17412E+07	1.76565E+06	4.98096E+08
680	6.8	7.0839E+06	1.28482E+06	5.0134E+08
720	7.2	4.18152E+06	884958	5.01557E+08
760	7.6	2.49972E+06	529227	5.01684E+08
800	8	1.49625E+06	343651	5.0176E+08
840	8.4	896745	220964	5.01885E+08
880	8.8	538043	148953	5.01932E+08
920	9.2	322166	99328.4	5.01945E+08
960	9.6	194294	56365	5.01859E+08
1000	10	116920	35328.1	5.01865E+08

INTEGRATED INTENSITIES:

I364 = 9.48354E+17 I368 = 2.84156E+17 RATIO= .299631

PEAK INTENSITIES:

I364 = 3.92513E+15 I368 = 9.785E+14

RATIO= .249268

STEADY STATE RATIO= .300001

Excitation at 405.8 nm from $^3P_2$ state with 0.1mm focal diameter. Saturation occurs when the ratio PB(3P1) : PB 6P(3P) reaches 3:5; maximum achieved is 1:4.5.

APPENDIX III (c)

TIME EVOLUTION OF PB FLUORESCENCE
TEMPERATURE= 2000
LASER POWER (WATTS)= 200
BEAM DIAMETER(MM)= .5
LASER BANDWIDTH(SEC-1)= 2E+11
FLASH FWHM(SEC)= 5E-09
N (NUMBER)= .01
LASER EXCITES PB(3PO) STATE

N	TIME(NS)	PB(3P1)	PB(3P0)	PB 6P(3P)
40	1.4	8.6585	149.977	8.64558E+08
80	2.8	60.8084	852.598	8.64594E+08
120	4.2	315.31	4462.89	8.64977E+08
160	5.6	1415	19181.6	8.64960E+08
200	7	5448.75	78016.4	8.64625E+08
240	8.39999	18066.5	219722	8.63743E+08
280	9.79997	51045.3	589776	8.61346E+08
320	11.2	123965	1.3516E+06	8.55787E+08
360	12.5999	257529	2.63764E+06	8.44805E+08
400	13.9999	456495	4.37256E+06	8.2635E+08
440	15.3999	696630	6.15478E+06	8.00219E+08
480	16.7999	891257	7.37844E+06	7.68657E+08
520	18.1999	968630	7.58173E+06	7.36212E+08
560	19.5998	949164	6.7281E+06	7.07604E+08
600	20.9998	793571	5.16597E+06	6.85846E+08
640	22.3998	588457	3.48811E+06	6.71543E+08
680	23.7998	372114	2.08205E+06	6.63422E+08
720	25.1998	209149	1.09867E+06	6.59453E+08
760	26.5998	103115	453979	6.5779E+08
800	27.9997	44671.8	173706	6.57194E+08
840	29.3997	17663.8	57981.7	6.57013E+08
880	30.7998	5776.72	16887.4	6.56968E+08
920	32.1998	1744.94	4336.24	6.56955E+08
960	33.5999	474.259	988.586	6.56954E+08
1000	34.9999	117.144	262.386	6.56954E+08

INTEGRATED INTENSITIES:

I406 = 3.43453E+16 I368 = 3.48878E+17 RATIO= .100757

PEAK INTENSITIES:

I406 = 1.29602E+14 I368 = 1.31401E+15

RATIO= .098783

STARK STATE RATIO = .100758

Excitation at 368.3 nm from $^3P_1$ state, with 0.5mm focal diameter. Saturation occurs when the ratio Pb(3PO) : Pb 6P(3P) reaches 1:3; maximum achieved is 1:100.

APPENDIX III (d)

TIME EVOLUTION OF PB FLUORESCENCE
TEMPERATURE= 2000

LASER POWER (WATTS)= 200

BEAM DIAMETER(MM)= .1

LASER BANDWIDTH(SEC-1)= 2E+11

FLASH PWHM(SEC)= 1E-09

N (ATMOS)= .01

LASER EXCITES PB(3P0) STATE

N	TIME(MS)	PB(3P1)	PB(3P0)	PB 6P(3P)
40	.4	50.3556	2738.9	8.6495E+08
80	.8	738.118	31827.3	8.6491E+08
120	1.2	6898.51	263851	8.6425E+08
160	1.6	47345.3	1.59111E+06	8.6837E+08
200	2	240513	6.98572E+06	8.4369E+08
240	2.4	903558	2.16844E+07	7.9329E+08
280	2.8	2.38236E+06	4.58349E+07	6.9862E+08
320	3.2	4.53176E+06	6.56615E+07	5.5395E+08
360	3.6	6.46695E+06	6.8404E+07	4.2911E+08
400	4	7.23367E+06	5.62404E+07	3.4374E+08
440	4.4	7.6252E+06	4.42527E+07	2.9575E+08
480	4.8	6.15445E+06	3.66814E+07	2.7606E+08
520	5.2	4.97676E+06	1.99258E+07	2.6942E+08
560	5.6	3.77562E+06	1.2873E+07	2.6831E+08
600	6	2.72583E+06	7.86262E+06	2.6861E+08
640	6.4	1.89713E+06	4.87925E+06	2.6901E+08
680	6.8	1.26573E+06	2.35203E+06	2.6928E+08
720	7.2	854478	1.35035E+06	2.6945E+08
760	7.6	559515	786323	2.6955E+08
800	8	362163	456297	2.6961E+08
840	8.4	232273	265431	2.6964E+08
880	8.8	147857	154775	2.6967E+08
920	9.2	93542	90464	2.6968E+08
960	9.6	58875.4	52997.7	2.6969E+08
1000	10	36895.4	31118.4	2.6965E+08

INTEGRATED INTENSITIES:

I466 = 2.71716E+17 I368 = 2.70034E+16 RATIO= .100623

PEAK INTENSITIES:

I466 = 9.58954E+14 I368 = 1.19368E+16

RATIO= .0796494

STEADY STATE RATIO = .100758

Excitation at 368.3 nm from $^3P_1$ state, with 0.1 mm focal diameter. Saturation occurs when the ratio PB(3PO) : Pb 6P(3P) reaches 1:3; maximum achieved is 1:6.

APPENDIX III (e)

TIME EVOLUTION OF PB FLUORESCENCE
TEMPERATURE= 2000
LASER POWER (WATTS)= 1000
BEAM DIAMETER(MM)= .1
LASER BANDWIDTH(SEC-1)= 2E+11
FLASH FWHM(SEC)= 5E-09
H (MINUS)= .01
LASER EXCITES PB(3P1)STATE

#	TIME(NS)	PB(3P1)	PB(3P0)	PB 6P(3P)
40	1.4	26124.6	631	8.64955E+08
80	2.8	156099	4275.54	8.64786E+08
120	4.2	748486	22427	8.63424E+08
160	5.6	3.32048E+06	186188	8.57922E+08
200	7	1.18547E+07	377823	8.3902E+08
240	8.39999	3.44173E+07	1.17134E+06	7.79745E+08
280	9.79997	7.32983E+07	2.98385E+06	6.52835E+08
320	11.2	1.06007E+08	4.74617E+06	4.64391E+08
360	12.5999	1.01197E+08	5.42431E+06	2.88366E+08
400	13.9999	7.26543E+07	4.49807E+06	1.68368E+08
440	15.3999	4.55254E+07	3.06385E+06	9.62677E+07
480	16.7999	2.68351E+07	1.89947E+06	5.47219E+07
520	18.1999	1.53526E+07	1.10857E+06	3.1234E+07
560	19.5998	8.64218E+06	632693	1.80983E+07
600	20.9998	4.81835E+06	355423	1.08162E+07
640	22.3998	2.64095E+06	197188	6.83378E+06
680	23.7998	1.4117E+06	107388	4.71965E+06
720	25.1998	715402	56358.8	3.66634E+06
760	26.5998	338067	27749	3.19639E+06
800	27.9997	134523	12481.6	3.01725E+06
840	29.3997	47459	4917.71	2.96043E+06
880	30.7998	14584.6	1716.97	2.94555E+06
920	32.1998	3882.87	529.944	2.94233E+06
960	33.5999	922.469	146.656	2.94176E+06
1000	34.9999	197.663	36.3935	2.94168E+06

INTEGRATED INTENSITIES:

I364 = 6.46865E+17 I368 = 1.83866E+17 RATIO= .300081

PEAK INTENSITIES:

I364 = 3.25632E+15 I368 = 9.36293E+14

RATIO= .287531

STEADY STATE RATIO= .300081

Excitation at 405.8 nm from $^3P_2$ state, with 0.1mm focal diameter and high laser power. Saturation occurs when the ratio PB(3P1) : PB 6P (3P) reaches 3:5; maximum achieved is 1:3.

REFERENCES

1. Gaydon, A.G.; Wolfhard, H.G. 1970, "Flames, Their Structure, Radiation and Temperature", Third Ed. (Rev.), Chapman and Hall, London.

2. Mavrodineanu, R.; Boiteux, H. 1965, "Flame Spectroscopy", Wiley and Sons, New York.

3. Kowalik, R.M.; Kruger, L.H. 1979, Comb. Flame, 34, 135.

4. Lapp, M.; Penney, C.M. 1977, Advances in Infrared and Raman Spectroscopy, Vol. 3. Heyden and Son, London.

5. Kuhl, J.; Marowsky, G. 1971. Opt. Commun., 4, 125.

6. Jenkins, D.R. 1970, Spectrochim. Acta, 25B, 47.

7. Phillips, L.F. 1960, Ph.D. Thesis, University of Cambridge.

8. McEwan, M.J. 1965, Ph.D. Thesis, University of Canterbury.

9. Mulvihill, J.N. 1975, Ph.D. Thesis, University of Canterbury.

10. Kaskan, W.E. 1957, Sixth Symposium (International) on Combustion, 134, Reinhold, New York.

11. Padley, P.J. 1959, Ph.D. Thesis, University of Cambridge.

12. James, C.G.; Sugden, T.M. 1955, Proc. Roy. Soc. (London), A227, 312.

13. de Voss, J.C. 1954, Physica, 20, 690.

14. Padley, P.J.; Sugden, T.M. 1958, Proc. Roy. Soc. (London), A248, 248.

15. "EMI Photomultiplier Tubes", Brochure 30M-6-67 (PMT), Issue 1, EMI Electronics Limited. Valve Division, London.

16. Thorne, A.P. 1974, "Spectrophysics", Chapman and Hall, London.

17. Klauminzer, G.K. 1975, Laser Focus, Nov. , 35.

18. Lester, T.W.; Wittig, S.C.K. 1977, Sixteenth Symposium (International) on Combustion, 671, The Combustion Institute, Pittsburgh.

19. Porter, R.P.; Clark, A.H.; Kaskan, W.E.; Browne, W.E. 1966, Eleventh Symposium (International) on Combustion, 907, The Combustion Institute, Pittsburgh.

20. Hayhurst, A.N.; Kittelson, D.B. 1978, Comb. Flame, 31, 37.

21. Bowser, R.J.; Weinberg, F.J. 1976, Comb. Flame, 27, 21.

22. Bascombe, K.N.; Green, J.A.; Sugden, T.M. 1963, Advances in Mass Spectrometry, 2, 66.

23. Bulewicz, E.M.; Padley, P.J.; Smith, R.E. 1970, Proc. Roy. Soc. (London), A315, 129.

24. Barnes, R.H.; Moeller, C.E.; Kircher, J.F.; Verber, C.M. 1973, Appl. Optics, 12, 2531.

25. Peeters, J.; Lambert, J.F.; Hertoghe, P.; van Tiggelen, A. 1970, Thirteenth Symposium (International) on Combustion, 321, The Combustion Institute, Pittsburgh.

26. Turek, C.A.; Yardley, J.T. 1971, IEEE J. Quantum Elect., QE-7, 102.
Sahar, E.; Wieder, I. 1974, IEEE J. Quantum Elect., QE-10, 612.

27. Nadler, M.P.; Wang, V.K.; Kaskan, W.E. 1970, J. Phys. Chem., 74, 917.

28. Kaskan, W.E.; Nadler, M.P., 1972, J. Chem. Phys., 56, 2220.

29. Gordon, S.; Mulac, W.; Nangia, P. 1971, J. Phys. Chem., 75, 2087.

30. McConnell, J.C. 1973, J. Geophys. Res., 78, 7812.

31. Zetsch, C.; Hansen, I. 1978, Ber. Bunsenges Phys. Chem., 82, 830.

32. Hansen, I.; Hoinghaus, K.; Zetsch, C.; Stuhl, F. 1976, Chem. Phys. Lett., 42, 370.

33. See end of reference table, p 108.
34. See end of reference table, p 108.
35. See end of reference table, p 108.

36. Fraser, L.M.; Winefordner, J.D. 1972, Anal. Chem., 44, 1444.

37. Padley, P.J.; Sugden, T.M. 1958, Seventh Symposium (International) on Combustion, 235, Butterworths, London.

38. Gaydon, A.G. 1968, Dissociation Energies, Chapman and Hall, London.

39. Kuhl, J.; Spitschan, H. 1973, Opt. Commun., 7, 256.

40. Bolshov, M.A.; Zybin, A.V.; Koloshnikov, V.G.; Koshelev, K.N. 1977, Spectronchim. Acta, 32B 279.

41. Jenkins, D.R. 1969, Proc. Roy. Soc. (London) A313, 551.

42. Mandl, A.; Chen, Hao-Lin 1976, Phys. Rev., A14, 264.

43. de Zaffra, R.L.; Marshall, A. 1968, Phys. Rev., 170, 28.

44. Penkin, N.P.; Slavenas, I.Y.Y. 1963, Opt. Spectrosc., 15, 83.

45. Husain,, D.; Littler, J.G.F. 1972, J. Photochem., 1, 327 : 1972, Chem. Phys. Lett., 16, 145.

46. Friswell, N.J.; Jenkins, D.R. 1972, Comb. Flame, 19, 197.

47. Moore, C.E. 1971, Atomic Energy Levels, Vol.4, Circular 467, National Bureau of Standards, Washington.

48. Bulewicz, E.M.; Sugden, T.M. 1958, Trans. Farad. Soc. , 54, 1855.

49. Bulewicz, E.M.; James, C.G.; Sugden, T.M. 1956, Proc. Roy. Soc. (London), 235, 89.

50. Fenimore, C.P.; Jones, G.W. 1957, J. Phys. Chem., 61, 654.

51. Bulewicz, E.M.; Sugden, T.M. 1956, Trans. Farad. Soc., 52, 1475.

52. Blickensderfer, R.P.; Jordan, K.D. 1979, Chem.Phys., 41, 193.

53. JANAF Thermochemical Tables 1971, NS RDS-NB537, National Bureau of Standards, Washington D.C.

54. Bulewicz, E.M.; Sugden, T.M. 1958, Chem. Soc. (London), Spec. Publ. No. 9, 81.

55. Omenetto, N.; Benetti, P; Hart, L.P.; Winefordner, J.D.; Alkemade, C.Th.J. 1973, Spectrochim. Acta, 28B, 289.

56. Daily, J.N. 1977, Appl. Optics, 16, 568.

57. Phillips, L.F. 1965, "Basic Quantum Chemistry", John Wiley and Sons, New York.

58. Peipmeier, E.H. 1972, Spectrochim. Acta, 27B, 431.

59. Landau, L. 1932, Z.Phys. 2, 46. (Ref. not sighted but see Ref. 60)

60. Zener, C. 1932, Proc. Roy. Soc. (London), A137, 696.

61. Stuckelberg, E.G.G. 1932, Helv. Phys. Acta, 5, 369 : (Ref. not sighted but see Ref. 63)

62. Elbel, M. "Progress in Atomic Spectroscopy", 1979, (Ed. W. Hanle, and H. Kleinpoppen), Plenum Press, New York.

63. Child, M.S. 1972, Trans. Farad. Soc., 53, 18.

64. Byhovskii, V.K.; Nikitin, E.E.; Ovchinnikova, M.Ya. 1965, J. Expt. Theor. Phys., 20, 500.

65. Nikitin, E.E. 1961, Opt. i. Spectr. (trans.) 11, 246.

66. Abramovitz, M.; Stegun, I.A. 1965, "Handbook of Mathematical Functions", Dover Publications, New York.

67. Nikitin, E.E. 1968, "Chemische Elementarprozesse", Ed. H. Hartmann, 43, Springer-Verlag, New York.

68. Pearson, R.G. 1976, "Symetry Rules for Chemical Reactions", Wiley Interscience, New York.

69. Landau, L.D.; Lifshitz, E.M. 1959, "Quantum Mechanics", (transl. J.B. Sykes and J.S. Bell), Pergamon Press, London.

70. Tully, J.D. 1976, Dynamics of Molecular Collisions, Ed. W.H. Miller, B, 217.Plenum Press, N.Y.

71. Child, M.S. 1974, "Molecular Collision Theory", Academic Press, London.

72. Nikitin, E.E. 1974, "Theory of Elementary Atomic and Molecular Processes in Gases", (transl. M.J. Kearsley), Oxford University Press, London.

73. Herzberg, G. 1950, "Molecular Spectra and Molecular Structure : Volume 1; Diatomic Molecules", Van Nostrand, New York.

74. Rapp, D. 1970, "Quantum Mechanics", Holt, Reinhart and Wilson, New York.

75. McEwan, M.J.;Phillips, L.F. 1967, Comb. Flame, 11, 63.

76. Fristrom, R.M.; Westenberg, A.A. 1965, "Flame Structure", McGraw Hill, New York.

33. Halpern, J.B.; Hancock, G.; Lenzi, M.; Welge, K.H. J. Chem. Phys., 1975, 63, 4808.

34. Kroll, M. 1975, J.Chem.Phys. 63, 319.

35. Anderson, R.; Crosley, D.R. 1975, Chem.Phys.Lett., 62, 275.